

**Studies on Nonlinear Frequency Conversion Techniques
using $\chi^{(2)}$ Processes**

By

Rashmi Rekha Sahoo

PHYS11201604006

**National Institute of Science Education and Research
Bhubaneswar**

A thesis submitted to the

*Board of Studies in
Physical Sciences*

for the Degree of

DOCTOR OF PHILOSOPHY

of

HOMI BHABHA NATIONAL INSTITUTE



January, 2023

Homi Bhaba National Institute

Recommendations of the Viva Voce Committee

As members of the Viva Voce Committee, we certify that we have read the dissertation prepared by Rashmi Rekha Sahoo entitled "Studies on Nonlinear Frequency Conversion Techniques using $\chi^{(2)}$ Processes" and recommend that it may be accepted as fulfilling the thesis requirement for the award of Degree of Doctor of Philosophy.

Chairman - Prof. Sanjay Kumar Swain

Sanjay Swain
7/6/23

Guide / Convener - Dr. Ritwick Das

Ritwick Das
07/06/2023

Examiner - Prof. Shailendra K Varshney

Shailendra K Varshney
07.06.2023

Member 1 - Dr. Ashok Kumar Mohapatra

Ashok Kumar Mohapatra

Member 2 - Dr. Kartikeswar Senapati

K. Senapati

Member 3 - Dr. Rajan Jha

Rajan Jha

Final approval and acceptance of this thesis is contingent upon the candidate's submission of the final copies of the thesis to HBNI.
I/We hereby certify that I/we have read this thesis prepared under my/our direction and recommend that it may be accepted as fulfilling the thesis requirement.

Date : 07/06/2023

Place : JATNI

Signature
Co-guide (if any)

Ritwick Das

Signature
Guide

STATEMENT BY AUTHOR

This dissertation has been submitted in partial fulfillment of requirements for an advanced degree at Homi Bhabha National Institute (HBNI) and is deposited in the Library to be made available to borrowers under rules of the HBNI.

Brief quotations from this dissertation are allowable without special permission, provided that accurate acknowledgement of source is made. Requests for permission for extended quotation from or reproduction of this manuscript in whole or in part may be granted by the Competent Authority of HBNI when in his or her judgment the proposed use of the material is in the interests of scholarship. In all other instances, however, permission must be obtained from the author.

Rashmi Rekha Sahoo
RASHMI REKHA SAHOO
Name & Signature of the Student

DECLARATION

I hereby declare that I am the sole author of this thesis in partial fulfillment of the requirements for a postgraduate degree from National Institute of Science Education and Research (NISER). I authorize NISER to lend this thesis to other institutions or individuals for the purpose of scholarly research.

Rashmi Rekha Sahoo .
RASHMI REKHA SAHOO
Name & Signature of the Student

List of Publications arising from the thesis

Journal

1. "Thermo-Optic effects in congruent- $LiTaO_3$ based continuous-wave optical parametric oscillator," R. R. Sahoo, M. K. Shukla and R. Das, *IEEE Photonics Technol. Lett.* **33** (19) 2021.
2. "Green laser pumped congruently-grown $LiTaO_3$ based singly-resonant optical parametric oscillator," R. R. Sahoo, M. K. Shukla and R. Das, *Results in Optics* **9** 2022.
3. "Stimulated polariton scattering in Yb-laser pumped lithium niobate based continuous-wave singly-resonant optical parametric oscillator," R. R. Sahoo, M. K. Shukla and R. Das, *J. Opt. Soc. Am. B* **39** (10) 2022.

Manuscript under preparation

1. "Evolution of geometric phase in a three-wave mixing process using singly-resonant optical parametric oscillator based on $LiNbO_3$,"

Conferences

1. "Thermo-optic manifestation in $LiTaO_3$ based continuous wave parametric oscillator", R. R. Sahoo, M. K. Shukla and R. Das, In: Singh K., Gupta A.K., Kher S., Dixit N., Pant K. (eds) IOCL-2019. Springer proceedings in physics, vol 258. Springer, Singapore. <https://doi.org/10.1007/978-981-15-9259-1-154>
2. "Stimulated polariton scattering on $LiNbO_3$ based optical parametric oscillator", M. K. Shukla, R. R. Sahoo and R. Das, In: Singh K., Gupta A.K., Kher S., Dixit N., Pant K. (eds) IOCL-2019. Springer proceedings in physics, vol 258. Springer, Singapore. <https://doi.org/10.1007/978-981-15-9259-1-153>

Rashmi Rekha Sahoo
RASHMI REKHA SAHOO
Name & Signature of the Student

Dedicated to my parents.....

ACKNOWLEDGEMENTS

This thesis is the outcome of an extensive four and a half-year endeavor. During this period, I encountered numerous hurdles, both personal and professional, compounded by the global pandemic and subsequent lockdowns. However, the successful completion of my PhD is a testament to the collective efforts of numerous individuals. I would like to express my heartfelt gratitude to all those who played a significant role in this remarkable journey.

I would like to begin by expressing my sincere gratitude to the members of my doctoral committee, Dr. Sanjay Swain, Dr. Ritwick Das, Dr. Ashok Kumar Mohapatra, Dr. Kartikeswar Senapati, and Dr. Rajan Jha for their participation as committee members and for their diligent evaluation of my work on an annual basis.

I am grateful for the support and professionalism demonstrated by the academic staff, electrical staff, and workshop staff, whose commitment to providing timely solutions and their willingness to go above and beyond their responsibilities have made a significant impact on the quality and completion of my research.

I would like to express my sincere gratitude to my supervisor, Dr. Ritwick Das, for providing me with the invaluable opportunity to join his research group as a PhD student. Throughout my journey, he has been a constant source of support and guidance. I am truly grateful for his thoughtfulness, which has helped me develop critical thinking skills and a keen interest in my research field. I have been fortunate to learn from his insights and benefit from his wisdom, which has significantly influenced the direction of my career. His storytelling has a captivating aura, which never fails to motivate me to persevere in my endeavors. I am truly grateful for the impact he has had on my career.

I would like to extend my heartfelt gratitude to my lab seniors, Samir Bhaiya and Mukesh Bhaiya, Partha Bhaiya and Jitendra Bhaiya for their unwavering support and for fostering a friendly work environment within the lab. Their guidance and mentorship have been invaluable throughout my journey.

I would like to extend my sincere appreciation to my fellow lab mates, Anupa, Abhishek, Shailja, Surbhi, Soumik and Rudra Bhai, for their camaraderie and support throughout our journey together. Their collaboration and friendship have made the lab environment a truly enriching and enjoyable place to work.

I would also like to express my gratitude to the M.Sc. students who carried out their master's theses in our lab, namely Renu Raman, Pankaj, Pravanjan and Dinesh. Furthermore, I would like to give a special thanks to Pravanjan for his delightful cup of coffee that has kept us energized and made our days vibrant.

I would like to acknowledge the invaluable contributions of individuals who played an integral role in my journey, extending beyond the academic realm. Foremost, I express my heartfelt gratitude to my younger sister, Dipti, whose unwavering support and motivation have been immeasurable. Despite being six years younger, she has consistently guided and supported me throughout this journey.

I would like to express my deep gratitude to my parents for their unwavering presence and support throughout my journey. Their constant love, encouragement, and guidance have been instrumental in shaping the person I am today. From the very beginning, my parents have been my pillars of strength, providing me with a solid foundation on which to build my dreams. They have consistently believed in me, motivating me to strive for excellence and pursue my passions. Whether it was helping me with research, providing a listening ear during challenging times, or offering valuable advice, their wisdom and experience have been invaluable resources.

I am grateful to my batchmates, Tanim, Dukhi, Charanpreet, Subir, Pratidhawni, Asish, Rik, Akshay, Milan, Anupa, Purbasha, Bharat, Dipika, Bimalesh, and Laxmipriya, for their warmth and accomplishment during the initial days of our time at the institute. Their friendship and support made the transition into the new environment much smoother and more familiar.

I am grateful for the unwavering support and equal credibility shown by other members of NISER who have been a part of my journey. I would like to extend my appreciation to Shiva Bhaiya, Arup Bhaiya, Sushree Di, Manoar Bhaiya, Dusmant Bhaiya, Amita Di, Ekta Di, Sony Di, Durga Bhaiya, Kishan, Soumya, Sujit, Surya, Nandini, Toushif, Supriya, Prerna, Lipsa, Akankshya, Bhabhani, Jnaneswar, Anjan and Mouli. Their presence and camaraderie have enriched my overall experience at NISER. From engaging discussions to shared moments of celebration and challenges, we have supported and encouraged one another.

Finally, I would like to express my deepest gratitude to Gentle for his unwavering support over the past six years. His consistent support and encouragement during both the highs and lows of my journey have been invaluable to me. He has been a steadfast presence, always standing by my side and providing the support I needed. His belief in my abilities, even during challenging times, has instilled confidence in me and pushed me to surpass my own expectations. I am profoundly grateful for the invaluable impact he has had on my personal and professional growth.

Rashmi Rekha Sahoo
School of Physical Sciences,
NISER Bhubaneswar

Summary

In the present thesis, we have demonstrated the work based on singly resonant optical parametric oscillator (SRO), which operates in continuous wave regions. The noncentrosymmetric nonlinear crystals possessing $\chi^{(2)}$, are suitable for designing SROs. SROs based on periodically poled $LiTaO_3$ and $LiNbO_3$ have the tunability from near-infrared to far infrared in the electromagnetic spectrum. In the SRO based on $LiTaO_3$, we have studied the tunability and the efficiency of the SRO. In addition, we have carried out a numerical study to understand the thermo-optic effects. In the subsequent study, we investigated an SRO based on periodically poled $LiNbO_3$. The infrared and Raman active $LiNbO_3$ facilitate the stimulated polariton scattering (SPS) in the SRO. By virtue of this SPS process, we have observed Stokes shifted side peaks in the spectrum of the signal. The three-wave mixing process in a nonlinear crystal, between the pump, signal, and idler has an equivalence with the spin-1/2 system in a magnetic field. This analogy helped to access the growth of the signal/idler modes using a geometric representation.

Contents

Summary	1
List of Figures	4
Chapter 1 Introduction	5
References	12
Chapter 2 Fundamentals of Nonlinear Optics	17
2.1 Second order nonlinear optical processes	18
2.2 Second Order Nonlinear Susceptibility	21
2.3 Electromagnetic wave propagation in presence of nonlinear optical interaction	22
2.4 Phase-matching condition	26
2.4.1 Birefringent phase-matching	27
2.5 Quasi-Phase-Matching	29
2.5.1 Techniques to achieve QPM	31
2.6 Frequency conversion process and amplification	32
2.7 Optical parametric oscillator	34
2.7.1 Laser pump source	36
2.7.2 Nonlinear crystal	37
2.7.3 Cavity mirrors	37
2.8 Wavelength tuning	38
2.9 Phase matching bandwidth	39
2.9.1 Temperature bandwidth	39
2.10 Optical Parametric Oscillators (OPOs)	40
2.11 Cavity design and ABCD matrix method	42
2.12 Conclusion	44
References	45
Chapter 3 Study of thermo-optic effects in singly- resonant optical parametric oscillator	50
3.1 Motivation	50
3.2 Experimental configuration	52
3.3 Results and Discussion	53
3.3.1 Wavelength Tuning	54
3.3.2 Power Scaling	55
3.3.3 Thermo-optic manifestations	56
3.3.4 Spatial beam characteristics	63
3.4 Conclusion	64
References	66
Chapter 4 Stimulated polariton scattering in $LiNbO_3$ based singly-resonant optical parametric oscillator	72
4.1 Motivation	72

4.2	Experimental Configuration	74
4.3	Results and Discussion	76
4.3.1	SRO: Wavelength Tunability and Conversion Efficiency	76
4.3.2	Power Scaling	77
4.3.3	Stimulated Polariton Scattering	78
4.3.4	Polariton mode dispersion and gain	81
4.4	Conclusion	88
References	90
 Chapter 5 Geometric phase measurement in singly resonant optical parametric oscillator		 95
5.1	Motivation	95
5.2	Geometric phase in three wave mixing process	96
5.3	Experimental set-up	100
5.4	Result and Discussion	102
5.5	Conclusion	104
References	105
 Future Scope		 108

List of Figures

1.1	Summary of the wavelength tuning of various Laser sources and Optical parametric oscillator.	6
2.1	Representation of polarization for a model of atom	17
2.2	Representation of different $\chi^{(2)}$ nonlinear frequency conversion processes	21
2.3	Refractive index representation for birefrngent crystal	28
2.4	Schematic of QPM structure and the process	30
2.5	Linear cavity representing singly resonant OPO	35
2.6	Cavity configuration of linear cavity	40
2.7	Types of OPO cavity	42
2.8	Variation of resonating beam radius as the beam propagates inside the cavity	43
3.1	Schematic of the experimental set-up for MgO:cPPLT SRO	52
3.2	Temperature tuning of MgO:cPPLT SRO	54
3.3	Power scaling of MgO:cPPLT SRO	55
3.4	Simulated variation of temperature within the crystal	58
3.5	Maximum temperature at the crystal center at different pump beam waist and pump power	60
3.6	Longitudinal variation of phase-mismatch with incident pump power	61
3.7	Normalized open aperture Z-scan transmission trace of MgO:cPPLT	62
3.8	Pump and idler beam-profile at the exit-face of crystal	63
4.1	Schematic of the experimental set-up for the MgO:cPPLN SRO	75
4.2	Temperature tuning and power scaling of MgO:cPPLN SRO	76
4.3	Schematic representation of phase-matching between SRO signal beam and SPS Stokes beam and polariton mode	79
4.4	Signal spectrum of SRO for $\Lambda_{QPM} = 29.5 \mu$	79
4.5	Signal spectrum of SRO for $\Lambda_{QPM} = 30 \mu m$	81
4.6	Dispersion relation for TO phonon modes and polariton frequency of SRO for $\Lambda_{QPM} = 29.5 \mu m$	83
4.7	Dispersion relation for TO phonon modes and polariton frequency of SRO for $\Lambda_{QPM} = 30 \mu m$	84
4.8	SRO signal wavelength for $\Lambda_{QPM} = 29.5 \mu m$	87
4.9	SRO signal wavelength for $\Lambda_{QPM} = 29.5 \mu m$	88
5.1	Schematic of the experimental set-up for the SRO placed at one of the interferometer arm	100
5.2	Power scaling of SRO at $100^\circ C$	102
5.3	Variation of intensity at the center of the fringe pattern of the interferometer	104

Chapter 1

Introduction

The acronym LASER stands for “light amplification by stimulated emission of radiation” [1, 2]. Since its discovery, lasers are used to generate and amplify coherent radiation in the electromagnetic (*em*) spectrum ranging from ultraviolet, infrared (IR) and extended to far in IR. The discovery of Laser is one of the greatest invention that opened gate for many other fundamental researches. The concept of Laser is based on the theoretical work prescribed by Charles Hard Townes and Arthur Leonard Schawlow [3, 4]. Later on, in the year 1960, Theodore H. Maiman at Hughes Research Laboratories developed the first laser [5]. The first experimentally realised laser had an active medium constituted by ruby crystal which emitted coherent radiation in red-band of *em* spectrum. With the technological research and development, lasers are now used to generate deep ultra-violet and X-ray wavelengths. Such sources enable a path for carrying out detailed studies on chemical and biochemical processes [6]. The importance and the application of laser in commonplace devices are numerous. The laser beams have remarkable properties which includes good directionality, highly monochromatic and strong intensity [2]. From the perspective of time-scale, lasers could operate from continuous wave to attosecond regime [7]. Sources in attosecond time scale could produce an extremely high power ($\mathcal{O}(10^9 \text{ watt})$) peak power and consequently, they could be used for exploring process that exhibit very weak physical manifestations [8]. Such possibilities to enormously expand into wide variety of applications have led the race to develop lasers operating at extremely short time-scales. Undoubtedly, there are many facets which are yet to be discovered and developed.

It is seamlessly apparent that the advent and development of lasers pave the path for carrying out fundamental studies in science which includes exploring nonlinear optical characteristics of materials, Raman scattering, different forms of spectroscopy, gravitational wave detection and many more [9, 10]. In view of industrial applications, lasers have been extremely good candidates for optical communications, mechanical material processing (welding, drilling, cutting), biomedical imaging and medical surgeries and military warfare, information processing and storage. From the meteorological point of view, today lasers form the backbone for standardization of precision length and time measurement [11, 12, 13, 14].

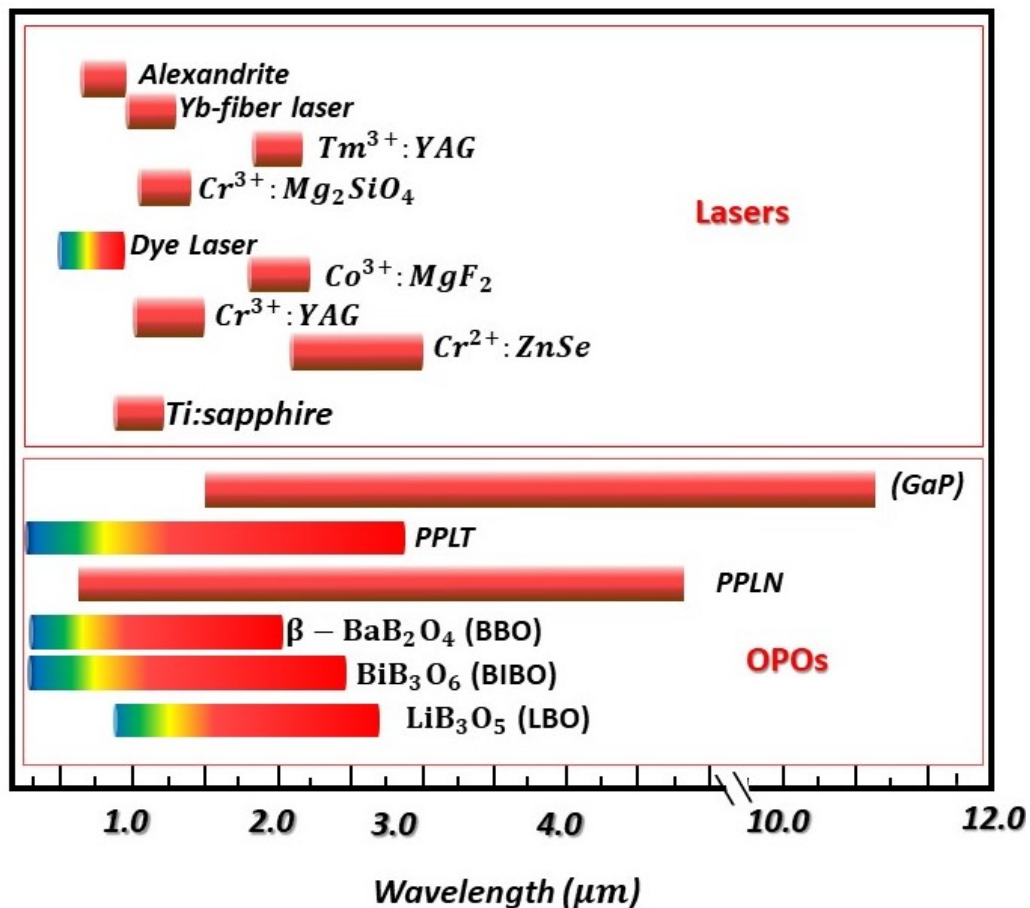


Figure 1.1: Summary of the wavelength tuning of various Laser sources and Optical parametric oscillator.

Figure 1.1 shows an overview to some of the available tunable laser sources [15]. Ti:sapphire laser is the most widely used tunable source. Due to the availability of broad gain bandwidth it could be used for ultrashort pulse generation [16]. The maximum wavelength tunability offered by Ti:sapphire crystal based laser sources extend from 650 *nm* to 1100 *nm*. Some other available solid state laser sources are ruby, Nd:YAG and Nd:glass [17]. The most widely known gas lasers are He-Ne, Argon ion and CO_2 [18, 19]. These sources have limited applications on the basis of high spectral coverage or in terms of high available output power. Wavelength tunability of laser source in visible region could be obtained by using organic dye lasers which can be tuned from 300 *nm* to 1.2 μm . A few other kind of laser sources are fiber laser and semiconductor lasers which offer far less wavelength tunability [20].

In general, the conventional laser sources have been used to cover a wide range in the *em* spectrum over half a century. However, there remains several gaps in the *em* spectrum which are yet to be bridged using conventional laser sources. In addition the conventionally used laser sources have some shortcomings in terms of fine wavelength tunability, irregular spatial beam quality and low wall-plug efficiency.

Through an alternative route, coherent sources could be obtained based on second-order nonlinear frequency conversion processes in non-centrosymmetric crystals [9, 21]. The frequency conversion process generally is a three wave mixing process between the three interacting waves, namely pump (ω_p), signal (ω_s) and idler (ω_i). The advent of second-order nonlinear optical processes such as optical parametric generation and oscillation have paved the path for accessing the near infrared and mid-infrared spectral band with high optical power and excellent beam quality. The nonlinear optical processes essentially involve a material exhibiting high second-order nonlinear coefficient in combination with the available high-power laser sources.

Sources based on the frequency conversion process could offer high output power in different spectral bands. Consequently, they could be adopted to operate in a wide temporal regime extending from continuous-wave (CW) and quasi-CW (or nanosecond) regime to ultrashort (picosecond and femtosecond) time-scales. These sources, therefore, could be used for various applications listed above and a few more.

In the year 1961, *Franken et al.* have observed experimentally the coherent nonlinear optical effect for the first time [22]. He demonstrated the second harmonic generation in quartz crystal. This discovery put forward the importance of nonlinear process in the direction of new frequency generation processes [23, 24]. In general, a nonlinear frequency conversion process involves two sources such as sum frequency generation (SFG) or difference frequency generation (DFG). The second harmonic generation (SHG) is a special case of sum frequency generation where the two input sources have the identical frequency. On the other hand, processes such as optical parametric generation and oscillation are configured with single pump source. Many difference frequency generation based sources are being used presently for a variety of applications such as spectroscopy, optical microscopy, trace gas sensing etc. However, a DFG based CW optical source is significantly limited in terms of low to very low output power.

A high frequency conversion efficiency or a high output power could be obtained through devising an optical parametric oscillator (OPO). As common to all nonlinear optical process, OPOs provide a platform to generate frequencies in broad spectral bands and at various temporal scales. Hence, now a days, one of the efficient techniques for obtaining tunable source is to device OPOs using suitable pump source, an optimum cavity and a suitable nonlinear optical crystal.

The working and function of an OPO is mainly dependent on the spectral and spatial beam quality of the incident pump beam. Additionally, the properties associated with the nonlinear crystal have a key role in the development of the OPO cavity. Lack of

suitable nonlinear materials in terms of achieving phase matching condition for a desired spectral region hampered the development of practical OPOs for several years. In the year 1965 *Giordmaine and Miller* first realised OPO experimentally [25]. This development evoked an intense surge of research and development in parametric devices and uphold a comprehensive study of sources based on nonlinear materials. A rigorous study has been carried out for nearly two decades in the development and understanding of the parametric frequency conversion in a cavity configuration and established many fundamental principles and practical benchmarks for this area. However, the practical implication of the OPOs has been harnessed until the development of nonlinear materials such as, Lithium Niobate ($LiNbO_3$ (LN)), Lithium Tantalate ($LiTaO_3$ (LT)), Bismuth Borate or Bismuth (BiB_3O_6 (BIBO)), Beta-Barium Borate ($\beta - BaB_2O_4$ (BBO)), Lithium Triborate (LiB_3O_5 (LBO)), Potassium Titanyl Phosphate ($KTiOPO_4$ (KTP)), Rubidium Titanyl Arsenate ($RbTiOAsO_4$), Barium Sodium Niobate ($Ba_2NaNb_2O_5$), Gallium Arsenide ($GaAs$), Lithium Iodate ($LiIO_3$) and Potassium Niobate ($KNbO_3$). [26, 27, 28, 29, 30, 31, 32, 33, 34, 35, 36, 37, 38, 39, 40, 41]. These crystals have rendered sources based on frequency conversion processes to be viable sources of coherent light for a broad category of fundamental and practical applications.

At this point, it is worth pointing out that high-power coherent sources operating in CW regime with wide tunability are of great importance for many applications including a variety of spectroscopic applications and quantum optical studies. As pointed out before, Ti:sapphire laser and dye laser have been successfully employed for this purpose, OPOs provide a plausible alternative bridging the limitation of wide frequency tunability and stable output over long duration in conjunction with a cost-effective simple experimental design. In general, the nonlinear optical processes in CW regime faces many practical challenges due to very low nonlinear optical gain for the CW pumps. Hence, the deployment of the resonator cavities provide a plausible route to amplify the frequency converted beams. The

first CW OPO was made by using birefringent KTP crystal by *Yang et al.* in the year 1993 [42]. The discovery of quasi-phase matched (QPM) crystals in ferroelectric materials have enhanced the studies of nonlinear frequency conversion process by multiple times [26, 43]. Since the demonstration of OPO for the first time, the advancement of new long-length QPM materials in association with the developed pump sources have established OPOs as practical sources for delivering coherent tunable radiation at all power levels. The developed pump sources include high-power fiber lasers. These developments have continued the legacy of frequency conversion processes in the advancement of generating new frequency.

The work presented in the thesis primarily focuses on the singly-resonant OPOs (SROs) operating in the CW regime. The SROs discussed in the thesis are devised using periodically-poled $LiTaO_3$ and $LiNbO_3$ crystals of 50 mm and 80 mm respectively. The usage of periodically-poled crystals facilitates the access to the maximum nonlinear optical coefficient for the process. The SROs offer a wide tunability from near-infrared (NIR) to far-infrared (FIR) spectral band in the electromagnetic spectrum. In addition, all the SROs are pumped by fiber lasers which are used to pump the SROs. This will ensure the efficiency and robustness of the frequency mixing process.

The thesis is organized in six chapters. In the second chapter, we will discuss the theoretical framework to understand the $\chi^{(2)}$ -based nonlinear optical processes. We would also provide a brief discussion on the OPO cavity design which includes a suitable $\chi^{(2)}$ nonlinear optical medium.

The third chapter of the thesis will present a demonstration and characterization of a high-power continuous wave (cw) SRO made up of MgO-doped congruently grown $LiTaO_3$ (cPPLT). By optimally focusing the pump beam at the center of a cPPLT crystal and varying the temperature of the crystal-oven, we have generated a tunable radiation from 1810 – 1920 nm yielding a maximum power of ≈ 583 mW. The SRO's threshold is 2.1 W at a

oven temperature of $50^{\circ}C$ and shows an early saturation at $3.1 W$ pump power. The creation of a temperature gradient inside the crystal is the primary reason for this saturation behaviour observed in the idler beam power. The local rise in temperature along the longitudinal direction of the beam propagation are obtained by solving the differential equation for heat conduction.

In chapter four, we explored the impact of high-power signal beam resonating inside the cw-SRO which is tunable in the mid-infrared spectral band. The cw SRO is based on a 80 mm long 8-mol% MgO-doped periodically poled $LiNbO_3$ (PPLN) crystal. In the PPLN based SRO (with nonlinear grating period = $29.5\mu m$), the crystal temperature tuning yielded a wavelength tunability from $3625 - 3825 nm$ with a maximum power of $1.9 W$ at $3765 nm$ for an incident pump power of $\approx 24 W$. We observed that the signal spectrum of SRO exhibits multiple peaks even though the pump is a single-frequency beam. In case of $30\mu m$ grating-period, we observed a similar SRO signal spectrum. We have investigated these frequency shifted beams in view of the stimulated polariton scattering (SPS) process taking place in the nonlinear crystal. The SPS process could facilitate the generation of coherent CW-FIR (or terahertz) beams by employing the high intra-cavity signal power.

In the fifth chapter, we will discuss an analytical framework to draw equivalence of a TWM process in SRO with a spin-1/2 system in magnetic field. This idea allows us to ascertain the growth of signal/idler modes using a geometrical representation. We also demonstrate a experimental configuration where the $LiNbO_3$ based SRO forms one arm of the Mach-Zehnder interferometer. Finally, in chapter six, we present a future outlook to the work presented in the thesis.

References

- [1] K. Thyagarajan and A. Ghatak. *Lasers: fundamentals and applications*. Springer Science & Business Media, 2010.
- [2] A. E. Siegman. *Lasers*. University science books, 1986.
- [3] J. P Gordon, H. J Zeiger, and C. H Townes. The maser—new type of microwave amplifier, frequency standard, and spectrometer. *Physical review*, 99(4):1264, 1955.
- [4] A. L. Schawlow and C. H. Townes. Infrared and optical masers. *Phys. Rev.*, 112:1940–1949, Dec 1958.
- [5] T. H. Maiman. *Stimulated optical radiation in ruby*. Society of Photo-Optical Instrumentation Engineers, 1960.
- [6] S. Beggs, J. Short, M. Rengifo-Pardo, and A. Ehrlich. Applications of the excimer laser: a review. *Dermatologic Surgery*, 41(11):1201–1211, 2015.
- [7] F. Lépine, G. Sansone, and M. J. J. Vrakking. Molecular applications of attosecond laser pulses. *Chemical Physics Letters*, 578:1–14, 2013.
- [8] J. Duris, S. Li, T. Driver, E. G. Chapenois, J. P. MacArthur, A. A. Lutman, Z. Zhang, P. Rosenberger, J. W. Aldrich, R. Coffee, G. Coslovich, F. J. Decker, J. M. Glow-
nia, G. Hartmann, W. Helml, A. Kamalov, J. Knurr, J. Krzywinski, M. F. Lin, J. P. Marangos, M. Nantel, A. Natan, J. T. O’Neal, N. Shivaram, P. Walter, A. L. Wang, J. J. Welch, T. J. A. Wolf, J. Z. Xu, M. F. Kling, P. H. Bucksbaum, A. Zholents, Z. Huang, J. P. Cryan, and A. Marinelli. Tunable isolated attosecond x-ray pulses with gigawatt peak power from a free-electron laser. *Nature Photonics*, 14(1):30–36, dec 2019.
- [9] Robert W Boyd. *Nonlinear optics*. Academic press, 2020.

-
- [10] B. P. Abbott, R. Abbott, R. Adhikari, P. Ajith, B. Allen, G. Allen, R. S. Amin, S. B. Anderson, W. G. Anderson, and M. A. Arain. Ligo: the laser interferometer gravitational-wave observatory. *Reports on Progress in Physics*, 72(7):076901, 2009.
- [11] F. P. Gagliano, R. M. Lumley, and L. S. Watkins. Lasers in industry. *Proceedings of the IEEE*, 57(2):114–147, 1969.
- [12] K. Meiners-Hagen, R. Schödel, F. Pollinger, and A. Abou-Zeid. Multi-wavelength interferometry for length measurements using diode lasers. *Measurement science review*, 9(1):16, 2009.
- [13] A. E. Ennos. Speckle interferometry. In *Laser speckle and related phenomena*, pages 203–253. Springer, 1975.
- [14] H. F. Shih, T. P. Yang, M. O. Freeman, J. K. Wang, H. F. Yau, and D. R. Huang. Holographic laser module with dual wavelength for digital versatile disc optical heads. *Japanese journal of applied physics*, 38(3S):1750, 1999.
- [15] Majid Ebrahim-Zadeh. Continuous-wave optical parametric oscillators. *Handbook of Optics*, 4:1–33, 2010.
- [16] H. Liu, S. Sun, L. Zheng, G. Wang, W. Tian, D. Zhang, H. Han, J. Zhu, and Z. Wei. Review of laser-diode pumped ti: sapphire laser. *Microwave and Optical Technology Letters*, 63(8):2135–2144, 2021.
- [17] R. L. Byer. Diode laser—pumped solid-state lasers. *Science*, 239(4841):742–747, 1988.
- [18] R. J. Wiet, Douglas C Kubek, Paul Lemberg, and Arkadiush T Byskosh. A meta-analysis review of revision stapes surgery with argon laser: effectiveness and safety. *Otology & Neurotology*, 18(2):166–171, 1997.

-
- [19] M. Radovanovic and M. Madic. Experimental investigations of CO_2 laser cut quality: a review. *Nonconventional Technologies Review*, 4(4):35, 2011.
- [20] P. Kronenberg and O. Traxer. The laser of the future: reality and expectations about the new thulium fiber laser—a systematic review. *Translational andrology and urology*, 8(Suppl 4):S398, 2019.
- [21] William Paul Risk, William Paul Risk, TR Gosnell, and AV Nurmikko. *Compact blue-green lasers*. Cambridge University Press, 2003.
- [22] P. A. Franken, A. E. Hill, C. W. Peters, and G. Weinreich. Generation of optical harmonics. *Physical Review Letters*, 7(4):118, 1961.
- [23] R. H. Kingston. Parametric amplification and oscillation at optical frequencies. *Proceedings of the Institute of Radio Engineers*, 50(4):472, 1962.
- [24] S. A. Akhmanov and R. V. Khokhlov. Concerning one possibility of amplification of light waves. *Sov. Phys. JETP*, 16:252–257, 1963.
- [25] J. A. Giordmaine and Robert C Miller. Tunable coherent parametric oscillation in $LiNbO_3$ at optical frequencies. *Physical Review Letters*, 14(24):973, 1965.
- [26] M Yamada, N Nada, M Saitoh, and K Watanabe. First-order quasi-phase matched $LiNbO_3$ waveguide periodically poled by applying an external field for efficient blue second-harmonic generation. *Applied Physics Letters*, 62(5):435–436, 1993.
- [27] K Kato. Second-harmonic generation to 2048 Å in b-ba 2 o 4. *IEEE journal of quantum electronics*, 22(7):1013–1014, 1986.
- [28] Xiaofan Cao, Ramakant Srivastava, Ramu V Ramaswamy, and Jamal Natour. Recovery of second-order optical nonlinearity in annealed proton-exchanged linbo/sub x. *IEEE Photonics technology letters*, 3(1):25–27, 1991.

- [29] CT Chen, BC Wu, AD Jiang, and GM You. A new-type ultraviolet shg crystal-beta-bab2o4. *Scientia Sinica Series B-Chemical Biological Agricultural Medical & Earth Sciences*, 28(3):235–243, 1985.
- [30] Albert A Ballman and H Brown. Ferroelectric domain reversal in lithium metatantate. *Ferroelectrics*, 4(1):189–194, 1972.
- [31] JT Lin, JL Montgomery, and K Kato. Temperature-tuned noncritically phase-matched frequency conversion in lib3o5 crystal. *Optics Communications*, 80(2):159–165, 1990.
- [32] Shujie Lin, Baichang Wu, Fali Xie, and Chuangtian Chen. Phase-matching retracing behavior: New features in LiB_3O_5 . *Applied physics letters*, 59(13):1541–1543, 1991.
- [33] YS Luh, MM Fejer, RL Byer, and RS Feigelson. Stoichiometric linbo3 single-crystal fibers for nonlinear optical applications. *Journal of Crystal Growth*, 85(1-2):264–269, 1987.
- [34] Mool C Gupta, WP Risk, Alan CG Nutt, and SD Lau. Domain inversion in $KTiOPO_4$ using electron beam scanning. *Applied physics letters*, 63(9):1167–1169, 1993.
- [35] Mool C Gupta, William Kozlovsky, and Alan CG Nutt. Second-harmonic generation in bulk and waveguided $LiTaO_3$ with domain inversion induced by electron beam scanning. *Applied physics letters*, 64(24):3210–3212, 1994.
- [36] M Scheidt, B Beier, K-J Boller, and R Wallenstein. Frequency-stable operation of a diode-pumped continuous-wave rbtioaso 4 optical parametric oscillator. *Optics letters*, 22(17):1287–1289, 1997.
- [37] RG Smith, JE Geusic, HJ Levinstein, JJ Rubin, S Singh, and LG Van Uitert. Continu-

- ous optical parametric oscillation in $\text{Ba}_2\text{NaNb}_2\text{O}_5$. *Applied Physics Letters*, 12(9):308–310, 1968.
- [38] P Günter, PM Asbeck, and SK Kurtz. Second-harmonic generation with $\text{Ga}_{1-x}\text{Al}_x$ as lasers and KNO_3 crystals. *Applied Physics Letters*, 35(6):461–463, 1979.
- [39] Arkadiusz Galat, Krzysztof M Abramski, Pawel A Duda, Wieslaw Strek, Andrei N Kuzmin, Gennadii I Ryabtsev, ZA Ges, and VP Konyayev. Second-harmonic generation in LiIO_3 at 490 nm using InGaAs/AlGaAs laser diodes. In *Metal/Nonmetal Microsystems: Physics, Technology, and Applications*, volume 2780, pages 340–343. SPIE, 1996.
- [40] L Gordon, GL Woods, RC Eckardt, RR Route, RS Feigelson, MM Fejer, and R Byer. Diffusion-bonded stacked GaAs for quasiphase-matched second-harmonic generation of a carbon dioxide laser. *Electronics Letters*, 22(29):1942–1944, 1993.
- [41] M. Ghotbi, A. Esteban-Martin, and M. Ebrahim-Zadeh. BiB_3O_6 femtosecond optical parametric oscillator. *Opt. Lett.*, 31(21):3128–3130, Nov 2006.
- [42] ST Yang, RC Eckardt, and RL Byer. Continuous-wave singly resonant optical parametric oscillator pumped by a single-frequency resonantly doubled $\text{Nd}:\text{Yag}$ laser. *Optics letters*, 18(12):971–973, 1993.
- [43] Walter R Bosenberg, Alexander Drobshoff, Jason I Alexander, Lawrence E Myers, and Robert L Byer. 93% pump depletion, 3.5-w continuous-wave, singly resonant optical parametric oscillator. *Optics letters*, 21(17):1336–1338, 1996.

Chapter 2

Fundamentals of Nonlinear Optics

Optical phenomenon observed in day to day life such as reflection, refraction, dispersion and diffraction could be explained through the presence of low intensity of light. When the amplitude of applied electromagnetic wave is small the electromagnetic wave have a linear response [1]. In other words, the material polarization varies linearly with the applied electric field. The polarization response of the medium with the applied field could be represented mathematically as;

$$P = \epsilon_0 \chi^{(1)} E \quad (2.1)$$

where ϵ_0 is the permittivity of free space, and $\chi^{(1)}$ is the linear susceptibility tensor with components dependent on frequency of the electromagnetic wave and other material properties.

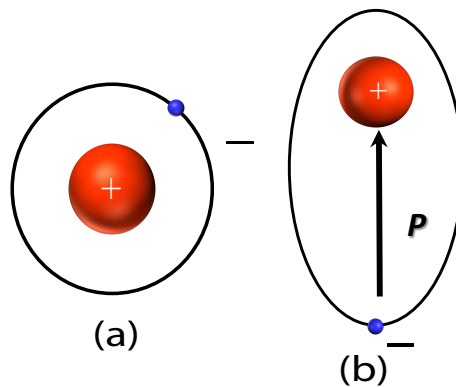


Figure 2.1: Representation of a model of atom (a) in the absence of electric field, (b) in the presence of electric field

On the other hand when the amplitude of the applied electric field is large, the material properties are significantly altered [2, 3]. In the presence of a very high electric field, the displacement of electron cloud induces anharmonic oscillations which manifests through nonlinear optical effects [4, 5, 6, 7]. In that case, the induced polarisation could be represented in terms of the power series expansion in the field as,

$$P = \epsilon_0 \chi^{(1)} E + \epsilon_0 \chi^{(2)} E^2 + \epsilon_0 \chi^{(3)} E^3 + \dots \quad (2.2)$$

The first term in the equation 2.2 represents the linear polarisation which oscillates with the frequency of the applied electric field. And $\chi^{(1)}$ is the linear susceptibility responsible for the linear optical effects such as transmission, reflection and absorption (linear). The second term is responsible for second order polarisation, which is dependent on the second order susceptibility $\chi^{(2)}$. This gives rise to phenomenon such as second harmonic generation (SHG), sum-frequency generation (SFG), difference frequency generation (DFG), the linear electro-optic (Pockels) effect and the optical parametric generation (OPG) and optical parametric amplification (OPA) [8, 9, 6, 10]. In these processes, the polarization have a quadratic dependence on the incident electric field. The third-order nonlinear susceptibility results in processes such as the third harmonic generation (THG), optical bistability, phase-conjugation and optical Kerr effect. The higher-order terms manifests through the generation of new higher order oscillation frequency [11, 5]. In the present thesis, I will discuss on the second-order nonlinear optical susceptibility related processes.

2.1 Second order nonlinear optical processes

The second order nonlinear optical process involves three waves such as $(\omega : \omega_1 + \omega_2)$. The total electric field present in the medium is represented as [12, 13]

$$\tilde{E}(t) = E_1(t)e^{-i\omega_1 t} + E_2(t)e^{-i\omega_2 t} + c.c. \quad (2.3)$$

The contribution of second-order polarization is given by,

$$\tilde{P}^{(2)}(t) = \epsilon_o \chi^{(2)} \tilde{E}(t)^2 \quad (2.4)$$

By substituting Eq. 2.3 in Eq. 2.1, the nonlinear polarization corresponding to different frequency components could be obtained. In that case, the nonlinear polarization could be expressed as

$$\begin{aligned} \tilde{P}^{(2)}(t) = \epsilon_o \chi^{(2)} [& E_1^2 e^{-2i\omega_1 t} + E_2^2 e^{-2i\omega_2 t} + 2E_1 E_2 e^{-i(\omega_1 + \omega_2)t} + 2E_1 E_2^* e^{-i(\omega_1 - \omega_2)t} + c.c.] \\ & + 2\epsilon_o \chi^{(2)} [E_1 E_1^* + E_2 E_2^*] \quad (2.5) \end{aligned}$$

Different components for second-order nonlinear polarization term is given by

$$\begin{aligned} P(2\omega_1) &= \epsilon_o \chi^{(2)} E_1^2 \quad (SHG) \\ P(2\omega_2) &= \epsilon_o \chi^{(2)} E_2^2 \quad (SHG) \\ P(\omega_1 + \omega_2) &= 2\epsilon_o \chi^{(2)} E_1 E_2 \quad (SFG) \\ P(\omega_1 - \omega_2) &= 2\epsilon_o \chi^{(2)} E_1 E_2^* \quad (DFG) \\ P(0) &= 2\epsilon_o \chi^{(2)} (E_1 E_1^* + E_2 E_2^*) \quad (OR) \end{aligned} \quad (2.6)$$

Incident electromagnetic waves with frequencies ω_1 and ω_2 can generate aforementioned polarization terms and there remains good chance to generate radiation at those frequencies with appreciably high intensity through nonlinear interaction. In order to achieve this, the phase-matching condition needs to be satisfied. This could be understood as follows. During the light propagation, the nonlinear polarization and the corresponding electromagnetic wave accumulates different phases [1, 14, 15]. Therefore, for an efficient generation, these two must add constructively and alternately; they need to be phase-matched.

In order to illustrate the aforementioned point, let us consider a difference frequency generation (DFG) process. The DFG process could be visualized mathematically from equation 2.6. The DFG process is defined by the nonlinear process described in equation 2.6. It is evident that the generated nonlinear polarization has frequency equal to the

frequency difference $(\omega_1 - \omega_2)$ between the two waves. In such a scenario, the energy and the momentum conservation laws could be represented as;

$$\omega_3 = \omega_1 - \omega_2 \quad (2.7)$$

$$k_3 = k_1 - k_2 \quad (2.8)$$

where $k_i = \frac{n(\omega_i)\omega_i}{c}$ are the respective wavevectors, and $n(\omega)$ is the frequency dependent refractive index. Equation 2.8 is often referred to as the phase-matching condition which depends on the propagation of the waves inside the nonlinear medium. From the equation 2.7, it is clearly evident that two photons of frequency ω_1 and ω_2 are utilized to generate a lower frequency ω_3 . In this process, one of the waves amongst ω_1 and ω_2 is amplified and consequently, this process is termed as optical parametric amplification (OPA). It is worthwhile to point that even in the absence of ω_2 frequency ω_2 and ω_3 could be generated from ω_1 frequency which is known as optical parametric generation (OPG) [16, 17, 18]. In a simplified language, in OPG process, a higher frequency wave termed as pump (ω_p) generates two frequency waves which are termed as signal (ω_s) and idler (ω_i) are generated. Conventionally, the shorter wavelength is known as signal and the longer wavelength is known as the idler.

Typically, the pulsed lasers have relatively higher peak power as compared to power in a continuous-wave laser. Hence, it could offer sufficiently high intensities for the parametrically-generated waves even in a single pass configuration in a nonlinear crystal. On the other hand, for continuous wave lasers, the efficiency of OPG process is substantially small. Hence, a suitable feedback is essential for generating useful optical power. A Fabry-Perot cavity configuration is used to provide a feedback to the process and consequently, the nonlinear crystal could be placed inside the cavity consisting of mirrors for obtaining a suitable feedback. Such configurations are known as optical parametric oscillators (OPOs)

[9, 19, 20, 21]. In the next section, a brief discussion on essential facets of second-order susceptibility is presented.

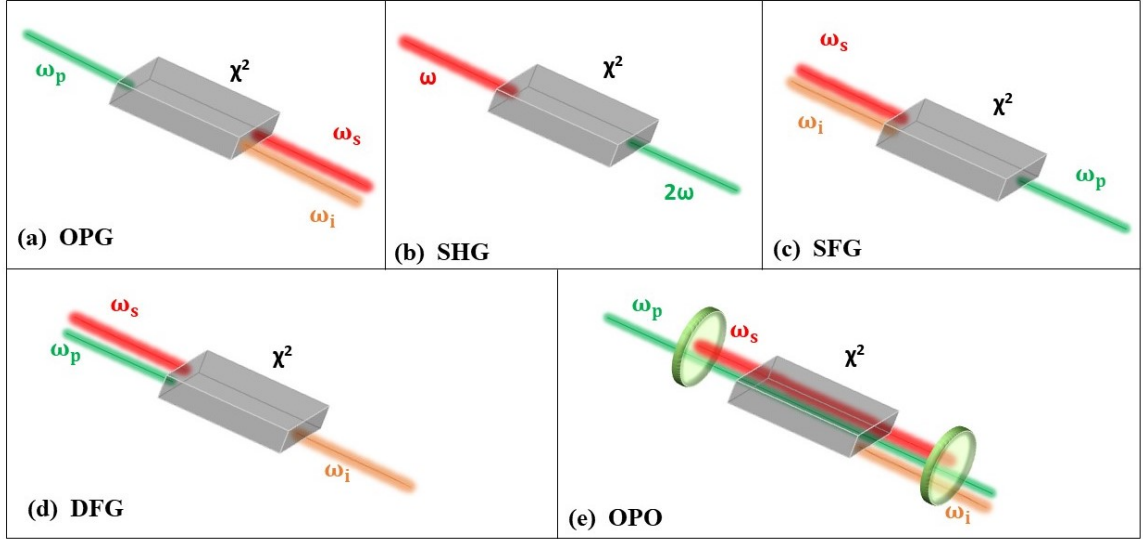


Figure 2.2: Representation of different $\chi^{(2)}$ nonlinear frequency conversion processes (a) Optical parametric generation, (b) Second harmonic generation (c) Sum frequency generation (d) Difference frequency generation (e) Optical parametric oscillator

2.2 Second Order Nonlinear Susceptibility

The interaction of three optical waves could be described using the nonlinear optical polarization which contains the second-order susceptibility term. In general, second-order nonlinear optical polarization is expressed as

$$P_i^{(2)}(\omega_n + \omega_m) = \epsilon_0 \sum_{jk} \sum_{(nm)} \chi_{ijk}^{(2)}(\omega_n + \omega_m, \omega_n, \omega_m) E_j(\omega_n) E_k(\omega_m) \quad (2.9)$$

where the indices j and k represents the directions in which the incident field(s) are oscillating. The index i represents direction of generated polarization. The notation (nm) indicates the summation over n^{th} and m^{th} frequency. The significance of the summation is that the sum $\omega_n + \omega_m$ will remain fixed even when ω_n and ω_m picks different values. The

product of electric field ($E(\omega_n)E(\omega_m)$) generates a nonlinear polarization oscillating at a frequency ($\omega_n + \omega_m$).

The structural properties (or the crystal symmetry) of the nonlinear crystal govern the values as well as the symmetry in $\bar{\chi}^{(2)}$ tensor. For example, a certain crystal symmetry results in vanishing a few elements of the susceptibility tensor. It is worth pointing out that $\bar{\chi}^{(2)}$ is not a *null* tensor only if the nonlinear crystal does not possess a center of inversion symmetry [14, 22].

2.3 Electromagnetic wave propagation in presence of nonlinear optical interaction

The generated nonlinear optical polarization ($\vec{P}^{(2)}$) is the source of new frequency components which is not present in the incident beam. This essentially means that the dipoles in medium are oscillating at a new frequency (or new frequencies). Hence, the medium could generate new frequencies efficiently when all the dipoles oscillate in such a phase that the newly generated electric field strengthens during the propagation. This idea of constructive generation of new field is alternatively known as phase matching condition.

The propagation of electromagnetic wave through a nonlinear optical medium could be ascertain through the solutions of Maxwell's equations. Where we have considered

- The nonlinear medium have no free charge
- The medium have no free current
- the material is non-magnetic, hence $\tilde{B} = \mu_o \tilde{H}$.

By considering the above assumptions, we have written the Maxwell's below.

$$\nabla \cdot \tilde{D} = 0 \quad (2.10)$$

$$\nabla \cdot \tilde{B} = 0 \quad (2.11)$$

$$\nabla \times \tilde{E} = -\frac{\partial \tilde{B}}{\partial t} \quad (2.12)$$

$$\nabla \times \tilde{H} = \frac{\partial \tilde{D}}{\partial t} \quad (2.13)$$

The wave equation can be derived from the Maxwell's equation by taking the curl of equation 2.12 as,

$$\nabla \times \nabla \times \tilde{E} + \mu_0 \frac{\partial^2}{\partial t^2} \tilde{D} = 0 \quad (2.14)$$

In terms of polarization equation 2.14 can be written as;

$$\nabla \times \nabla \times \tilde{E} + \frac{1}{c^2} \frac{\partial^2}{\partial t^2} \tilde{E} = -\frac{1}{\epsilon_0 c^2} \frac{\partial^2 \tilde{P}}{\partial t^2} \quad (2.15)$$

Hence equation 2.15 can be written in a simplified manner using the vector identity as,

$$\nabla^2 \tilde{E} - \frac{1}{c^2} \frac{\partial^2}{\partial t^2} \tilde{E} = \frac{1}{\epsilon_0 c^2} \frac{\partial^2 \tilde{P}}{\partial t^2} \quad (2.16)$$

In the equation 2.16 the polarization refers to the linear and the nonlinear contribution as well.

$$\tilde{P} = \tilde{P}^{(1)} + \tilde{P}^{NL} \quad (2.17)$$

Hence, the general expression of the wave equation could be expressed as,

$$\nabla^2 \tilde{E} - \frac{\epsilon^{(1)}}{c^2} \frac{\partial^2 \tilde{E}}{\partial t^2} = \frac{1}{\epsilon_0 c^2} \frac{\partial^2 \tilde{P}^{NL}}{\partial t^2} \quad (2.18)$$

In Eq. 2.18 the nonlinear optical response on the right hand side acts as the source term for the nonlinear process. Hence, in the absence of nonlinear response, the wave equation yields a solution for a wave with velocity $c/\sqrt{\epsilon^{(1)}}$. In case, the medium is dispersive

medium, each frequency component must be studied separately. Hence, Eq. 2.18 could be analyzed for each frequency component separately as,

$$\nabla^2 \tilde{E}_n - \frac{\epsilon^{(1)}(\omega_n)}{c^2} \cdot \frac{\partial^2 \tilde{E}_n}{\partial t^2} = \frac{1}{\epsilon_0 c^2} \frac{\partial^2 \tilde{P}_n^{NL}}{\partial t^2} \quad (2.19)$$

The above equation could be used to study the interaction of three waves in presence of non-zero $\chi^{(2)}$ which is the motivation of the present thesis. By considering the most general form of three-wave mixing as the SFG, the following mathematical framework could be developed. As described in the previous section, the SFG could be represented mathematically as $\omega_s + \omega_i = \omega_p$. The electric field associated with the applied field *i.e.* for ω_i and ω_s is given by;

$$\tilde{E}_i(z, t) = E_i e^{-i\omega_i t} + c.c. \quad \text{where } E_i = A_i e^{ik_i z} \quad (2.20)$$

In the above representation, *i* refers to signal (*s*) and idler (*i*) wave. And the nonlinear polarization associated with the SFG field could be represented as;

$$\tilde{P}_p(z, t) = P_p e^{-i\omega_p t} + c.c. \quad (2.21)$$

and

$$P_p = 4\epsilon_0 d_{eff} E_s E_i \quad (2.22)$$

Hence, the nonlinear polarization amplitude is

$$P_p = 4\epsilon_0 d_{eff} A_s A_i e^{i(k_s + k_i)z} \quad (2.23)$$

By taking into account the field at sum-frequency wavelength,

$$\tilde{E}_p(z, t) = A_3(z) e^{i(k_p z - \omega t)} + c.c. \quad (2.24)$$

where $k_p = \frac{n_p \omega_p}{c}$, $n_p^2 = \epsilon^{(1)}(\omega_p)$ and the generated field is a slowly varying function of z . This could be considered as a trial solution to Eq. 2.19. Also, we assume that all

the interacting waves are plane-waves. Hence, by substituting 2.24, 2.23 and 2.21 into Eq. 2.19, we could express the wave equation as,

$$\left[\frac{d^2 A_p}{dz^2} + 2ik_p \frac{dA_p}{dz} - k_p^2 A_p + \frac{\epsilon^{(1)}(\omega_p)\omega_p^2 A_p}{c^2} \right] e^{i(k_p z - \omega_p t)} + c.c. = \frac{-4d_{eff}\omega_p^2}{c^2} A_s A_i e^{i[(k_s + K_i)z - \omega_p t]} + c.c. \quad (2.25)$$

Equation 2.25 could be further simplified to,

$$\frac{d^2 A_p}{dz^2} + 2ik_p \frac{dA_p}{dz} = \frac{-4d_{eff}\omega_p^2}{c^2} A_s A_i e^{i(k_s + k_i - k_p)z} \quad (2.26)$$

By taking into account the slowly varying amplitude approximation,

$$\left| \frac{d^2 A_p}{dz^2} \right| \ll \left| k_p \frac{dA_p}{dz} \right| \quad (2.27)$$

This condition signifies that a fractional change in A_p in a distance of the wavelength must be much smaller than unity. Hence, Eq. 2.26 becomes;

$$\frac{dA_p}{dz} = \frac{2id_{eff}\omega_p}{n_p c} A_s A_i e^{i\Delta k z} \quad (2.28)$$

where n_p represents the refractive index of pump waves and Δk could be defined as;

$$\Delta k = k_s + k_i - k_p \quad (2.29)$$

which is generally known as the wavevector phase-mismatch. In a similar manner, the equations depicting the evolution of waves at frequencies ω_s and ω_i are,

$$\frac{dA_s}{dz} = \frac{2id_{eff}\omega_s}{n_s c} A_p A_i^* e^{-i\Delta k z} \quad (2.30)$$

and

$$\frac{dA_i}{dz} = \frac{2id_{eff}\omega_i}{n_i c} A_p A_s^* e^{-i\Delta k z} \quad (2.31)$$

Equation 2.28, 2.29 and 2.30 are the coupled-wave equations where the amplitude of the interacting waves exhibit a mutual dependence. A direct inference from the coupled-mode equations is when $\Delta k = 0$. In that case, the amplitude of the generated waves will

increase linearly provided that the other two wave amplitude are constant. In general, with finite values of Δk and by considering constant amplitude of A_s and A_i , the SFG intensity at the nonlinear crystal output is given by,

$$I_p = \frac{2d_{eff}^2 \omega_3^2 I_s I_i}{n_p n_s n_i \epsilon_0 c^3} L^2 \text{sinc}^2\left(\frac{\Delta k L}{2}\right) \quad (2.32)$$

From Eqs. 2.32, the phase-mismatch term is appearing as a ‘sinc’ function. Hence, the efficiency of three-wave mixing process reduces as the value of phase mismatch term (Δk) increases. It is worthwhile to point that the value of I_p is zero when the ‘sine’ term (numerator of the ‘sinc’ function) in the expression is zero *i.e.* at $L = \frac{2\pi}{\Delta k}$. It could be pointed that for a finite value of the phase mismatch, I_p follow the sinusoidal trajectory. In other words, the output power increases up to a length $\frac{\pi}{\Delta k}$ and then decreases. This length is called the coherence length (L_{coh}). In other words, we can say that, if Δk have finite value, this is the maximum value of I_p which could be obtained provided the crystal length is an integral multiple of L_{coh} .

2.4 Phase-matching condition

For an efficient three-wave mixing process $\Delta k \approx 0$ must be satisfied. In this picture, the nonlinear polarization and the generated field must be in phase. As a result the waves generating at each point along the crystal length must add up constructively, resulting in an efficient generation. Taking this into account, the dispersive nature of the medium at the frequencies of these three interacting waves would result into an expression for $\Delta k = 0$ given by,

$$\frac{n_p(\lambda_p)}{\lambda_p} = \frac{n_s(\lambda_s)}{\lambda_s} + \frac{n_i(\lambda_i)}{\lambda_i} \quad (2.33)$$

Here, the wavelength dependent refractive index is obtained from the Sellmeier’s equation [14, 23, 24, 25]. This equation provide an insight in to the wavelength as well temperature dependence of refractive index. These two factors plays a crucial role in satisfying phase

matching criteria. By manipulating the material characteristics, the phase matching condition can be satisfied. In the present discussion, we have noted that the refractive index of the nonlinear medium is wavelength and temperature dependent. Hence, by exploiting these characteristics, a tuned wavelength in a broad spectral bandwidth could be achieved. This is the key point for frequency tuning the OPOs in the frame of obtaining a wide spectral range of the coherent output. Several phase matching techniques have been employed to satisfying the phase matching condition such as birefringent and quasi-phase matching [24, 26]. In birefringent phase-matching, the anisotropic properties of a nonlinear crystal is employed to achieve $\Delta k = 0$ condition. On the other hand, quasi-phase-matching (QPM) uses the ferroelectric properties of the nonlinear crystal for achieving the phase-matching between the interacting waves.

2.4.1 Birefringent phase-matching

In a few nonlinear crystals, the refractive index is a function of crystallographic axis. As a result, by using waves with different electromagnetic polarization, the phase mismatch could be compensated [1, 8, 27]. In anisotropic medium the refractive index have different values along different principal axes. According to crystal orientation, they could be categorized as;

$$n_x = n_y = n_z \quad \textit{Isotropic} \quad (2.34)$$

$$n_x = n_y \neq n_z \quad \textit{Uniaxial} \quad (2.35)$$

$$n_x \neq n_y \neq n_z \quad \textit{Biaxial} \quad (2.36)$$

In the uniaxial orientation, the crystals have one optic-axis. Consider the optic-axis is along the $z - direction$ *i.e.* for a wave propagating in the $z - direction$, the wave sees the same refractive index in the x and the y direction. Therefore, the x or y -polarized waves are called the ordinary waves. On the other hand, the wave propagating in the xz -plane or yz -

plane have an angular dependence of the refractive index. The angular dependence of the refractive index is given by

$$\frac{1}{n_e(\theta)^2} = \frac{\sin^2\theta}{\tilde{n}_e^2} + \frac{\cos^2\theta}{n_o^2} \quad (2.37)$$

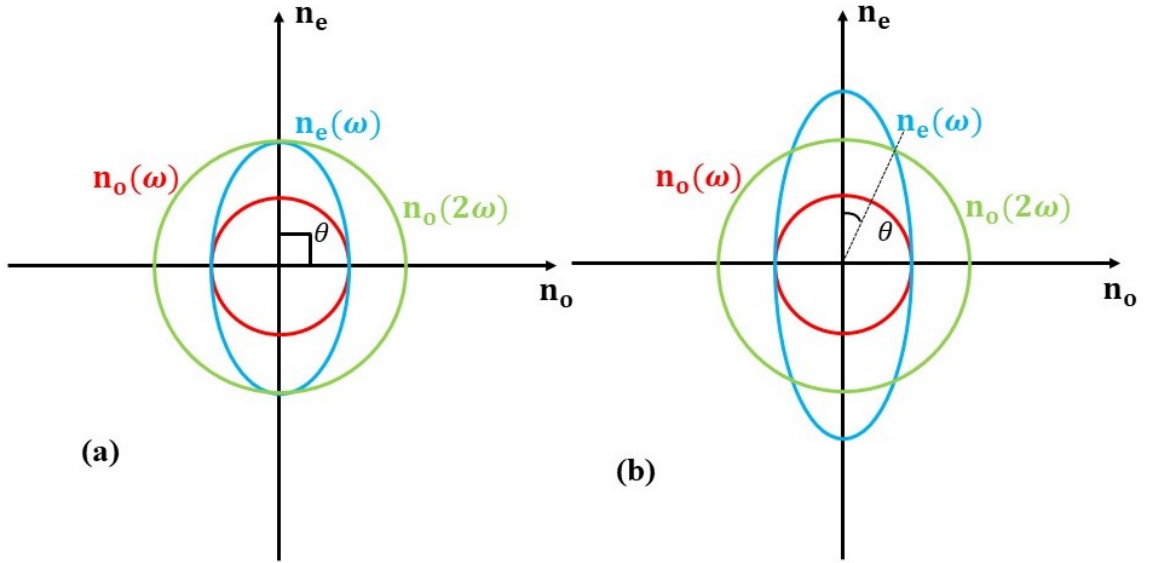


Figure 2.3: Refractive index representation for birefringent crystal (a) non-critical phase matching, (b) critical phase matching

Here n_o represents the ordinary refractive index and \tilde{n}_e is the principal value of the extraordinary refractive index. Hence, the phase-matching condition for a desired wave could be obtained by adjusting the θ value. It is interesting to note that in spite of the phase matching condition is satisfied for the interaction, the particular d -tensor component must have non-zero value to couple the fundamental wave to the nonlinear polarization. Generally, the angle dependent phase matching condition is categorized in to two types, critical and non-critical phase matching. This consideration could be visualized by taking the example of second harmonic generation (SHG). The SHG process is represented pictorially in the figure 2.3. From figure 2.3 (b), it is evident that a small deviation from the phase matching angle results in significant value of Δk , hence it is called critical phase matching. On the other hand when $\theta = 90^\circ$, the inner circle is tangential to the ellipse and small deviation

in phase-matching θ is not critical for changing Δk . In this case, the phase-matching condition is called noncritical phase matching. For the noncritical phase-matching condition temperature dependent refractive index plays a crucial role as the phase matching angle have a fixed value. In case of critical phase matching, the pointing-vector direction for the generated wave and that for the incident wave are not same when the phase-matching angle change(2.3 (b)). Hence, this results in a walk-off between the incident and the generated wave and the walk off angle is given by,

$$\tan \rho = \frac{\tan \theta \left(\frac{n_o^2}{n_e^2} - 1 \right)}{1 + \frac{n_o^2}{n_e^2} \tan^2 \theta} \quad (2.38)$$

The interaction length before the walk-off is defined as,

$$L_{int} = \frac{\sqrt{\pi} w_o}{\rho} \quad (2.39)$$

where w_o is the beam waist. Hence, for a tightly focused beam, even for a smaller value of the walk off angle could lead to walk off after a small distance. Hence, the gain for the nonlinear process reduces. However, the walk-off in case of the non-critical phase matching is absent. Hence, the nonlinear process could occur over the entire crystal length.

2.5 Quasi-Phase-Matching

Certain crystals like GaAs, gallium nitride, Zinc Telluride, are weakly anisotropic as well as exhibit second-order nonlinearity [28, 29, 30, 31, 32]. Interesting route proposed by N. Bloembergen that, by allowing the nonlinear coefficient (d) to vary periodically with a period of $2L_{coh}$, the phase matching could be achieved [33, 34].

Hence, we could say that the nonlinear polarization changes its sign at every coherence length as the nonlinear polarization is proportional to nonlinear coefficient (d) (figure 2.4) [30, 28, 33]. Through this route, the fundamental wave(s) and the nonlinear polarization can be forced to be in phase by changing the sign of nonlinear polarization. Hence,

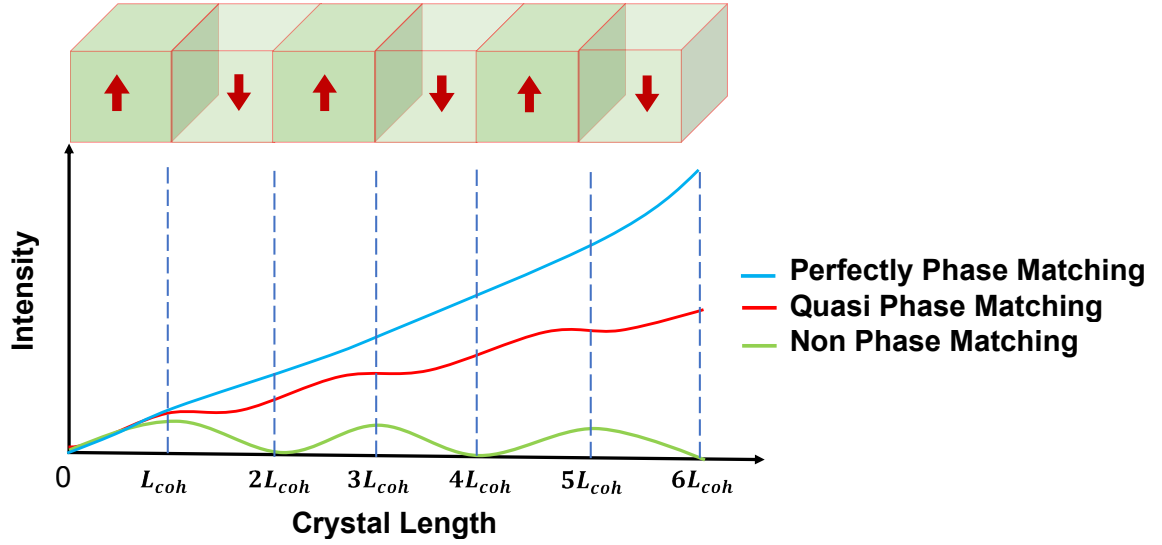


Figure 2.4: Schematic of QPM structure and the process representing intensity of output waves for birefringent phase-matched condition in blue, quasi-phase-matching in red, and non phase-matching in green.

the efficiency of generation increases instead of following a sinusoidal trajectory. Also, in this case, the value of effective nonlinear coefficient decreases. Hence, the QPM efficiency for the materials do not follow the same trajectory as that of a perfectly phase matched condition. The periodic modulation of the nonlinear coefficient gives rise to an additional K -vector that facilitates the phase-matching. This technique could be adopted to achieve phase-matching even if the medium is isotropic. Such possibilities arise in ferroelectric crystals that have domains. The direction of polarization of domains is inverted periodically with a period Λ which inverts the sign of the nonlinear coefficient d periodically with a period Λ . In such a scenario, the nonlinear coefficient could be represented as

$$\begin{aligned}
 d(z) &= +d & |z| < \frac{L_{coh}}{2} \\
 &= -d & \frac{L_{coh}}{2} < |z| < \frac{\Lambda}{2}
 \end{aligned} \tag{2.40}$$

Hence, the mathematical description of quasi-phase matching could be written in terms of Fourier series as,

$$d(z) = d_{eff} \sum_{m=-\infty}^{\infty} G_m e^{(ik_m z)} \quad (2.41)$$

where, $k_m = \frac{2\pi m}{\Lambda}$ is the magnitude of the grating with m^{th} Fourier component of the nonlinear coefficient.

$$G_m = \left(\frac{2}{m\pi} \right) \sin \left(\frac{m\pi}{2} \right) \quad (2.42)$$

If we consider the generated amplitude for SFG process, and compare the A_p for birefringence and the QPM process, they are related through

$$A_{p,QPM} = \frac{2}{\pi} A_{p,birefringence} \quad (2.43)$$

Hence, in QPM, there is a reduction of amplitude of the generated beam, by a factor of $\frac{2}{\pi}$. We have observed that there is a decrease in [d_m (nonlinear coupling coefficient of the m^{th} order Fourier term)], when we use the higher order Fourier components. Hence, we could get an efficient generation for first order ($m=1$) term. Hence,

$$d_1 = \frac{2}{\pi} d_{eff} \quad (2.44)$$

Hence, the wave vector mismatch incorporating k_m could be written as,

$$\begin{aligned} \Delta k_m &= k_s + k_i - k_p + k_m \\ &= k_s + k_i - k_p + \frac{2\pi}{\Lambda} \end{aligned} \quad (2.45)$$

The periodicity required for QPM of any order is;

$$\Lambda = \frac{2\pi}{k_s + k_i + k_p} = 2L_{coh} \quad (2.46)$$

2.5.1 Techniques to achieve QPM

Ferroelectric materials such as $LiNbO_3$, $LiTaO_3$, $KTiOPO_4$ exhibits spontaneous polarization below the Curie temperature in the absence of an external electric field. These

crystals could be poled periodically by aligning the direction of spontaneous polarization [29, 35, 36]. Hence, these nonlinear crystals are called periodically-poled or periodically domain inverted. The widely used technique for the domain inversion is applying periodic electrode on the surface of crystal. A uniform electrode is applied to the opposite surface. Hence, by the application of sufficiently high electric field to the electrodes, periodically-poled crystals could grown. The maximum thickness of the nonlinear crystal could go through this process is determined by the dielectric breakdown of the medium. The crystal's maximum thickness during this process is limited by the dielectric breakdown of the medium.

Another approach for achieving the poling structure is to include a periodic domain structure during the growth of the crystal. It is technically very difficult to grow crystals with very small grating period.

The domain inversion in certain crystals could also be achieved by diffusing certain ions in to the medium at elevated temperature.

2.6 Frequency conversion process and amplification

The $\chi^{(2)}$ frequency conversion process involves the interaction of three waves termed as, pump (ω_p), signal (ω_s) and idler (ω_i) in a nonlinear medium. When a highly intense pump beam is incident on a medium with non-zero $\chi^{(2)}$ along with a weak signal wave, an idler beam at ω_i frequency is spontaneously generated.

$$\omega_p = \omega_s + \omega_i \quad (2.47)$$

If the signal beam could be optimally fed back to the nonlinear crystal then one could construct an optical parametric oscillator. Hence, the amplification of beam at ω_s frequency and the generation of idler beam at ω_i frequency could be obtained by solving the coupled differential equation 2.30 and 2.31. In this case, we have assumed low depletion of the

pump beam.

$$\frac{dA_p}{dz} = 0 \quad (2.48)$$

The solution of the differential equation is given by,

$$A_s(z) = \left[A_s(0) \left(\cosh gz - \frac{i\Delta k}{2g} \sinh gz \right) + \frac{\kappa_s}{g} A_i^*(0) \sinh gz \right] e^{\frac{i\Delta k z}{2}} \quad (2.49)$$

$$A_i(z) = \left[A_i(0) \left(\cosh gz - \frac{i\Delta k}{2g} \sinh gz \right) + \frac{\kappa_s}{g} A_s^*(0) \sinh gz \right] e^{\frac{i\Delta k z}{2}} \quad (2.50)$$

where $\Delta k = k_p - k_s - k_i$ as described earlier and

$$g = \left[\kappa_s \kappa_i^* - \left(\frac{\Delta k}{2} \right)^2 \right]^{\frac{1}{2}} \quad (2.51)$$

$$\kappa_i = \frac{2i\omega_i^2 d_{eff} A_p}{k_i c^2} \quad (2.52)$$

By considering the initial condition as $A_i = 0$ and A_s is finite then the gain associated with the signal beam for a crystal of length L could be expressed as;

$$G_s(L) = \frac{I_s(z=L)}{I_s(z=0)} - 1 = \Gamma^2 L^2 \frac{\sinh^2 \left[\Gamma^2 L^2 - \left(\frac{\Delta k L}{2} \right)^2 \right]^{\frac{1}{2}}}{\left[\Gamma^2 L^2 - \left(\frac{\Delta k L}{2} \right)^2 \right]} \quad (2.53)$$

Here, I_i is the intensity represented as,

$$I_j = \frac{n_j c \epsilon_0 |A_j|^2}{2} \quad (2.54)$$

Here j corresponds to pump, signal and idler and

$$\Gamma^2 = \frac{8\pi^2 d_{eff}^2}{c \epsilon_0 n_p n_s n_i \lambda_s \lambda_i} I_p(0) \quad (2.55)$$

The gain factor in Eq. 2.55 could also be represented as;

$$\frac{8\pi^2 d_{eff}^2}{c \epsilon_0 n_p n_o \lambda_o^2} (1 - \delta^2) I_p(0) \quad (2.56)$$

where the degeneracy term δ is defined as

$$1 + \delta = \frac{\lambda_o}{\lambda_s}; \quad 1 - \delta = \frac{\lambda_o}{\lambda_i} \quad (0 \leq \delta \leq 1) \quad (2.57)$$

where the degenerate wavelength is defined as $\lambda_o = 2\lambda_p$ and n_o refers to the wavelength at degeneracy. It is worthwhile to point that the gain associated with the parametric process is maximum at the degeneracy and the gain decreases when the spectral separation between the signal and idler increases. Hence, for phase-matched condition ($\Delta k = 0$), the gain associated with the signal beam could be written as;

$$G_s(L) = \sinh^2(\Gamma L) \quad (2.58)$$

Hence, at low gain *i.e.* for $\Gamma L \lesssim 1$, the gain approximates to,

$$G_s(L) \cong \Gamma^2 L^2 \quad (2.59)$$

We could observe that, in low gain regime, the signal gain increases quadratically. For high gain situation *i.e.* $\Gamma L \gg 1$, the gain reduces to;

$$G_s(L) \cong \frac{1}{4} e^{2\Gamma L} \quad (2.60)$$

In the high gain regime, the signal gain exhibits an exponential growth as a function of length L .

2.7 Optical parametric oscillator

The output from a frequency conversion process could be maximized in an oscillator configuration. Hence, the nonlinear medium is placed within an optical cavity to provide feedback at the desired wavelength [11]. Hence, a desired wave is allowed to successive pass through the nonlinear medium and a coherent output could be obtained. Consider a simple cavity design shown in Fig. 2.5. This represents a linear cavity configuration where

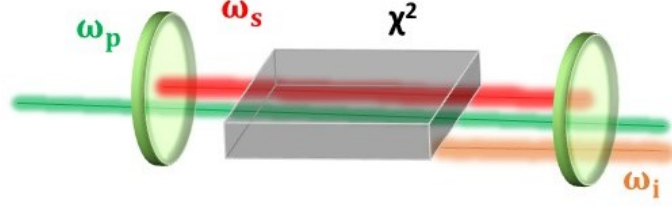


Figure 2.5: Linear cavity representing singly resonant OPO

the nonlinear crystal is placed inside a pair of mirrors. In the present condition, the mirrors are highly reflecting for the signal beam and transmits the pump as well as the idler beam. To begin with, the signal and idler waves are generated spontaneously from the pump wave. The losses in the cavity arises from components of the cavity.

- Mirror :The cavity mirrors are not 100% reflecting for the signal beam
- Nonlinear crystal :The crystal have it own absorption due to its composition and the wavelength range at which it is operating

It is worthwhile to point that when the gain of the resonating wave is equal to the cavity loss then the signal oscillation begins. Hence, by considering the reflection loss and scattering loss inside the crystal and double-pass in the crystal for one round-trip, the signal and idler amplitude could be represented as,

$$A_{s,o} = \sqrt{R_{a,s}R_{b,s}}e^{-2\alpha_s L}A_s(L) = \rho_s A_s(L) \quad (2.61)$$

$$A_{i,o} = \sqrt{R_{a,i}R_{b,i}}e^{-2\alpha_i L}A_i(L) = \rho_i A_i(L) \quad (2.62)$$

where ρ is defined as

$$\rho_m = \sqrt{R_{a,m}R_{b,m}}e^{-2\alpha_m L} \quad (2.63)$$

and m refers to the signal and idler beams. Here, R_a and R_b refers to the reflectivity of the two mirrors. By relating Eqs. 2.61 and 2.62 with Eqs. 2.49 and 2.50, the resonance

condition could be written as,

$$\Gamma^2(1 - \rho_i \cosh(\gamma L))(1 - \rho_s \cosh(\gamma L)) = \kappa_i \kappa_s^* \rho_s \rho_i \sinh^2(\Gamma L) \quad (2.64)$$

By using definitions $\Gamma^2 = \kappa_s^* \kappa_i$ and $\cosh^2(L) - \sinh^2(L) = 1$, the resonance condition reduces to,

$$\cosh(\Gamma L) \geq \frac{1 + \rho_s \rho_i}{\rho_s + \rho_i} \quad (2.65)$$

For undepleted pump, the gain is very small *i.e.* $\Gamma L \ll 1$, hence the resonator condition reduces to;

$$\frac{(\Gamma L)^2}{2} \geq \frac{(1 - \rho_s)(1 - \rho_i)}{\rho_s + \rho_i} \quad (2.66)$$

Hence by putting the value of Γ and by considering $I_p = P_p/A$, where A refers to the cross-sectional area of beam and P_p is pump power, the threshold for OPO is,

$$P_{TH} \geq A \frac{n_p n_s n_i \epsilon_o c \lambda_s \lambda_i}{4\pi^2 d_{eff}^2 L^2} \frac{(1 - \rho_s)(1 - \rho_i)}{\rho_s + \rho_i} \quad (2.67)$$

where A refers to the cross-sectional area. Hence, the threshold condition is given by,

$$P_{TH} \geq A \frac{n_p n_s n_i \epsilon_o c \lambda_p^2}{\pi^2 d_{eff}^2 L^2 (1 - \delta^2)} \frac{(1 - \rho_s)(1 - \rho_i)}{\rho_s + \rho_i} \quad (2.68)$$

Equations 2.68 shows that the threshold for OPO depends on the reflectivity of mirrors, length of the crystal, nonlinear coefficient and optical absorption for the nonlinear crystal.

2.7.1 Laser pump source

The pump source must be sufficiently intense, so that the nonlinear gain for achieving OPO threshold is obtained [8, 1]. The spectral and spatial coherence of the pump beam also plays a crucial role. It is worthwhile to point that the practical laser sources have finite spectral bandwidth as well as spatial divergence. Hence, it is very difficult to satisfy the phase matching condition for all the spectral and spatial components of the beam simultaneously.

This results in a non-zero value of Δk within which the parametric gain is significant. Subsequently, this limits the maximum pump spectral width that could be utilized for frequency conversion process.

2.7.2 Nonlinear crystal

The nonlinear crystal plays a crucial role in successful implementation of the OPO. The desired characteristics of the nonlinear crystal depends on various factors such as; broad transparency range satisfying the phase matching condition, large nonlinear coefficient, high optical damage threshold, small spatial walk-off [11]. The gain associated with the parametric process have a direct dependence on the nonlinear coefficient d_{eff} and have inversely related to the square root of refractive indices at the interacting wavelengths. These two factors could be used to define the figure of merit (FOM) for the nonlinear crystal.

$$FOM \equiv \frac{d_{eff}}{\sqrt{n_p n_s n_i}} \quad (2.69)$$

The nonlinear crystal should possess high tolerance to a small changes in spectral and spatial property of the pump beam. These tolerances are associated with the nonlinear crystal and could be measured in terms of spectral and angular acceptance bandwidth of the crystal. These factors basically depends on the rate of change of phase mismatch with the wavelength and the angular spread of the pump beam. One could derive these factors from the Taylor series expansion of the phase-mismatch term. A brief description is provided in section 2.9.

2.7.3 Cavity mirrors

Cavity mirrors plays a crucial role in OPOs. They provide feedback to stimulate the three-wave interaction process and hence, assist in improving the frequency conversion efficiency [37, 38]. In SROs, for example, one of the three interacting waves, say the signal

wave is forced to oscillate inside the cavity. In that case, the cavity mirrors would be designed such that they are highly reflecting ($R > 99.9\%$) for the signal wave. For the pump and the idler wave, the cavity mirrors are highly transmitting ($T > 99.9\%$). Hence, a strong idler beam could be coupled-out of the cavity. In a similar manner, the cavity mirrors could be designed to get DRO and TRO (discussed in details in 2.10).

2.8 Wavelength tuning

One of the greatest advantage associated with OPO is to generate a widely tunable sources [39, 28, 23, 40]. This could be achieved by manipulating various parameters that help in satisfying the phase matching condition. The phase matching condition depends on refractive index of the nonlinear crystal at different wavelengths. The Sellemier's relation defines the variation in refractive index of the medium as a function of wavelength and temperature. A general Sellmeir's equation for an optically transparent medium is given by,

$$n^2(\lambda) = B_o + \frac{\lambda^2 B_1}{\lambda^2 - \lambda_1^2} + \frac{\lambda^2 B_2}{\lambda^2 - \lambda_2^2} \quad (2.70)$$

where B_o , B_1 , B_2 , λ_1 and λ_2 are the fitting constants and the wavelength (λ) is expressed in μm -unit. Hence, for an SRO, the signal and idler wavelength could be tuned using various techniques mentioned below.

- Temperature tuning: Variation of signal/idler wavelength as a function of crystal temperature.
- Angle tuning: As described in section 2.5.1, the phase-matching could be satisfied at different wavelengths by utilizing the non-critical phase-matching in anisotropic crystals.
- Changing the grating period in quasi phase-matching: A crystal containing multiple

grating periods can be translated laterally to change Λ and hence the signal and idler wavelengths

2.9 Phase matching bandwidth

The factors which determine the nonlinear gain are input laser wavelength, spatio-temporal coherence of the laser beam along with the temperature-dependent dispersive properties of the crystal. These factors play a crucial role in deciding the tolerance for the phase matching process for deriving appreciable gain. Quantitatively, these factors could be ascertained by observing their impact on the optical power of the frequency converted beam. Suppose X defines the factor and a change in X by ΔX leads to a 50% drop in optical power (or efficiency) with respect to its maximum value. Since, X or ΔX dictates the variation of Δk , therefor a Taylor series expansion of Δk (about $\Delta k = 0$) would allow us to determine the actual dependency on the drop in efficiency. If the frequency conversion efficiency is governed through a *sinc* function then the phase matching bandwidth is determined by the full-width-half-maximum (FWHM) of the *sinc*² function *i.e.*

$$\text{sinc}^2\left(\frac{\Delta k L}{2}\right) \geq 0.5 \quad (2.71)$$

$$\Delta X_{FWHM} = 2 \frac{0.886\pi}{L \left| \frac{\partial \Delta k}{\partial X} \right|} \quad (2.72)$$

It is apparent that the crystal length plays a crucial role in determining the bandwidth *i.e.* longer the interaction length the narrower the phase-matching bandwidth.

2.9.1 Temperature bandwidth

The temperature bandwidth is defined as the range of temperatures over which the conversion process is efficient. Hence,

$$\Delta T_{FWHM} = \frac{0.443}{L \left| \frac{1}{\lambda_p} \frac{\partial n_p}{\partial T} - \frac{1}{\lambda_s} \frac{\partial n_s}{\partial T} - \frac{1}{\lambda_i} \frac{\partial n_i}{\partial T} \right|} \quad (2.73)$$

The temperature tuning bandwidth becomes large when the denominator of 2.73 approaches to zero *i.e.* near degeneracy.

2.10 Optical Parametric Oscillators (OPOs)

The OPOs are resonant cavities for signal or the idler or both so as to provide a suitable feedback to the optical parametric amplification process. Accordingly, the mirrors are designed to strongly reflect one or more beams involved in the three-wave mixing process. According to the reflectivity of the mirrors, the OPO cavities are categorized into three types namely, singly resonant OPO (SRO), Doubly resonant OPO (DRO) and Triply resonant OPO (TRO) OPO [41, 42].

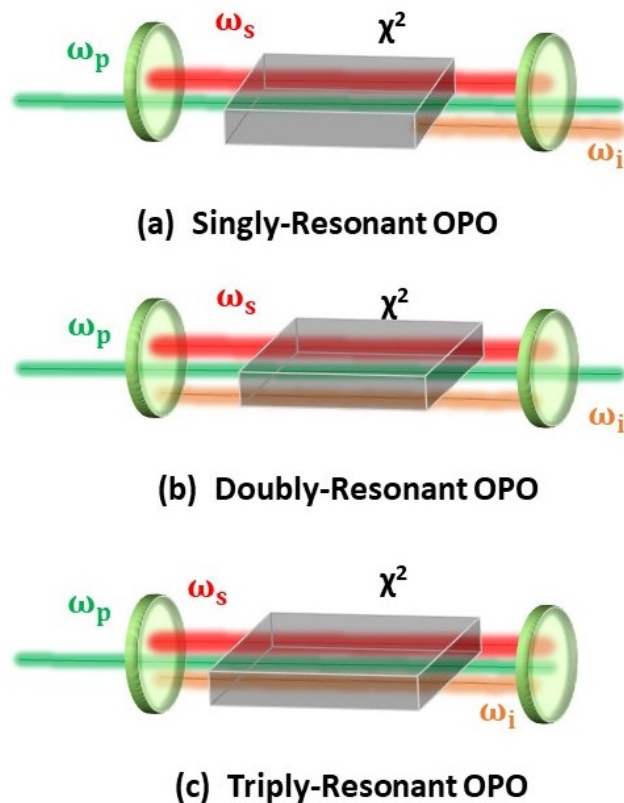


Figure 2.6: Types of cavity configuration of a linear cavity OPO (a) Singly resonant OPO (b) Doubly resonant OPO (c) Triply resonant OPO

In SRO, one of the three interacting waves is made to oscillate within the cavity (figure 2.6 (a)). The threshold pump required to begin signal or idler oscillation in an SRO is maximum ($\mathcal{O}(1 - 10W)$) [11]. In order to reduce the threshold pump power, both the signal and idler beams in the OPO are made to oscillate within the cavity. This configuration is termed as the DRO (figure 2.6 (b)). It is also possible to make the pump beam oscillate within the cavity in addition to the signal and idler. This configuration of OPO is known as TRO (figure 2.6 (c)). The TROs offer the lowest threshold as compared to SRO and DRO. However, stable oscillation in DRO and TRO is challenging, as the required resonance condition for more than one number of waves must be fulfilled simultaneously within the same cavity. Despite the highest pump threshold, SROs offer the most viable solution for generating high-power and tunable radiation over a wide spectral band. Here, we mainly discuss the SRO which is relevant to the present work. Figure 2.7(a) illustrates the typical cavity configurations for SRO devices. The linear cavity configuration is the simplest one which comprises nonlinear crystal enclosed by two mirrors.

Figure 2.7 (b)-(d) represents a few variants for the OPO cavities. The linear, X- and V-cavities (Fig. 2.7 (a), (b) and (d)) are standing-wave cavities. The ring cavity configuration (Fig. 2.7 (c)) is a travelling-wave cavity. Standing wave cavities are suitable choice of ultrafast OPO architectures. Due to the fact that the synchronization of pump pulse and the oscillating beam could be easily achieved. The standing wave cavity could obtain the gain only when the oscillating beam and the pump beam are co-propagating and the oscillating signal suffers loss when it is counter-propagating with respect to the pump beam. The travelling-wave cavities provide advantage in terms of isolating the back-reflection of pump as well as facilitates unidirectional propagation of all the beams.

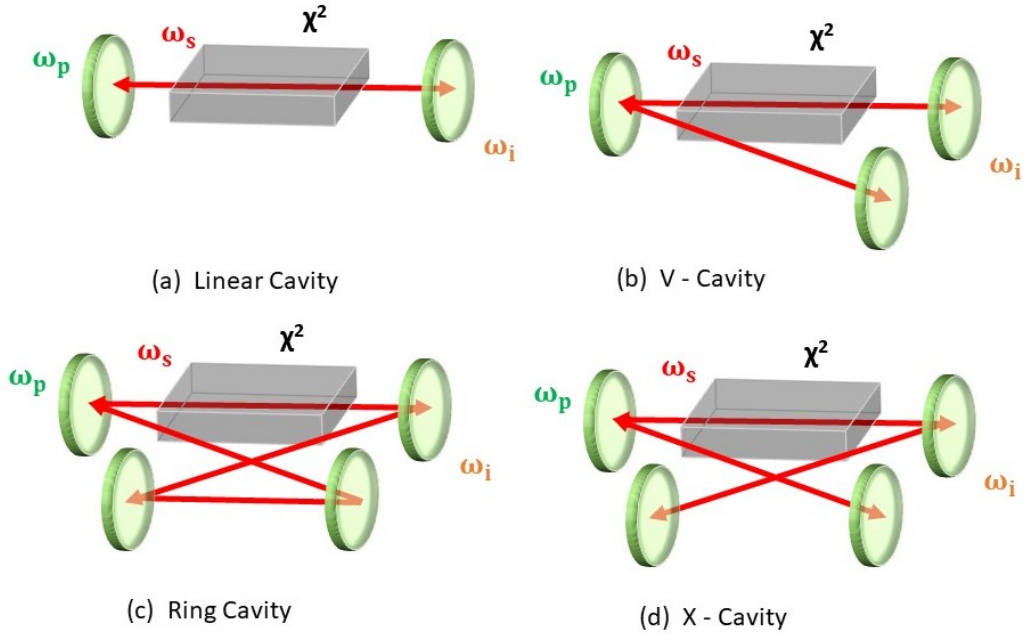


Figure 2.7: OPO cavity designs (a) Linear cavity, (b) V-cavity, (c) Ring cavity, and (d) X-cavity

2.11 Cavity design and ABCD matrix method

The working of the OPO is dependent on the optimum cavity design *i.e* the selection of cavity mirrors, separation between them in a particular cavity setting. The Gaussian beam propagation inside the cavity could be understood through the ABCD matrix approach [43]. The Gaussian beam propagation in the cavity begins with an initial beam diameter defined as,

$$\frac{1}{q} = \frac{1}{R} - \frac{i\lambda}{\pi n w_0^2} \quad (2.74)$$

Here, R refers to the radius of curvature and w_0 is the spot size of beam which is $1/e$ drop in amplitude. is the $1/e^{th}$ drop in intensity of the beam in transverse direction. By considering a symmetric cavity configuration where the beam waist is located at the crystal center and accordingly the radius of curvature at the crystal center is infinite, the Gaussian

beam parameter is expressed as,

$$q_o = i \frac{\pi n w_o^2}{\lambda} \quad (2.75)$$

For stable oscillations, the beam waist at the crystal center should be identical after one round-trip.

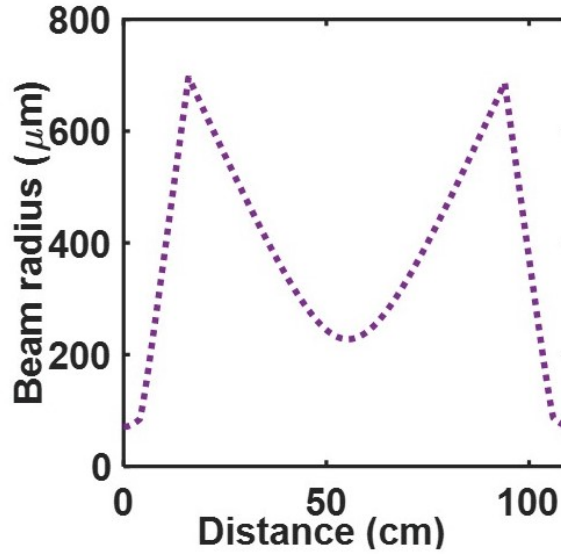


Figure 2.8: Variation of resonating beam radius as the beam propagates inside the cavity. The distance axis starts from the center of the crystal and the beam path is as presented in figure 2.7(d)

For a better understanding, we consider a ring resonator configuration as shown in figure 2.7(c). For this experimental configuration, we have considered the beam waist at the center of the crystal is $75\mu\text{m}$ and for a stable resonating condition the beam waist at the center of the crystal must be same after every round trip of the resonating beam. Therefore, after each round trip, the beam waist at the crystal center should be $75\mu\text{m}$. In this given configuration, we are using a 80 mm long *PPLN* crystal. This corresponds to an optimum focusing parameter $\xi \approx 1$. The resonating signal wavelength is assumed to be 1570 nm . The refractive index of the crystal at 100°C crystal temperature is 2.14. Hence, the beam waist of signal at different positions of a stable ring cavity is thus calculated using the Gaussian

beam parameter and the ABCD matrix at each component of the resonator cavity. Hence the beam waist of signal at different positions of a stable ring cavity is thus calculated and can be plotted shown in figure 2.8.

2.12 Conclusion

In conclusion, this chapter has provided a comprehensive overview of nonlinear optical processes, including SFG, SHG, DFG, OPG, and OPO. The efficiency and effectiveness of these processes heavily rely on satisfying the phase matching condition. QPM has emerged as an exceptional alternative for achieving phase matching in nonlinear optical processes. By introducing periodic modulation in the nonlinear crystal's properties, QPM enables access to higher nonlinear coefficients, expanding the range of achievable wavelengths and enhancing the efficiency and tunability of OPOs. OPO, in particular, stands out as a versatile and powerful technique, offering coherent and tunable light across a wide range of wavelengths. OPO finds extensive utility in various scientific and technological domains, including spectroscopy, quantum optics, and laser engineering. The enhanced phase matching capabilities provided by QPM further enhance the efficiency and performance of OPO systems.

References

- [1] W. P. Risk, W. P. Risk, T. Gosnell, and A. Nurmikko, *Compact blue-green lasers*. Cambridge University Press, 2003.
- [2] R. Minck, R. Terhune, and C. Wang, “Nonlinear optics,” *Applied optics*, vol. 5, no. 10, pp. 1595–1612, 1966.
- [3] E. Sauter, *Nonlinear optics*, vol. 44. John Wiley & Sons, 1996.
- [4] Y.-R. Shen, *Principles of nonlinear optics*. Wiley-Interscience, New York, NY, USA, 1984.
- [5] A. Yariv, *Quantum electronics*. John Wiley & Sons, 1989.
- [6] G. Boyd and A. Ashkin, “Theory of parametric oscillator threshold with single-mode optical masers and observation of amplification in linb o 3,” *Physical review*, vol. 146, no. 1, p. 187, 1966.
- [7] G. Boyd and D. Kleinman, “Parametric interaction of focused gaussian light beams,” *Journal of Applied Physics*, vol. 39, no. 8, pp. 3597–3639, 1968.
- [8] J. Giordmaine, “Mixing of light beams in crystals,” *Physical Review Letters*, vol. 8, no. 1, p. 19, 1962.
- [9] S. E. Harris, “Tunable optical parametric oscillators,” *Proceedings of the IEEE*, vol. 57, no. 12, pp. 2096–2113, 1969.
- [10] P. Maker, R. Terhune, M. Nisenoff, and C. Savage, “Effects of dispersion and focusing on the production of optical harmonics,” *Physical review letters*, vol. 8, no. 1, p. 21, 1962.

-
- [11] M. Ebrahim-Zadeh, “Continuous-wave optical parametric oscillators,” *Handbook of Optics*, vol. 4, pp. 1–33, 2010.
- [12] R. W. Boyd, *Nonlinear optics*. Academic press, 2020.
- [13] P. E. Powers and J. W. Haus, *Fundamentals of nonlinear optics*. CRC press, 2017.
- [14] V. G. Dmitriev, G. G. Gurzadyan, and D. N. Nikogosyan, *Handbook of nonlinear optical crystals*, vol. 64. Springer, 2013.
- [15] P. N. Butcher and D. Cotter, *The elements of nonlinear optics*. Cambridge university press, 1990.
- [16] W. Louisell, A. Yariv, and A. Siegman, “Quantum fluctuations and noise in parametric processes. i.,” *Physical Review*, vol. 124, no. 6, p. 1646, 1961.
- [17] J. Gordon, W. H. Louisell, and L. R. Walker, “Quantum fluctuations and noise in parametric processes. ii,” *Physical Review*, vol. 129, no. 1, p. 481, 1963.
- [18] P. D. Drummond and M. Hillery, *The quantum theory of nonlinear optics*. Cambridge University Press, 2014.
- [19] R. L. Byer, “Optical parametric oscillators,” *Quantum electronics: A treatise*, vol. 1, no. part B, 1975.
- [20] R. Smith, “Optical parametric oscillators,” *In: Lasers. Volume 4.(A76-39776 19-36) New York*, vol. 4, pp. 189–307, 1976.
- [21] R. Byer, M. Oshman, J. Young, and S. Harris, “Visible cw parametric oscillator,” *Applied Physics Letters*, vol. 13, no. 3, pp. 109–111, 1968.
- [22] G. F. Koster, J. O. Dimmock, R. G. Wheeler, and H. Statz, *Properties of the thirty-two point groups*, vol. 24. MIT press Cambridge, MA, 1963.

-
- [23] M. Hobden, D. Robertson, P. Davies, K. Hulme, J. Warner, and J. Midwinter, "Properties of a phase-matchable nonlinear optical crystal: Potassium dithionate," *Physics Letters*, vol. 22, no. 1, pp. 65–66, 1966.
- [24] D. H. Jundt, "Temperature-dependent sellmeier equation for the index of refraction, n_e , in congruent lithium niobate," *Optics letters*, vol. 22, no. 20, pp. 1553–1555, 1997.
- [25] B. E. Saleh and M. C. Teich, *Fundamentals of photonics*. John Wiley & sons, 2019.
- [26] G. Edwards and M. Lawrence, "A temperature-dependent dispersion equation for congruently grown lithium niobate," *Optical and quantum electronics*, vol. 16, pp. 373–375, 1984.
- [27] D. A. Kleinman, "Nonlinear dielectric polarization in optical media," *Physical Review*, vol. 126, no. 6, p. 1977, 1962.
- [28] M. M. Fejer, G. Magel, D. H. Jundt, and R. L. Byer, "Quasi-phase-matched second harmonic generation: tuning and tolerances," *IEEE Journal of quantum electronics*, vol. 28, no. 11, pp. 2631–2654, 1992.
- [29] L. Gordon, G. Woods, R. Eckardt, R. Route, R. Feigelson, M. Fejer, and R. Byer, "Diffusion-bonded stacked gaas for quasiphase-matched second-harmonic generation of a carbon dioxide laser," *Electronics Letters*, vol. 22, no. 29, pp. 1942–1944, 1993.
- [30] G. D. Miller, *Periodically poled lithium niobate: modeling, fabrication, and nonlinear optical performance*. Stanford university, 1998.
- [31] L. E. Myers, R. Eckardt, M. Fejer, R. Byer, W. Bosenberg, and J. Pierce, "Quasi-phase-matched optical parametric oscillators in bulk periodically poled $linbo_3$," *JOSA B*, vol. 12, no. 11, pp. 2102–2116, 1995.

-
- [32] P. Powers, T. J. Kulp, and S. Bisson, “Continuous tuning of a continuous-wave periodically poled lithium niobate optical parametric oscillator by use of a fan-out grating design,” *Optics letters*, vol. 23, no. 3, pp. 159–161, 1998.
- [33] N. Bloembergen and A. Sievers, “Nonlinear optical properties of periodic laminar structures,” *Applied Physics Letters*, vol. 17, no. 11, pp. 483–486, 1970.
- [34] J. Armstrong, N. Bloembergen, J. Ducuing, and P. S. Pershan, “Interactions between light waves in a nonlinear dielectric,” *Physical review*, vol. 127, no. 6, p. 1918, 1962.
- [35] K. L. Vodopyanov, O. Levi, P. Kuo, T. Pinguet, J. Harris, M. Fejer, B. Gerard, L. Becouarn, and E. Lallier, “Optical parametric oscillation in quasi-phase-matched gaas,” *Optics letters*, vol. 29, no. 16, pp. 1912–1914, 2004.
- [36] L. E. Myers, R. Eckardt, M. M. Fejer, R. L. Byer, and W. R. Bosenberg, “Multigrating quasi-phase-matched optical parametric oscillator in periodically poled linbo 3,” *Optics letters*, vol. 21, no. 8, pp. 591–593, 1996.
- [37] R. Byer and S. Harris, “Power and bandwidth of spontaneous parametric emission,” *Physical Review*, vol. 168, no. 3, p. 1064, 1968.
- [38] R. Byer, A. Kovrigin, and J. Young, “A cw ring-cavity parametric oscillator,” *Applied Physics Letters*, vol. 15, no. 5, pp. 136–137, 1969.
- [39] R. L. Sutherland, *Handbook of nonlinear optics*. CRC press, 2003.
- [40] M. Hobden and J. Warner, “The temperature dependence of the refractive indices of pure lithium niobate,” *Physics Letters*, vol. 22, no. 3, pp. 243–244, 1966.
- [41] J. Bjorkholm, “Some spectral properties of doubly and singly resonant pulsed optical parametric oscillators,” *Applied Physics Letters*, vol. 13, no. 12, pp. 399–401, 1968.

- [42] J. Bjorkholm, “Analysis of the doubly resonant optical parametric oscillator without power-dependent reflections,” *IEEE Journal of Quantum Electronics*, vol. 5, no. 6, pp. 293–295, 1969.
- [43] O. Svelto, D. C. Hanna, *et al.*, *Principles of lasers*, vol. 1. Springer, 2010.

Chapter 3

Study of thermo-optic effects in singly-resonant optical parametric oscillator

3.1 Motivation

OPOs are versatile and widely-tunable coherent high power sources, exhibiting potential to cover the conventionally inaccessible segments of *em* spectrum. The generated wavelengths in different spectral bands lead to a variety of applications ranging from spectroscopy and medical science to security purposes. The high-resolution infrared (IR) spectroscopy has been employed for non-invasive investigation of the neural activity as well as to monitor the quality of seeds for quality evaluation [1, 2, 3, 4, 5]. Continuous-wave (CW) SROs generating wavelength in near-IR (NIR) to mid-IR (MIR) spectral band could find important applications in high-resolution gas-phase spectroscopy and trace-gas sensing as a result of the fact that a wide range of gas molecules have fundamental absorption lines and overtones for the rotational-vibrational states in this regime [6, 7, 8]. Tunable IR sources are the crucial component of remote sensing technology [9]. Conventional NIR laser diode sources provide a monolithically integrated architecture but they possess a limited tunability in wavelength [10]. Diode laser sources based on lead-salt offers tunability from $\approx 3.0 - 30 \mu\text{m}$ [11, 12]. However, its operations are limited due to bad beam quality and low output power. In addition, the requirement of cryogenic cooling for the operation makes these sources substantially complicated [13]. Another available IR source is Quantum cascade lasers (QCLs) covering the spectral range from $\approx 3.5 - 24.0 \mu\text{m}$ [14]. QCLs

exhibit very limited wavelength tunability which dictated by the gain-bandwidth offered by the intra-band transitions in a semiconductor lasing medium [15, 16].

On the other hand, CW OPOs exhibit continuous wavelength tunability ($\geq 100 \text{ nm}$) along with high power ($\geq 1 \text{ W}$) delivery. In addition, they deliver beams with Gaussian spatial mode. The CW OPOs are based on resonant power enhancement for signal beam generated in an OPG process inside a nonlinear crystal having non-zero second-order nonlinear susceptibility. A wide range of nonlinear crystals have been investigated till today. Amongst these, SROs based on $LiNbO_3$, $LiTaO_3$ and $KTiOPO_4$ are extensively used for single-frequency NIR (1400-1700 nm) and MIR (2400 – 4000 nm) generation. A long-length periodically-poled (PP) nonlinear crystal could facilitate phase-matched generation over extended interaction length that could generate high-power frequency converted beams [17]. For SRO sources working in the MIR regime, periodically-poled $LiNbO_3$ (PPLN) is widely used for the nonlinear frequency conversion process due to its high d_{33} ($\approx 25 \text{ pm/V}$) [18]. However, the PPLN based SROs pumped by visible laser sources (400-800 nm) exhibit a low photorefractive damage threshold and therefore, rendered unsuitable when pumped by high-power ($\geq 2 \text{ W}$) lasers in the visible band (400-800 nm) [19]. In addition, in these pumping regions, green induced infrared absorption (GRIIRA) is predominant in a PPLN crystal. Owing to these causes, the pump sources in the visible region have limited performance in SROs based on $LiNbO_3$ [19]. MgO-doping in $LiNbO_3$ have tried reduce the limitation but still, it is still far from being rendered insignificant in the high pump power regimes [20]. In this context, the stoichiometrically grown $LiTaO_3$ based SROs have been shown perform exceptionally well owing to high damage threshold, low optical absorption and high thermal conductivity [20, 21]. The $LiTaO_3$ crystals possess transparency in ultraviolet band and are highly resistant to the photorefractive damage [22, 23]. It is also worth pointing out that the thermo-optic effects are significantly suppressed in the stoichiometric variant of $LiTaO_3$. However, long length fabrication of PP

$LiTaO_3$ (PPLT) crystals is challenging and therefore, the congruently-grown variants of PPLT are being explored. In the present chapter, the thermo-optic manifestations inside the congruently-grown PPLT (cPPLT) crystal is explored using an SRO configuration.

3.2 Experimental configuration

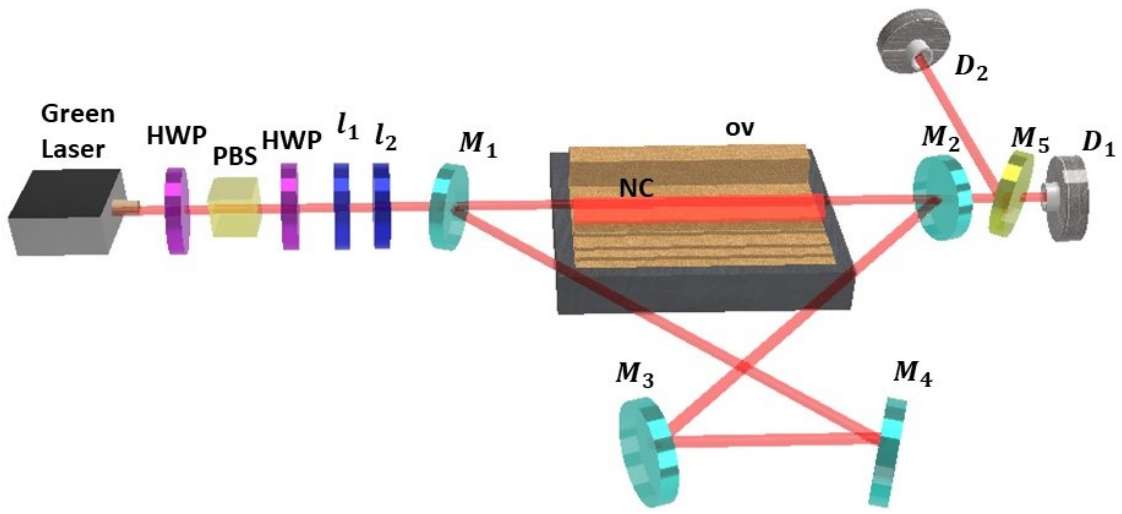


Figure 3.1: A schematic of the experimental set-up for MgO:cPPLT SRO; HWP: Half-wave plate, PBS: Polarizing beam-splitter, l_1 : Concave lens, l_2 : Convex lens, $M_{1,2,3,4}$: Curved mirrors forming the cavity, OV: Temperature controlled oven housing the nonlinear crystal, NC: Nonlinear crystal (MgO:cPPLT), M_5 : Dichroic Mirror, $D_{1,2}$: Thermal Detectors

The schematic of the experimental setup for the MgO-doped congruently-grown PPLT (MgO:PPLT) SRO is shown in figure 3.1. The fundamental pump source is a continuous-wave fiber laser (IPG-GLR-20-SF) delivering a linearly-polarized beam having wavelength (λ) = 532 nm. The green beam has $M^2 < 1.2$, with linewidth $\Delta\nu \leq 1MHz$. The input power of the laser is controlled by a pair of half wave plate (HWP) and a polarizing beam splitter (PBS). A second HWP is required to manage the polarization of the beam required to achieve the phase matching condition, which helps to get access to the highest nonlinear coefficient. A suitable combination of lenses comprising of a concave lens ($f = -100mm$) and convex lens ($f = 100 mm$) are used to get a desired beam waist at the center of the

crystal satisfying the criteria set by Boyd-Kleinmann theory of frequency conversion using Gaussian beam. The mirrors M_1, M_2, M_3 and M_4 are the cavity mirrors, among which M_1 and M_2 are curved mirrors (-100 mm radius of curvature) Mirrors M_3 and M_4 are plane mirrors. All four mirrors are highly reflective ($R > 99\%$) for the wavelength between 710-850 nm *i.e.* for the signal beam. The mirrors are highly transmitting for 532 nm and 1600-1950 nm wavelength bands. Hence, these are highly transmitting for the pump and the idler beam. A dichroic mirror (M_5) separates the pump beam from the idler beam. The nonlinear crystal used in SRO cavity is 8 – mol% MgO doped cPPLT crystal (HC-Photonics Taiwan). The nonlinear crystal is 50 mm long having a rectangular aperture with dimension 2mm \times 0.5mm. The poling period of the grating is $\Lambda = 9.1\mu\text{m}$. The crystal faces are anti-reflection coated for pump, signal and idler wavelengths. The MgO:cPPLT crystal is housed inside a oven whose temperature could be varied from 20°C to 200°C in steps of 0.1°C

3.3 Results and Discussion

We started the SRO characterization with $w_0 = 30\mu\text{m}$ beam waist leading to Boyd-Kleinman (B-K) focusing parameter $\xi \approx 2.1$. The threshold of the SRO is $P_{p(th)} \approx 500$ mW at oven temperature $T_{ov} = 50^\circ\text{C}$. The observation of small SRO threshold could be attributed to the high *single-pass* gain in MgO:cPPLT crystal owing to an optimum value of ξ ($= 2.84$) [24]. However, the SRO output saturates at pump power $P_p \approx 1.2$ W. The maximum observed idler power is $P_{i(max)} \approx 200$ mW. In this SRO configuration, the thermal-lensing effect is predominant for $P_p \geq 1.4$ W. Consequently the signal oscillation stops and the SRO stops to operate when the pump power P_p goes beyond 1.5 W. In order to achieve SRO operation at high pump powers, we increased the beam waist to $w_0 = 60\mu\text{m}$ having $\xi \approx 0.5$. Hence, the threshold of oscillation increases to $P_{th} \approx 2.1$

W at the crystal oven temperature $T_{ov} = 50^\circ C$. We have observed the P_{th} almost remains same across the entire wavelength tuning range.

3.3.1 Wavelength Tuning

We have observed the wavelength tunability of the SRO by changing the oven temperature. By changing the oven temperature from $50^\circ C$ to $160^\circ C$ at a fixed pump power of $P_p \approx 3.4 W$, the idler wavelength could be coarsely tuned from 1815 nm-1920 nm (see Fig. 3.2). The average value of the idler power (over the entire tuning range) is $\approx 470 mW$. Also, we have observed a drop in idler power at higher oven temperatures. The drop in SRO idler power could be attributed to,

- i Operation at wavelengths significantly away from degeneracy [17]
- ii Non-uniformity in mirror coating and anti-reflection coating for MgO:cPPLT crystal
- iii Thermo-optic behavior of the nonlinear crystal at the higher temperature

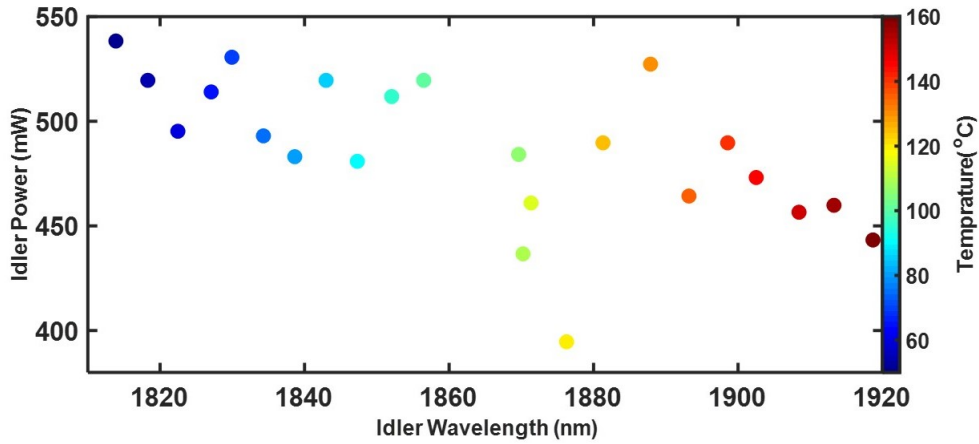


Figure 3.2: Variation of idler power as a function of MgO:cPPLT crystal temperature (for $P_p \approx 3 W$ and $w_0 \approx 60 \mu m$)

Amongst the above-mentioned factors, argument (iii) plays an effective role in the drop of the efficiency since argument (i) and (ii) could contribute to 10 – 15% in the

efficiency drop. The efficiency drop is significantly influenced by the argument (iii) as both arguments (i) and (ii) collectively contribute to a 10-15 % reduction in efficiency. In the later section of this chapter, we will discuss the impact of thermo-optic effects on the generated beam.

3.3.2 Power Scaling

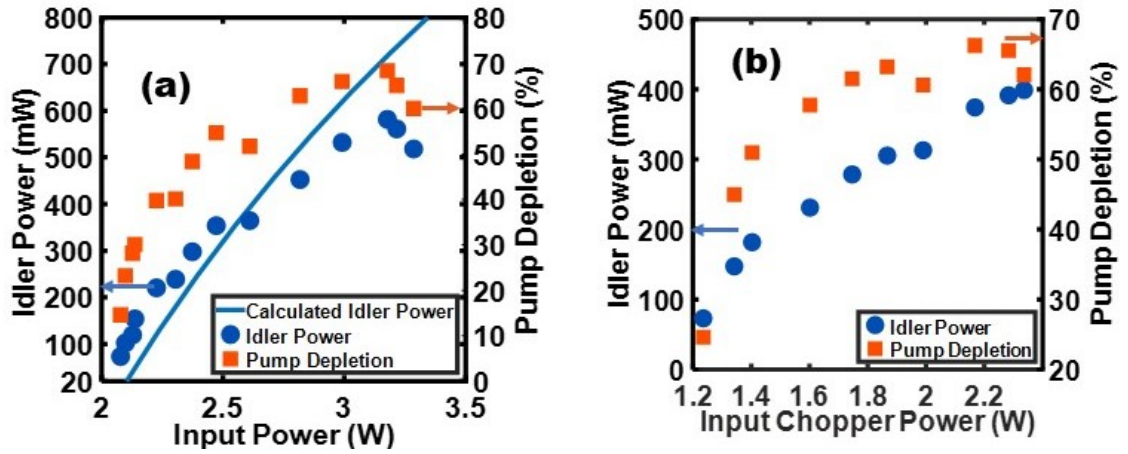


Figure 3.3: (a) Variation of idler power and pump depletion (in %) as a function of pump power (at crystal temperature $T = 50^\circ C$ and $w_0 \approx 60\mu m$) (b) Variation of idler power and pump depletion (in %) as a function pump power ($w_0 = 60\mu m$) at fixed chopper frequency of 530 Hz.

In the entire wavelength tuning range at fixed P_p , the maximum P_i is obtained at $T_{ov} = 50^\circ C$ (in figure 3.2). At this oven temperature, we have performed the power scaling of the SRO by varying the P_p shown in Fig. 3.3(a). The P_i increases with an increase in P_p . But we have observed saturation in P_i when $P_{p(sat)} \approx 3.1$ W and tends to drop for $P_p \geq 3.4$ W. From the observations in Fig. 3.3(a), it could be inferred that the saturation in idler power (P_i) sets in when $P_{p(sat)}/P_{p(th)} \approx 1.5$. For further investigation, we have carried out the observation of pump depletion with P_p . Pump depletion is the percentage representation of the ratio between the leftover P_p after the nonlinear generation process to the input P_p . The leftover power from the SRO could be collected with the dichroic mirror

M_5 , which separates the pump from the idler beam. A similar saturation effect could also be observed for the pump depletion shown in figure 3.3(a), which tends to flatten around 65 – 70%. In the theoretical aspect, we could represent the variation of P_i generation with P_p (for moderately focused beams) is governed by the relation [25]

$$P_i(z = L) = \frac{w_{0i}^2 \lambda_p}{w_{0p}^2 \lambda_i} \sin^2(\Gamma) P_p(z = 0) \quad (3.1)$$

where

$$\frac{\sin^2 \Gamma}{\Gamma^2} = \frac{P_{p(th)}}{P_p} \quad (3.2)$$

By taking into account the experimental parameters we have simulated the variation in P_i with P_p shown by the solid line in Fig. 3.3(a). shown by the solid line in Fig. 3.3(a). We have observed a close relevance between the experimental measurement and the simulated result up to $P_p \leq 3.0 W$.

3.3.3 Thermo-optic manifestations

With a view to obtain deeper insight on the idler power saturation and subsequent back-conversion, we investigated the impact of pump (green) beam towards the manifestation of photo-thermal effects in MgO:cPPLT crystal. Although, the crystal thermal load tends to reduce when the pump beam-waist increase from $w_0 = 30 \mu m$ to $w_0 = 60 \mu m$, it is far from being insignificant. In order to ascertain the role of thermo-optic effects, we have chopped the CW pump beam periodically at a frequency of 530 Hz mechanical chopper with 50% duty-cycle. Chopping of the pump beam decreases the average power. Hence the threshold for SRO operation with average P_p is $P_{p(th)} = \approx 1.2 W$, and the average output is $P_{i(max)} \approx 400 mW$. In this configuration maximum depleted pump power is of $\approx 65\%$ as shown in figure 3.3(b). From the observations, it has been observed that, although the idler power does not exhibit any saturation up to $P_p \approx 2.4 W$, the variation is not linear. In addition, the pump depletion exhibits a peak (near 2.2 W average pump power) and tends to

drop when the pump increases further. The slope change in idler power as well as pump depletion for a quasi CW beam are distinct signature of back-conversion (to pump) in the SRO owing to thermo-optic effects. The *thermo-optic* effects in MgO:cPPLT crystal essentially include

- i Thermal-dephasing (longitudinal wavevector mismatch)
- ii Thermal-lensing (or wavefront distortion)

In view of drawing more information regarding the photothermal effects we have carried a systematic comparison between the stoichiometric and the congruent variant of the $LiTaO_3$ nonlinear crystal. We note that congruently-grown $LiTaO_3$ (cPPLT) exhibits the following properties in comparison with the stoichiometrically-grown variant.

- i Low thermal conductivity (K)
- ii High absorption in the visible and the NIR band
- iii Large thermo-optic coefficient ($\frac{dn}{dT}$)

The thermal conductivity determines the rate of heat (energy) flow from a source to the surrounding (or sink) over a given length of the medium which is kept at a known temperature. At room temperature $K_{(cPPLT)} = 4.4$ W/mK and ($K_{(sPPLT)} = 8.5$ W/mK). Here we could observe that thermal conductivity value of sPPLT orientation is about twice the value of cPPLT. In CW high-power operation, this plays a crucial role in efficiently dissipate the generated heat (near the crystal center) to the sink (oven). Hence, the smaller value of k for cPPLT prohibits the heat transfer leading to accumulation of heat in the bulk of crystal, thereby increasing phase-mismatch (Δk). In our experimental setup we have measured the linear optical absorption (α_{cPPLT}) at 532 nm for the cPPLT crystal along the propagation length of 50 mm. The measured value of α_{cPPLT} by varying P_p from 2.0-4.5

W is $\approx 0.082 \text{ cm}^{-1}$. The value of α_{sPPLT} is $\approx 0.03 \text{ cm}^{-1}$ and is three times smaller than α_{cPPLT} [26]. In order to appreciate the cumulative impact of absorption of pump (green) and thermal conductivity on phase-matching, we solve the heat conduction equation given by,

$$\frac{d^2T}{dz^2} = -\frac{\alpha_p I_p}{K} \quad (3.3)$$

We have considered the temperature of the crystal faces to be $T = 90^\circ C$ at $z = \pm \frac{L}{2}$ (assuming $z = 0$ is at the crystal center) as the boundary condition. We have solved the differential equation along the propagation direction. We adopt a simulation technique which is identical to that prescribed by O. A. Louchev *et al.* It is worthwhile to point that the heat differential equation is dependent on the intensity. The intensity variation along the propagation direction (along z -direction) has a dominant contribution from change in Gaussian beam radius ($w(z)$). [27]. Hence, we have simulated the variation of temperature along the crystal length using the differential equation considering the above mentioned boundary condition. The simulation results along the z -direction is shown in 3.4(a,b), where the colour map

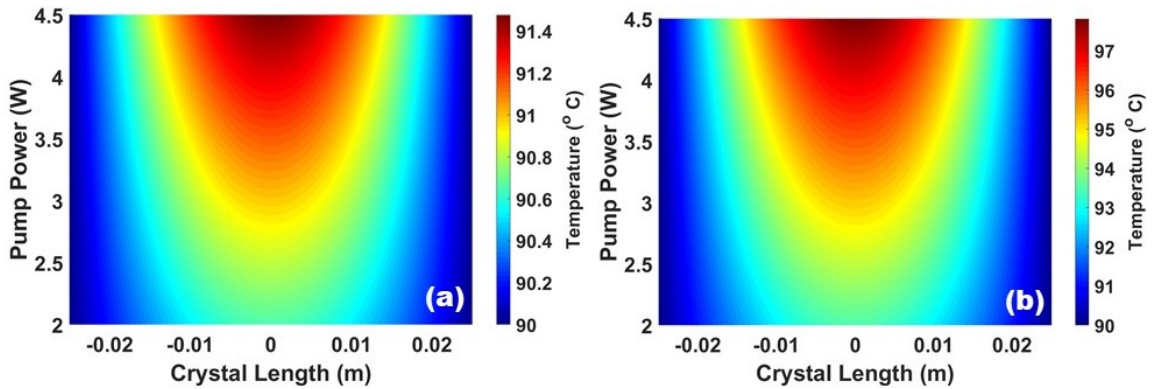


Figure 3.4: Simulated variation of temperature within the crystal (colour-code) as a function of length and pump power (varying from 2 – 4.5 W) (a) for sPPLT, (b) for cPPLT.

represents the change in temperature. It is apparent that the rise in temperature (for maximum input P_p) at the crystal center for cPPLT is about $97^\circ C$ and it is significantly higher ($\Delta T_{max} \approx 7^\circ C$) as compared to that for sPPLT ($\Delta T_{max} \approx 2^\circ C$). Hence there is a rise in

temperature locally. This increment in temperature could lead to a change in ‘ $\Delta k(T) - K$ ’ in each period of the periodically poled crystal. Here, $\Delta k(T) = \frac{[\omega_p n_p(T) - \omega_s n_s(T) - \omega_i n_i(T)]}{c}$ is the phase-mismatch, $K = \frac{2\pi}{\Lambda}$ is the 1st-order grating constant and n_p, n_s, n_i are (extraordinary) refractive index for the crystal at the pump, signal and idler wavelengths respectively. Hence, the cumulative phase mismatch determines the effective interaction of the nonlinear medium obeying the relation,

$$\Sigma \Delta k(T) \Lambda - K L_{eff} = \pi \quad (3.4)$$

Here, the summation is carried over all the grating elements present within the length ‘ L_{eff} ’ and is given by the relation;

$$L_{eff} = \frac{\pi}{(\Delta k)_{max}} \quad (3.5)$$

where $(\Delta k)_{max}$ represents the maximum value of the phase mismatch that inhibits the pump to idler conversion beyond L_{eff} . In terms of *Taylor series* expansion Δk could be represented as;

$$\Delta k \approx \Delta k|_{T=T_{PM}} + \frac{\partial \Delta k}{\partial T}|_{T=T_{PM}} \Delta T \quad (3.6)$$

where,

$$\frac{\partial \Delta k}{\partial T}|_{T=T_{PM}} = \frac{1}{c} [\omega_p \frac{\partial n_p}{\partial T}|_{T=T_{PM}} - \omega_s \frac{\partial n_s}{\partial T}|_{T=T_{PM}} - (\omega_p - \omega_s) \frac{\partial n_i}{\partial T}|_{T=T_{PM}}] \quad (3.7)$$

Hence, we could observe that the crystal length exceeding L_{eff} would not be contributing to idler-power generation. On the other hand, when the crystal is sufficiently long, the cumulative impact of back-conversion and linear absorption (in the region $L > L_{eff}$) could reduce the idler power as the pump power increases. Using the relation 3.5 and 3.6, we have calculated value of L_{eff} , which varies from 18 mm to 19 mm for pump power level varying from 2.2 W to 3.5 W. By altering the focusing conditions, L_{eff} could be varied over a wider range. From a comparison in between Figs. 3.4(a) and (b), it is apparent

that ΔT (at $z=0$) is substantially higher in cPPLT as compared to sPPLT. From the material dispersion, $\frac{\partial \Delta k_{max}}{\partial T}|_{cPPLT} = 0.0023 /m/^{\circ}C$ and $\frac{\partial \Delta k_{max}}{\partial T}|_{sPPLT} = 0.0017 /m/^{\circ}C$ which leads to $\frac{L_{eff}(sPPLT)}{L_{eff}(cPPLT)} \approx 10$ [28]. This point to the saturation in in idler (for cPPLT) is expected at nominal pump powers. It is worth pointing out that idler power saturation in $MgO : sPPLT$ based SRO has not been observed up to $P_p \approx 9 W$ (with pump at $\lambda = 532 nm$ wavelength) [29]. The contribution of Gaussian pump beam intensity in the variation of crystal temperature along the transverse direction could be understood explicitly as follows. In figure 3.5(a) and (b), a temperature map representing the maximum

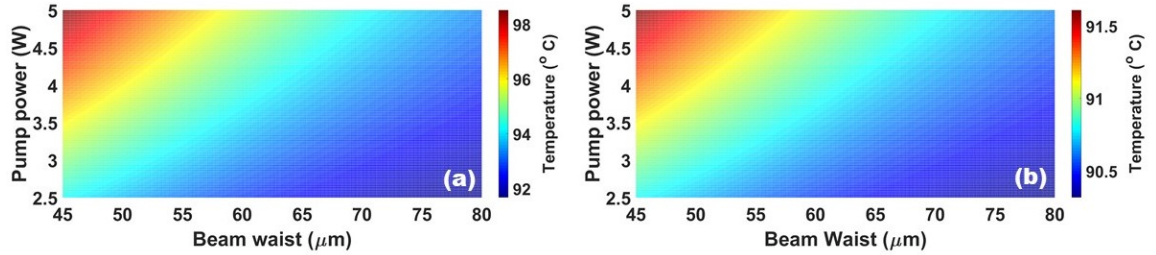


Figure 3.5: Maximum temperature (represented by the colour map) at the crystal center ($z=0$) at different pump beam waist and pump power for (a) MgO:cPPLT (b) MgO:sPPLT. The crystal oven temperature is assumed to be 90°

temperature attained (at $z = 0$ in figure 3.5 in 50 mm -long MgO:cPPLT and MgO:sPPLT crystal when the pump power and the pump beam-waist is varied. The oven temperature (T_{ov}) is assumed to be fixed at 90° . It is apparent that the maximum change in crystal temperature (at $z = 0$) is much smaller in MgO:sPPLT for a given pump beam-waist. Also, the thermal load on the crystal (for a given pump power) could be reduced by increasing the pump beam-waist. For example, the maximum rise in crystal temperature is appreciably small ($\approx +1.0^{\circ}$) for an incident pump power of 5.0 W when the pump beam waist is $\geq 75 \mu m$ (see figure 3.5(a)). The maximum rise in crystal temperature (with respect to T_{ov}) determines the maximum change in refractive index through the thermo-optic coefficient *i.e.* dn/dT [30, 28]. The thermo-optic coefficient for MgO:cPPLT is $4.5 \times 10^{-5} K^{-1}$ and

that for MgO:sPPLT is $0.2 \times 10^{-5} K^{-1}$ [28]. This implies a greater change in refractive index of MgO:cPPLT when an identical change in temperature takes place in MgO:cPPLT and MgO:sPPLT crystal. A map of longitudinal variation in Δk at different pump power levels is represented in Figs. 3.6(a) (for MgO:cPPLT) and (b) (for MgO:sPPLT). This figure has been simulated assuming an oven-temperature (T_{ov}) of 90° and pump wavelength of $\lambda_p = 532 \text{ nm}$. A comparison of Δk yields an order of magnitude higher values in MgO:cPPLT crystal (figure 3.6(a)) with respect to that estimated in the MgO:sPPLT crystal. In fact, the impact on $\Delta k(z)$ at higher pump power is highly significant in MgO:cPPLT and its role is discernibly reflected in figure 3.3(a) where the idler power tends to reduce for $P_p \geq 5 \text{ W}$. On the other hand, MgO:sPPLT exhibits a much weaker z-dependence of Δk and the idler power saturation has not been observed for pump power up to 10 W [21]. In addition, local heating in MgO:cPPLT could also have contributions from

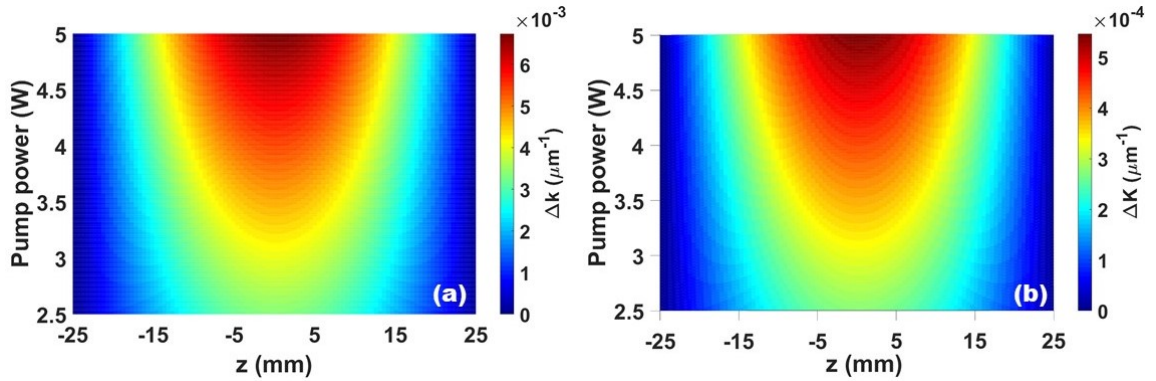


Figure 3.6: Colour-map (simulated) represents the longitudinal (z) variation of phase-mismatch (Δk) as a function of incident pump power for (a) MgO:cPPLT (b) MgO:sPPLT. The crystal oven temperature is assumed to be 90°

- i green-induced infrared absorption (GRIIRA)
- ii Nonlinear (two-photon) absorption (β)

We have performed the GRIIRA by measuring the transmitted power at 1064 nm wavelength in presence of a orthogonally-polarized high-power beam at 532 nm wavelength

(≈ 6 KW peak power). We observed that the 1064 nm wavelength transmission increases linearly in the entire measurement range. This observation rules out the contribution of heating from GRIIRA. This is consistent with the investigations on light-induced absorption in congruently-grown $LiTaO_3$ carried out by S. Alexandrovski *et al.* [31, 32]. We

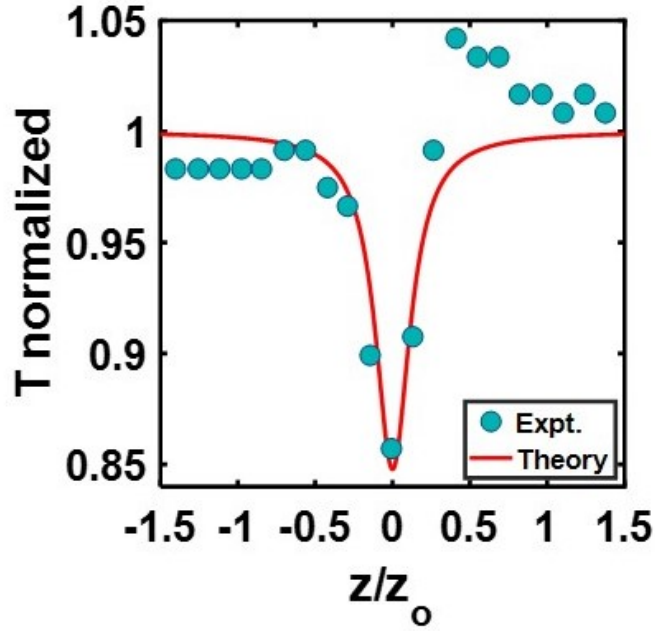


Figure 3.7: Normalized open aperture Z-scan transmission trace of MgO:cPPLT

have explored the possibility of thermo-optic manifestations due to nonlinear absorption. For this, we carried out the open-aperture (OA) Z-scan transmittance for a 0.5 mm thick slice of MgO:cPPLT [33]. For the Z-scan measurement, we have used a frequency-doubled high energy, ultrashort pulse laser (Cazadero-1030, Calmar, US) operating at 1030 nm and delivering ≈ 350 fs pulses at 1 kHz repetition rate. For the frequency-doubling process, we have used a 4 mm long birefringent crystal LiB_3O_5 (LBO). Figure 3.7 represents the normalized intensity along the scanning length. The scanning length is normalized with the *Rayleigh* range. By adopting the recipe prescribed by S. Bahae *et al.* [33], the nonlinear absorption coefficient is estimated to be $(\beta) \approx 1.06 \times 10^{-11}$ cm/W. This results in a maximum

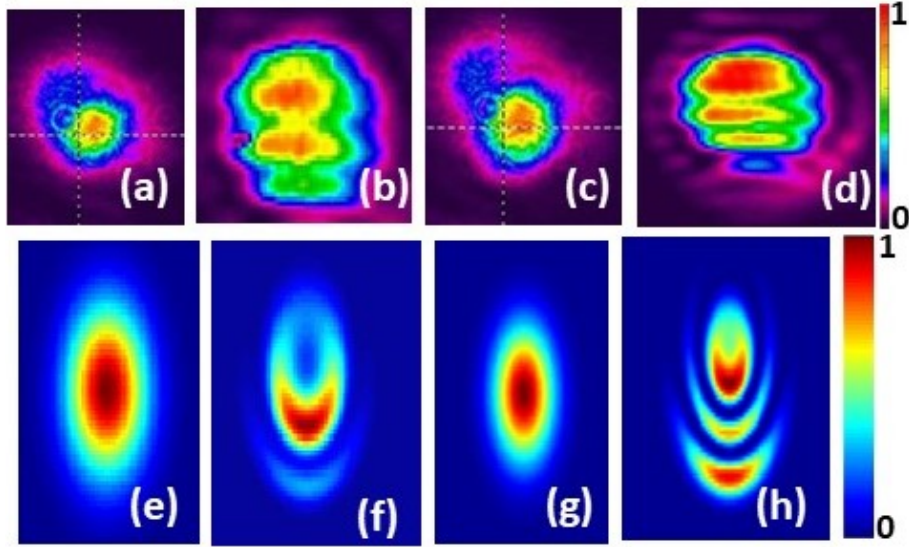


Figure 3.8: (a,b) Recorded (using thermal imaging camera) pump and idler beam-profile at the exit-face of crystal when $P_p = 3.5 \text{ W}$ ($w_0 \approx 60 \mu\text{m}$) (c,d) Corresponding beam-profiles of pump and idler respectively when $P_p = 4.2 \text{ W}$, (e,f) Simulated beam-profiles for pump and idler at the crystal exit-face when $P_p = 4 \text{ W}$, (g,h) Corresponding beam-profiles of pump and idler respectively when $P_p = 6 \text{ W}$.

nonlinear absorption $\beta I_p \approx 3 \times 10^{-7} \text{ cm}^{-1}$ which is extremely small in comparison with α_{cPPLT} . *Enomoto et.al.* have measured the nonlinear absorption for cPPLT without the grating has resulted in $\beta = 2.6 \times 10^{-9} \text{ cm/W}$ [34]. It is predicted that the suppression in β is mainly a consequence of periodic domain inversion in periodically poled crystals [35].

3.3.4 Spatial beam characteristics

It has been shown previously that the favorable conditions could result in self-guiding effect and optical bistability in SROs [36, 37]. In the present MgO:cPPLT-based SRO configuration, we have not observed self-guided effects. The early onset of saturation effects and distortion in idler beam at nominal power point towards absence of self-guided operation. We have recorded the the spatial beam profile of pump and idler ($\lambda_i=1812 \text{ nm}$) at different power levels using a thermal imaging camera (Spiricon, Ophir; USA). Two repre-

sentative recorded pump and idler beam profiles at (a) $P_p = 3.5$ W (b) $P_i = 0.57$ W, (c) $P_p = 4.2$ W and (d) $P_i = 0.54$ W are shown in the Figs. 3.8(a)-(d). From the Figs. 3.8(a) and (c) we could infer that both the pump beams maintain *near*-Gaussian (TEM_{00}) mode-profile. The small distortion in the pump beam is due to the un-optimized beam collection optics to capture the beam profile. On the other hand, the idler beam exhibits significant distortion as shown in Figs. 3.8(b) and (d) respectively. This distortion is essentially dictated by an asymmetric temperature gradient which is created by superposition of the temperature profiles made by the oven and the pump laser beam. By adopting the recipe proposed by O. A. Louchev *et al.* [27], we determined the pump and idler beam profiles at the crystal exit face which is shown in Figs.3.8(e-h) when $P_p = 3.8$ W (Figs. 3.8(e,f)) and $P_p = 4.5$ W (Figures 3.8(g,h)). Here, it is apparent in the Figs. 3.8(f) and (h) that the simulated idler beam profile undergoes discernible distortion for $P_p \geq 3.5$ W. For smaller P_p , we obtained *near*-Gaussian beam profile for the idler. The variation in idler beam-profile corroborates reasonably well with the experimentally measured counterparts in figure 3.8(b) & (d) barring the small difference in pump power values and impact of non-optimized optics used for recording the infrared (idler) beam. The difference in pump power values could be attributed to unaccounted parasitic losses and crystal inhomogeneity in the simulation.

3.4 Conclusion

We have reported a SRO based on 50 *mm*-long congruently-grown, periodically-poled $LiTaO_3$ crystal pumped by high power 532 nm fiber laser. This SRO exhibits early onset of saturation as well as idler beam distortion due to (a) high linear absorption at pump wavelength (b) low thermal conductivity (c) high thermo-optic coefficient (dn/dT) for MgO:cPPLT crystal which essentially results in the generation of strong thermal gradient [34, 38, 39]. The temperature gradient induced focusing leads to a focal length of

≈ 11 cm when $P_p \approx 4.5$ W and tends to be longer for smaller P_p [40]. It is worth pointing out that the linear absorption of $MgO : cPPLT$ in the signal wavelength band is about 6.5 times smaller which is also accompanied by a broader beam-waist at the crystal center. Therefore, in case of $MgO:cPPLT$ based SRO, the impact of signal absorption is appreciably small and has weak effect on SRO performance. The temperature induced phase-locking in $MgO:cPPLT$ based SRO is a promising possibility to explore [40]. A large thermo-optic coefficient in conjunction with high absorption in $MgO:cPPLT$ would significantly reduce the phase-locking threshold. Conventionally, the thermo-optic effects are less pronounced in case of ultrashort pulse pump lasers with low repetition rates (RRs). However, a high RR (≥ 100 MHz) of an ultrashort-pulse pump laser could result in discernible longitudinal (z) variation of phase-mismatch (Δk) by virtue of accumulated thermal effects. An optimum sweep in Δk (through suitable beam focusing) paves a plausible route to achieve broadly tunable, adiabatic ultrashort pulse frequency conversion with efficiencies $\geq 60\%$ in long-length crystals.

This Chapter constitutes the following journal publication:

- R. R. Sahoo, M. K. Shukla, and R. Das, “Thermo-optic effects in congruent- $LiTaO_3$ based continuous-wave optical parametric oscillator”, IEEE Photonics technol. lett., 33, 1069-1072 (2021)
- R. R. Sahoo, M. K. Shukla and R. Das, “Green laser pumped congruently-grown $LiNbO_3$ based singly-resonant optical parametric oscillator”, Results in Optics, 9, (2022).

References

- [1] D. A. Boas, T. Gaudette, G. Strangman, X. Cheng, J. J. Marota, and J. B. Mandeville, "The accuracy of near infrared spectroscopy and imaging during focal changes in cerebral hemodynamics," *Neuroimage*, vol. 13, no. 1, pp. 76–90, 2001.
- [2] H. W. Siesler, S. Kawata, H. M. Heise, and Y. Ozaki, *Near-infrared spectroscopy: principles, instruments, applications*. John Wiley & Sons, 2008.
- [3] L. M. Smith, J. Z. Sanders, R. J. Kaiser, P. Hughes, C. Dodd, C. R. Connell, C. Heiner, S. B. Kent, and L. E. Hood, "Fluorescence detection in automated dna sequence analysis," *Nature*, vol. 321, no. 6071, pp. 674–679, 1986.
- [4] R. C. Smith and K. S. Baker, "Optical properties of the clearest natural waters (200–800 nm)," *Applied optics*, vol. 20, no. 2, pp. 177–184, 1981.
- [5] G. L. Trainor, "Dna sequencing, automation, and the human genome," *Analytical chemistry*, vol. 62, no. 5, pp. 418–426, 1990.
- [6] S. Urabe, M. Watanabe, H. Imajo, and K. Hayasaka, "Laser cooling of trapped Ca^+ and measurement of the $3\ 2\ d\ 5/2$ state lifetime," *Optics letters*, vol. 17, no. 16, pp. 1140–1142, 1992.
- [7] W. Wang, M. Fejer, R. Hammond, M. Beasley, C. Ahn, M. Bortz, and T. Day, "Atomic absorption monitor for deposition process control of aluminum at 394 nm using frequency-doubled diode laser," *Applied physics letters*, vol. 68, no. 6, pp. 729–731, 1996.
- [8] W. Wang, R. Hammond, M. Fejer, C. Ahn, M. Beasley, M. Levenson, and M. Bortz, "Diode-laser-based atomic absorption monitor using frequency-modulation spec-

- troscopy for physical vapor deposition process control,” *Applied physics letters*, vol. 67, no. 10, pp. 1375–1377, 1995.
- [9] D. A. Walsh, P. G. Browne, M. H. Dunn, and C. F. Rae, “Intracavity parametric generation of nanosecond terahertz radiation using quasi-phase-matching,” *Optics express*, vol. 18, no. 13, pp. 13951–13963, 2010.
- [10] F. K. Tittel, D. Richter, and A. Fried, “Mid-infrared laser applications in spectroscopy,” in *Solid-state mid-infrared laser sources*, pp. 458–529, Springer, 2003.
- [11] Z. Shi, M. Tacke, A. Lambrecht, and H. Böttner, “Midinfrared lead salt multi-quantum-well diode lasers with 282 k operation,” *Applied physics letters*, vol. 66, no. 19, pp. 2537–2539, 1995.
- [12] H. Preier, “Recent advances in lead-chalcogenide diode lasers,” *Applied physics*, vol. 20, pp. 189–206, 1979.
- [13] P. Werle, “A review of recent advances in semiconductor laser based gas monitors,” *Spectrochimica Acta Part A: Molecular and Biomolecular Spectroscopy*, vol. 54, no. 2, pp. 197–236, 1998.
- [14] C. Gmachl, F. Capasso, D. L. Sivco, and A. Y. Cho, “Recent progress in quantum cascade lasers and applications,” *Reports on progress in physics*, vol. 64, no. 11, p. 1533, 2001.
- [15] C. Gmachl, A. Straub, R. Colombelli, F. Capasso, D. L. Sivco, A. M. Sergent, and A. Y. Cho, “Single-mode, tunable distributed-feedback and multiple-wavelength quantum cascade lasers,” *IEEE Journal of Quantum Electronics*, vol. 38, no. 6, pp. 569–581, 2002.

-
- [16] R. Köhler, C. Gmachl, A. Tredicucci, F. Capasso, D. L. Sivco, S. G. Chu, and A. Y. Cho, “Single-mode tunable, pulsed, and continuous wave quantum-cascade distributed feedback lasers at $\lambda \cong 4.6\text{--}4.7 \mu\text{m}$,” *Applied Physics Letters*, vol. 76, no. 9, pp. 1092–1094, 2000.
- [17] M. Ebrahim-Zadeh, “Continuous-wave optical parametric oscillators,” *Handbook of Optics*, vol. 4, pp. 1–33, 2010.
- [18] I. Shoji, T. Kondo, A. Kitamoto, M. Shirane, and R. Ito, “Absolute scale of second-order nonlinear-optical coefficients,” *JOSA B*, vol. 14, no. 9, pp. 2268–2294, 1997.
- [19] M. K. Shukla, P. S. Maji, and R. Das, “Yb-fiber laser pumped high-power, broadly tunable, single-frequency red source based on a singly resonant optical parametric oscillator,” *Optics Letters*, vol. 41, no. 13, pp. 3033–3036, 2016.
- [20] S. C. Kumar and M. Ebrahim-Zadeh, “Green-pumped continuous-wave parametric oscillator based on fanout-grating MgO: PPLN,” *Optics letters*, vol. 45, no. 23, pp. 6486–6489, 2020.
- [21] G. Samanta and M. Ebrahim-Zadeh, “Continuous-wave singly-resonant optical parametric oscillator with resonant wave coupling,” *Optics Express*, vol. 16, no. 10, pp. 6883–6888, 2008.
- [22] G. Samanta, S. C. Kumar, R. Das, and M. Ebrahim-Zadeh, “Continuous-wave optical parametric oscillator pumped by a fiber laser green source at 532 nm,” *Optics letters*, vol. 34, no. 15, pp. 2255–2257, 2009.
- [23] M. K. Shukla, S. Kumar, and R. Das, “Single-pass multi-watt second-harmonic-generation in congruent and stoichiometric lithium niobate,” *IEEE Photonics Technology Letters*, vol. 27, no. 13, pp. 1379–1382, 2015.

- [24] G. Boyd and D. Kleinman, "Parametric interaction of focused gaussian light beams," *Journal of Applied Physics*, vol. 39, no. 8, pp. 3597–3639, 1968.
- [25] R. Sowade, I. Breunig, J. Kiessling, and K. Buse, "Influence of the pump threshold on the single-frequency output power of singly resonant optical parametric oscillators," *Applied Physics B*, vol. 96, no. 1, pp. 25–28, 2009.
- [26] D. N. Nikogosyan, *Nonlinear optical crystals: a complete survey*. Springer Science & Business Media, 2006.
- [27] O. A. Louchev, N. E. Yu, S. Kurimura, and K. Kitamura, "Nanosecond pulsed laser energy and thermal field evolution during second harmonic generation in periodically poled $LiNbO_3$ crystals," *Journal of applied physics*, vol. 98, no. 11, p. 113103, 2005.
- [28] K. Moutzouris, G. Hloupis, I. Stavrakas, D. Triantis, and M.-H. Chou, "Temperature-dependent visible to near-infrared optical properties of 8 mol% Mg-doped lithium tantalate," *Optical Materials Express*, vol. 1, no. 3, pp. 458–465, 2011.
- [29] S. Chaitanya Kumar, K. Devi, G. Samanta, and M. Ebrahim-Zadeh, "Fiber-laser-based green-pumped continuous-wave singly-resonant optical parametric oscillator," *Laser Physics*, vol. 21, no. 4, pp. 782–789, 2011.
- [30] B. Bendow and D. Martin, "Towards ultralow thermal distortion glasses for ir and visible wavelengths," in *Advances in Optical Materials*, vol. 505, pp. 81–89, SPIE, 1984.
- [31] Y. Furukawa, K. Kitamura, A. Alexandrovski, R. Route, M. Fejer, and G. Foulon, "Green-induced infrared absorption in mgo doped linbo 3," *Applied Physics Letters*, vol. 78, no. 14, pp. 1970–1972, 2001.

-
- [32] A. L. Alexandrovski, G. Foulon, L. E. Myers, R. K. Route, and M. M. Fejer, "Uv and visible absorption in litao₃," in *Laser Material Crystal Growth and Nonlinear Materials and Devices*, vol. 3610, pp. 44–51, SPIE, 1999.
- [33] M. Sheik-Bahae, A. A. Said, T.-H. Wei, D. J. Hagan, and E. W. Van Stryland, "Sensitive measurement of optical nonlinearities using a single beam," *IEEE journal of quantum electronics*, vol. 26, no. 4, pp. 760–769, 1990.
- [34] S. Enomoto and S. Ashihara, "Comparative study on light-induced absorption between mgo: Linbo₃ and mgo: Litao₃," *Journal of Applied Physics*, vol. 110, no. 6, p. 063111, 2011.
- [35] Y. Chen, S. Liu, D. Wang, T. Chen, and M. Xiao, "Measurement of laser-induced refractive index change of inverted ferroelectric domain linbo₃," *Applied optics*, vol. 46, no. 31, pp. 7693–7696, 2007.
- [36] S. Lin, Y. Lin, Y. Huang, A. Chiang, and J. Shy, "Observation of thermal-induced optical guiding and bistability in a mid-ir continuous-wave, singly resonant optical parametric oscillator," *Optics letters*, vol. 33, no. 20, pp. 2338–2340, 2008.
- [37] I.-H. Bae, H.-S. Moon, S.-K. Kim, S.-N. Park, and D.-H. Lee, "Self-guided operation of singly resonant continuous-wave optical parametric oscillator based on bulk MgO-doped PPLN," *Applied Physics B*, vol. 106, no. 4, pp. 797–801, 2012.
- [38] S. Ashihara and S. Enomoto, "Pulsed-light-induced absorption in linbo₃ and litao₃ crystals with mgo doping," in *European Quantum Electronics Conference*, p. EF_P13, Optica Publishing Group, 2011.
- [39] L. Moretti, M. Iodice, F. G. Della Corte, and I. Rendina, "Temperature dependence of

the thermo-optic coefficient of lithium niobate, from 300 to 515 k in the visible and infrared regions,” 2005.

- [40] M. Vainio, J. Peltola, S. Persijn, F. Harren, and L. Halonen, “Thermal effects in singly resonant continuous-wave optical parametric oscillators,” *Applied Physics B*, vol. 94, no. 3, pp. 411–427, 2009.

Chapter 4

Stimulated polariton scattering in $LiNbO_3$ based singly-resonant optical parametric oscillator

4.1 Motivation

Lithium Niobate ($LiNbO_3$) is one of the most widely-used ferroelectric crystal for nonlinear frequency conversion processes due to a high value of second-order nonlinear optical susceptibility ($\chi_{33}^{(2)}$) [1, 2, 3, 4, 5]. The engineered electric-field induced poling in $LiNbO_3$ crystals facilitate in accessing the largest nonlinear coefficient ($\chi_{33}^{(2)}$) in a variety of frequency conversion processes [6, 7]. On the other hand, $LiNbO_3$ crystal possesses a wide transparent window ranging from 330 – 5500 nm. This property improves the applicability of $LiNbO_3$ -based tunable optical sources over a wide spectral band. From a spectroscopic viewpoint, $LiNbO_3$ posses active transverse-optic (TO) phonon mode branches, thereby displaying both Raman-activity as well as infrared-activity [8, 9, 10]. The interaction of transverse optical (TO) lattice vibrations with an electromagnetic (EM) wave modifies the nonlinear optical susceptibility such as ($\chi^{(2)}$ and $\chi^{(3)}$). This scattering process facilitates the generation of *polariton* modes having a predominant EM character [11, 12]. In general, the polariton mode frequency is situated in the far-infrared (FIR) or terahertz (THz) frequency band. This polariton induced scattering results in a frequency-shifted Stokes beam [13, 14]. When the Stokes beam generates through a concomitant stimulated process, it is known as stimulated-polariton-scattering (SPS). It is worth pointing out that the gain co-

efficient of Stokes mode (or the polariton mode) is primarily dictated by the electronic as well as ionic (Raman) contribution to $\chi^{(2)}$ [15]. A significant attenuation is observed by the polariton beam, by virtue of a dominant imaginary component of dielectric constant for $LiNbO_3$ at low (FIR) frequencies. It is important to note that phase matching constraint is an important criteria for the SPS process. Consequently, this adds to the system complexity for realizing an efficient SPS process, particularly in a cavity configuration. SPS in $LiNbO_3$ (LN) and $KTiPO_4$ (KTP) have been widely investigated using pulsed pump sources [16]. A $LiNbO_3$ -based polariton laser has been demonstrated by Warrier *et al.* which generates frequency tunable ultrashort pulses in the terahertz (THz) spectral band through a forward propagating SPS process [17]. On the other hand, Jang *et al.* demonstrated a tunable laser source using a backscattered polariton mode in a KTP crystal [18]. In general, a backscattered polariton mode exhibits a large imaginary component of the propagation constant and consequently, it undergoes strong attenuation in the propagation direction. Therefore, the lasers based on backscattered polariton mode have extremely high threshold [19]. Using $KiTiOAsO_4$ (KTA) crystal, a polariton laser with a wavelength tunability from 1078 – 1087 nm, have been demonstrated by Zang *et al.* [20]. In a few configurations, the polariton modes were excited in a $LiNbO_3$ based doubly-resonant optical parametric oscillator (OPO) around the degeneracy with an aim to generate tunable radiation [21, 22]. Although, the pump threshold tends to reduce in a doubly-resonant cavity, the far-infrared (FIR) output is quite unstable [23, 24]. In $LiNbO_3$ -based singly-resonant OPO (SRO), L. Liu *et al.* have observed multiple frequency shifted signal beam at higher pump powers with 47 cm^{-1} , 94 cm^{-1} and 104 cm^{-1} shifts. Such shifts have been attributed to stimulated Raman scattering (SRS) [25, 26]. However, it is crucial to note that the smallest TO phonon mode for $LiNbO_3$ is situated at $\approx 248\text{ cm}^{-1}$ which belongs to vibrations possessing conventional A_1 symmetry. Therefore, the small frequency-shifted peaks in the SRO signal are essentially excited by virtue of polariton-mode scattering that

could be practically termed as SPS Stokes modes [22]. In presence of a strong pump, A. J. Lee *et al.* observed a cascaded SPS process in Mg doped $LiNbO_3$ when the fundamental and the Stokes beams were resonated in separate cavities [27, 28]. This led to a broad spectral tunability in the THz band spanning from 1.3 THz to 2.6 THz [29]. The aforementioned explorations indicate that a SPS process in conjunction with a $LiNbO_3$ -based SRO configuration could provide an extremely wide tunable spectrum ranging from mid-infrared (MIR) to FIR (or THz) band [30, 31]. In addition, if the advantage brought about by an SPS process could be integrated within a single SRO cavity, then the complexity towards generating tunable FIR radiation would significantly simplify. In this chapter, we will demonstrate a continuous-wave (cw)-SRO based on an 80-mm long MgO-doped periodically-poled $LiNbO_3$ (MgO:PPLN) crystal. The SRO is a four mirror ring cavity generating (resonant) signal beam near communication band ($1.5 \mu m$) and single-pass idler whose frequency is tunable in the MIR band ($3.5 - 3.8 \mu m$). At nominal pump powers, resonant signal exhibits multiple side-peaks which are attributed to SPS process in MgO:PPLN crystal. A comprehensive study has been carried out to understand these discretely spaced polariton modes on the basis of the dispersion property of $LiNbO_3$ crystal.

4.2 Experimental Configuration

The schematic for the experimental set-up is shown in Fig.4.1 which comprises a fiber laser pump delivering $\approx 40 W$ of linearly-polarized, single-frequency output at $1064 nm$ wavelength and $M^2 \leq 1.1$. A half wave plate (HWP), in conjunction with a polarizing beam splitter (PBS) is used for controlling the incident pump power (P_p). The second HWP is used to obtain a suitable pump polarisation for carrying out phase-matching in MgO:PPLN crystal. Two lenses L_1 ($f = -75mm$) and L_2 ($f = +100mm$) are employed for obtaining optimum beam-waist at the center of MgO:PPLN crystal. In accordance with

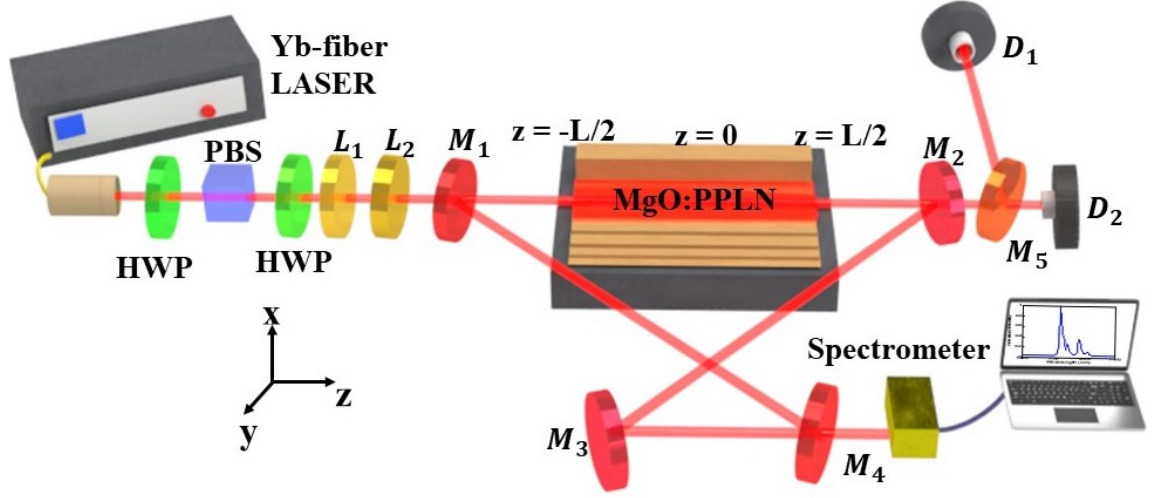


Figure 4.1: A schematic of the experimental set-up for the SRO; HWP: Half-wave plate, PBS: Polarizing beam-splitter, l_1 : Concave lens, l_2 : Convex lens, $M_{1,2}$: Plano-concave mirrors, $M_{3,4}$: Plane mirrors, OV: Temperature controlled oven housing the nonlinear crystal $\text{MgO} : \text{PPLN}$, M_5 : Dichroic Mirror, $D_{1,2}$: Thermal photodetectors

the Boyd-Kleinman (BK) theory for maximizing the frequency conversion efficiency, the pump beam is focused to a spot-size of radius $w_{op} \approx 75 \mu\text{m}$ which results in a focusing parameter $\xi \approx 1.5$ [32]. This is about half of the optimum value of $\xi_{op} \approx 2.84$ which allows us reduce the thermal load on the $\text{MgO}:\text{PPLN}$ crystal [32]. The SRO is comprised of a four-mirror ring-cavity with two curved mirrors having radius of curvature ($ROC = -200\text{mm}$) and two plane mirrors. The cavity design ensures a cavity length of $\approx 100\text{ cm}$. The cavity mirrors are highly reflecting ($R \geq 99\%$) in the $1350 - 1650\text{ nm}$ wavelength range and highly transmitting ($T \geq 85\%$) for the pump (1064 nm) as well as idler ($2500 - 4500\text{ nm}$) wavelength range. The SRO nonlinear crystal is an 80 mm long and 1 mm thick multi-grating $\text{MgO}:\text{PPLN}$ crystal with grating periods varying from $\Lambda = 27.5\ \mu\text{m}$ to $\Lambda = 30\ \mu\text{m}$ so as to facilitate *type-0* phase-matching. The entry as well as exit surface of $\text{MgO}:\text{PPLN}$ crystal is anti-reflection (AR) coated for pump, signal and idler wavelengths. The crystal is housed in an oven whose temperature (T_{ov}) could be varied from room temperature to 200°C so as carry out coarse wavelength tuning of the signal and idler modes.

4.3 Results and Discussion

4.3.1 SRO: Wavelength Tunability and Conversion Efficiency

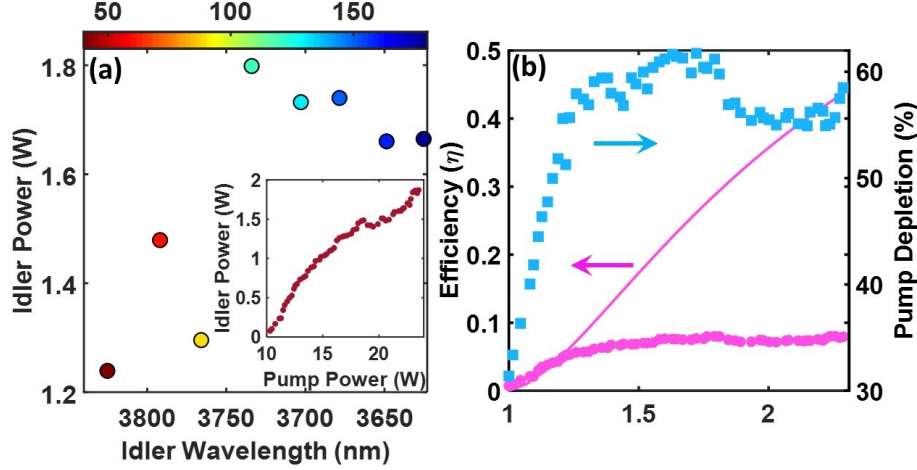


Figure 4.2: (a) Variation of SRO idler wavelength and idler power as a function of crystal oven temperature (T_{ov}) for $\Lambda_{QPM} = 29.5\mu m$ SRO (represented by the top color bar) Inset: Variation of idler power as a function of pump power when $T_{ov} = 100^\circ C$. (b) Measured conversion efficiency (magenta dots) and depleted pump power (blue dots) when $T_{ov} = 100^\circ C$ and $\Lambda_{QPM} = 29.5 \mu m$ as a function of $\frac{P_p}{P_{p(Th)}}$. The solid magenta curve represents the expected theoretical variation.

The SRO generates wavelength in MIR spectral band and exhibits a threshold pump power P_{Th} of $\approx 9.5 W$ at oven temperature $T_{ov} = 100^\circ C$. For an efficient MIR generation, we have used a periodically poled $LiNbO_3$ crystal with grating period $\Lambda = 29.5\mu m$. By changing the T_{ov} , the SRO idler wavelength (λ_i) could be coarsely tuned from 3625 – 3825 nm. The idler beam was separated from the pump beam by the dichroic mirror M_5 . We have observed that, in the wavelength tuning range, the threshold for oscillation varies between 8 – 10 W. The signal wavelength (λ_s) could be tuned from (1470 – 1510 nm) by changing the crystal oven temperature. We have represented the variation of idler power (P_i) with λ_i in figure 4.2(a). The colour map represents the temperature scale associated with the oven. The drop in P_i at smaller T_{ov} could be due to the higher absorption by MgO:PPLN crystal at longer IR wavelengths ($\geq 3700 nm$).

4.3.2 Power Scaling

In order to get a deeper insight of the SRO operation, we have observed the variation in P_i as a function of pump power (P_p) at $T_{ov} = 100^\circ C$ which could be observed in Fig. 4.2(a) inset. From this study, we have observed a linear variation of P_i as a function of P_p up to $\approx 13 W$ which is followed by the saturation behaviour. A maximum of $\approx 1.9 W$ idler power could be obtained from the present SRO configuration for a maximum pump power of $P_p \approx 24 W$. This corresponds to a conversion efficiency of $\approx 8.4\%$. It is also worthwhile to note that the maximum pump depletion of 62% was observed at $P_p \approx 17 W$ which reduced to $\approx 55\%$ at $P_p \approx 24 W$. Assuming a Gaussian pump beam, the internal SRO conversion efficiency at the exit face ($z = +\frac{L}{2}$ in Fig. 1) of the MgO:PPLN crystal could be theoretically estimated from

$$\eta = \frac{P_i(z = \frac{L}{2})}{P_p(z = -\frac{L}{2})} = 1 - \left[\frac{1}{N} + \int_0^{\ln(N)} e^{-x} \cos^2 \Gamma(x) dx \right] \quad (4.1)$$

where Γ could be estimated from the dispersion relation $\cos^2(\Gamma) = 1 - \frac{\Gamma^2 e^x}{N}$, $N = \frac{P_p}{P_{Th}}$ and $z = \pm \frac{L}{2}$ refers to MgO:PPLN end-faces [33]. This model predicts the pump depletion to be $\approx 71\%$ when $P_p \approx 6.5P_{Th}$. However, we have observed the onset of saturation in the pump depletion starts when $P_p \approx 1.7P_{Th}$. A small SRO frequency conversion efficiency in conjunction with high pump depletion ($\geq 55\%$) as well as an early onset of saturation drew our attention to the high intra-cavity (resonant) signal power (P_s) and its manifestations. Previously investigations have shown that in the presence of high intra-cavity signal power (P_s) introduce enhanced absorption in the nonlinear crystal and could be manifested in the form of thermal dephasing as well as thermal lensing. This could result in a self guided process, which in turn modifies the beam quality [34]. In addition, the cascaded $\chi^{(2)}$ - $\chi^{(2)}$ processes have also been reported [35]. The high intra-cavity power could also be employed to carry out the SHG of signal beam. This in turn enhance the spectral coverage of an SRO [36]. Additionally these high intra-cavity P_s could interact with the vibrational

levels of the $LiNbO_3$ crystal giving rise to the possibility of simultaneously exciting Raman-active as well as IR-active TO phonon modes. As a result, frequency-shifted modes could be generated which are termed as *Stokes beam*. When the difference between the Stokes wavelength (λ_{st}) and λ_s are small, they could satisfy the resonant condition for the SRO. If the gain cross-section for λ_{st} overcomes the cavity loss, it starts to oscillate. Previously, such resonant frequency shifted Stokes beam have been attributed to stimulated Raman scattering (SRS) [22].

The phenomenon discussed above are attributed to the high power P_s . This high power intra-cavity signal beam could coherently interact with IR-active TO phonon modes which have predominant *photon-like* character. This phenomenon could generate polariton modes. In general, these modes typically situated in the low energy FIR (or THz) spectral band. Such polariton modes could be generated through a stimulated process when the SRO signal as well as the Stokes beam are nearly collinear and consequently, this process is termed as *stimulated* polariton scattering (SPS). The phase matching condition associated with this SPS process is given by the relation;

$$\vec{k}_s = \vec{k}_{st} + \vec{k}_{FIR} \quad (4.2)$$

where \vec{k}_{FIR} , \vec{k}_{st} and \vec{k}_s are the wavevectors corresponding to polariton mode, SRO signal mode and the Stokes mode respectively. The PM condition is schematically represented in Fig. 4.3 where it could be observed that the signal and Stokes beams have a small angular separation ($\leq 5^\circ$) and the FIR beam generated through the SPS process propagates in *nearly* orthogonal direction with respect to the oscillating SRO signal.

4.3.3 Stimulated Polariton Scattering

The high intra-cavity signal power oscillating inside the SRO could initiate the SPS process explained in the previous section. In order to get an experimental observation,

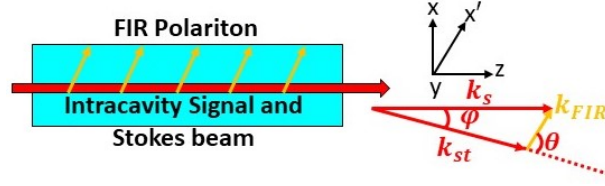


Figure 4.3: A schematic to represent the phase-matching between SRO signal beam and SPS Stokes beam and polariton (FIR) mode. x' -axis makes an angle ϕ with x -axis fixed to the MgO:PPLN crystal.

we have measured the spectrum of intra-cavity signal beam leaking out of the cavity with a mid-infrared (MIR) spectrometer containing InGaAs photodiode array (BWTEK Inc., USA). The recorded spectrum at a pump power of $P_p = 20 \text{ W}$ is presented in figure 4.4. Figures 4.4(a and b) represent the spectrum at different crystal oven temperatures T_{ov} for $\Lambda_{QPM} = 29.5 \mu\text{m}$. The signal spectrum in figure 4.5(a) and (b) corresponds to a grating period $\Lambda_{QPM} = 30 \mu\text{m}$. In order to get a clear picture with reference to the Raman Stokes shift, we consider the signal wavelengths to be the excitation wavelengths. With reference to the signal wavelengths, we have plotted the Raman shifts associated with the polarization parallel to the optic-axis (c -axis) [37].

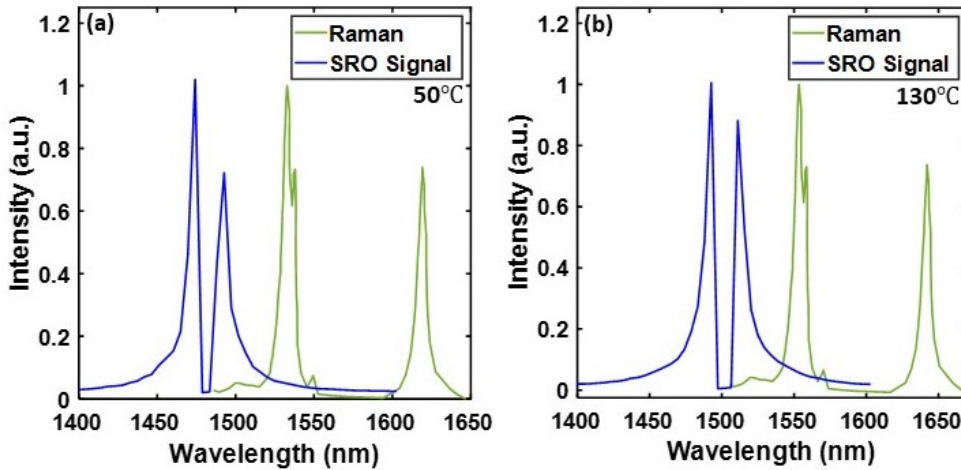


Figure 4.4: Measured SRO signal spectrum (solid blue curve) of the SRO and the expected Raman spectrum (solid green curve) for MgO:PPLN when (a) $\Lambda_{QPM} = 29.5 \mu\text{m}$ and $T_{ov} = 50^\circ\text{C}$ (b) $\Lambda_{QPM} = 29.5 \mu\text{m}$ and $T_{ov} = 130^\circ\text{C}$ (c) $\Lambda_{QPM} = 30 \mu\text{m}$ and $T_{ov} = 52^\circ\text{C}$ (d) $\Lambda_{QPM} = 30 \mu\text{m}$ and $T_{ov} = 127^\circ\text{C}$.

In the observation, we have observed side peaks in the signal spectrum of the SRO. Interestingly, it could be distinctly observed from figure 4.4(a),(b) and 4.5(a),(b) that these side peaks do not coincide with the expected Raman spectrum (green solid curves). In these plots, we could observe that the nearest side-peaks have a smaller wavelength shift as compared to the first Raman Stokes mode ($\approx 248 \text{ cm}^{-1}$). Also, the wavelength separation between the SRO signal mode and the first side-peak is smaller in case of a shorter grating period *i.e.* for $\Lambda_{QPM} = 29.5 \text{ }\mu\text{m}$. In view of the above observation, we could term the side-peaks as Stokes mode(s). These mode(s) could be explained through the phase matched interaction presented in equation 4.2. In addition we have studied the SRO signal spectrum for $\Lambda_{QPM} = 30 \text{ }\mu\text{m}$. The spectrum, in this case, exhibits multiple Stokes modes the second side-peak nearly coincides with the expected Stokes mode for the Raman scattering process (see Fig. 4.5(a) and (b)). It is apparent from the figures that these wavelength shifts undergone by this side-peak remain unchanged as the crystal oven temperature (T_{ov}) changes. Therefore, we conclude that the second side-peak in signal spectrum (for $\Lambda_{QPM} = 30^\circ\text{C}$) is the SRS Stokes mode. Consequently, the other Stokes modes (side-peaks) are essentially due to the stimulated polariton scattering (SPS) process which discussed in detail later. During the coarse wavelength tuning of the SRO (by varying T_{ov} from 30°C to 200°C), it was observed that the wavelength shift in Stokes mode due to the SPS process change. In fact, all the Stokes mode disappeared for $T_{ov} \geq 140^\circ\text{C}$ (when $\Lambda_{QPM} = 30 \text{ }\mu\text{m}$) which essentially implies that the SPS Stokes modes (at high T_{ov}) suffer very high cavity losses. On the other hand, the SPS Stokes mode were observed up to $T_{ov} \approx 180^\circ\text{C}$ for $\Lambda_{QPM} = 29.5 \text{ }\mu\text{m}$ grating period. The threshold of pump power required for the generation of the Stokes mode is $\approx 1.25P_{th}$. From the power scaling observation, we could see that the P_p up to this threshold power increases monotonically. In addition, it could be observed that the theoretical curve (solid magenta line) in Fig. 4.2(a) begins to deviate from the experimental measurements (magenta dots) around $\frac{P}{P_{th}} \approx 1.25$. This

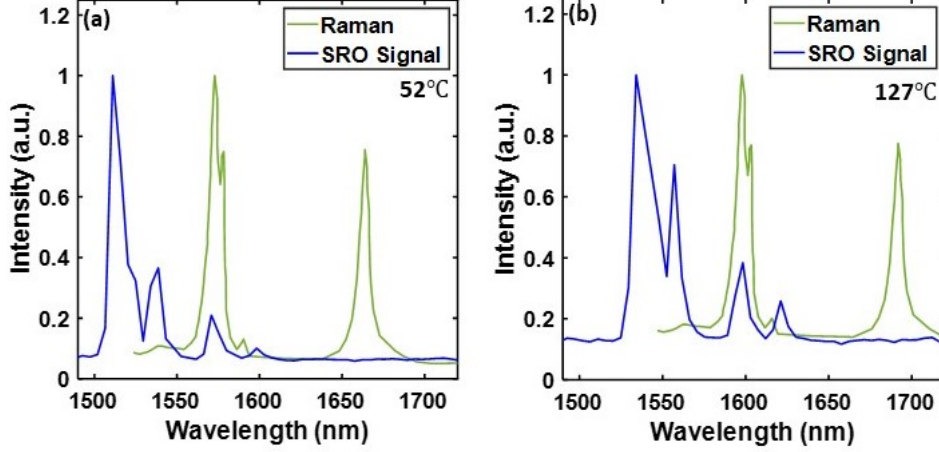


Figure 4.5: Measured SRO signal spectrum (solid blue curve) of the SRO and the expected Raman spectrum (solid green curve) for MgO:PPLN for $\Lambda_{QPM} = 29.5 \mu m$ SRO (a) $T_{ov} = 50^\circ C$ (b) $T_{ov} = 130^\circ C$

is due to the change in the slope of the idler power as a function of pump power. All the above mentioned observations indicate that the drop in conversion efficiency takes place simultaneously with the beginning of the SPS process. In order to appreciate the underlying mechanism, it is worth noting that the generation of Stokes beam (through the SPS process) draws significant optical power from the SRO signal beam. Since, the parametric (idler) generation process in the SRO directly depends on the intra-cavity signal power, the measured conversion efficiency tends to reduce as early as SPS process sets in. An increase in pump power henceforth, facilitates further growth of SPS Stokes mode(s) at the expense of a slower growth of idler beam.

4.3.4 Polariton mode dispersion and gain

In order to explain the above observations, we investigate the transverse optical (TO) phonon dispersion curve for MgO-doped $LiNbO_3$ which is shown in figure 4.6 and 4.7.

The TO phonon dispersion has been obtained using the relation [8],

$$k^2 = \frac{\omega^2 \epsilon_{FIR}(\omega)}{c^2} = \frac{\omega^2}{c^2} \left(\epsilon_\infty + \sum_j \frac{S_j \nu_{oj}^2}{\nu_{oj}^2 - \nu^2 - i\nu\Gamma_j} \right) \quad (4.3)$$

where k and ω are wavevector and frequency associated with the phonon dispersion of MgO-doped $LiNbO_3$ respectively, ϵ_∞ is the contribution of high-frequency lattice vibrations to the dielectric polarization and takes a constant value of 4.6 for MgO-doped $LiNbO_3$ [38]. ν_{oj} , S_j and Γ_j represents the characteristic TO vibrations associated with A_1 symmetry (electric field $\vec{E} \parallel c$ -axis of $LiNbO_3$), oscillator strength and linewidth respectively for MgO-doped $LiNbO_3$ crystal [8, 38]. An interaction between the SRO signal mode with TO phonons of $LiNbO_3$ gives rise to Stokes modes. In other words, a high-power intra-cavity SRO signal beam could facilitate the generation of nonlinear polarisation at a Stokes wavelength (close to the SRO signal) and at a FIR wavelength (at the phonon mode energy). For a perfectly *phase-matched* ($\vec{k}_s = \vec{k}_{st} + \vec{k}_{FIR}$) interaction, the propagation constant ($k_{FIR} \equiv k(\omega_{FIR})$) associated with the generated FIR mode is given by

$$k(\omega_{FIR}) = \pm \sqrt{(k_s - k_{st})^2 + 4k_s k_{st} \sin^2 \frac{\phi}{2}} \quad (4.4)$$

where k_s and k_{st} are the propagation constants for the intra-cavity SRO signal and the polariton Stokes beam respectively, ϕ represents the small angle between the signal and the generated Stokes beam (see Fig. 4.3). Here we have represented equation 4.4 graphically for $\phi = 1.7^\circ$ (color) and $\phi = 1.5^\circ$. We could observe that the phase-matching curves intersects the TO phonon dispersion curve (light blue curve) for $LiNbO_3$ in different branches. A *phase-matched* pair of Stokes beam and the FIR polariton beam is being generated at the point of intersection. It is important to note that if the magnitude of k_{FIR} (at the point of intersection) in Fig. 4.5(a)) is significantly smaller than that at the Brillouin zone boundary then the generated mode would exhibit a dominant em character. In case, k_{FIR} is large (*i.e.* close to the value at Brillouin zone boundary), the generated FIR (polariton) mode

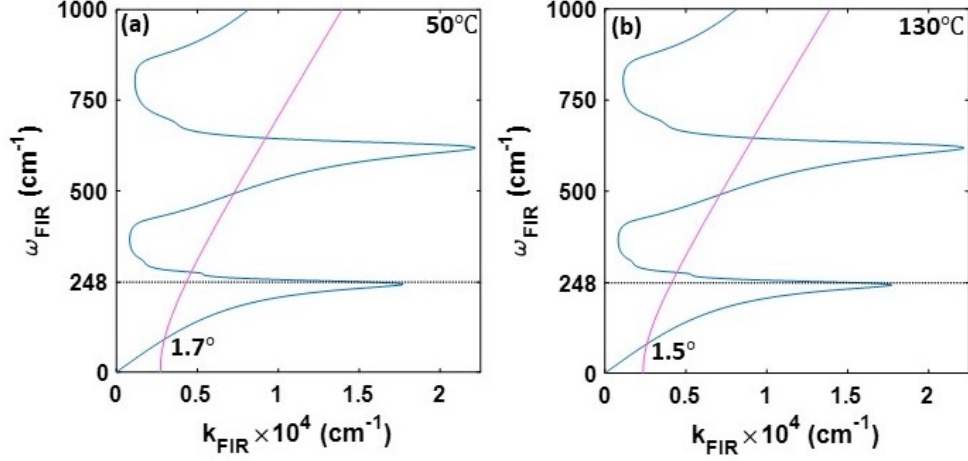


Figure 4.6: Represents the dispersion relation for TO phonon modes (solid blue curve) for MgO-doped $LiNbO_3$ crystal (equation 4.3) and the variation of polariton frequency ω_{FIR} (solid purple curve) for different ϕ as a function of wavevector (k_{FIR}) (see 4.4) for $\Lambda_{QPM} = 29.5 \mu m$ at (a) $T_{ov} = 50^\circ C$ and (b) $T_{ov} = 130^\circ C$.

exhibits a dominant vibrational (phonon-like) character which is the widely-known Raman mode. For intermediate values of k_{FIR} , the FIR mode could exhibit an hybrid electro-mechanical character or alternately, a polariton mode. This process of FIR generation is achieved through *stimulated polariton scattering* (SPS) and could efficiently generate coherent terahertz (THz) wave.

In Figure 4.6(a), the k_{FIR} *phase-matching* curve intersects the TO-mode dispersion of $LiNbO_3$ at $\omega_{FIR} \approx 86 \text{ cm}^{-1}$ which corresponds to the SPS Stokes mode at $\lambda_{st} \approx 1493 \text{ nm}$ shown in Fig.4.4(a). It is worth pointing out that, in this case, the SRO signal and the SPS Stokes are resonant to the same SRO cavity. Hence, we could infer that the signal or idler wavelength change as a consequence of temperature tuning would allow intersection of curves for a different value of ϕ . For example, we have measured the signal spectrum at $T_{ov} = 130^\circ C$ in Fig. 4.4(b) (solid green curve) which depicts a $\lambda_{st} \approx 1511 \text{ nm}$ when $\lambda_s \approx 1493 \text{ nm}$. The origin of this side-peak could be understood if we plot the curve for k_{FIR} (as per equation 4.4) when $\phi = 1.5^\circ$ as shown in figure 4.6(b). This curve intersects

the $LiNbO_3$ phonon dispersion curve at $\omega_{FIR} \approx 79.8 \text{ cm}^{-1}$ ($\equiv 18 \text{ nm}$) which is equivalent to a SPS Stokes wavelength of $\approx 1511 \text{ nm}$.

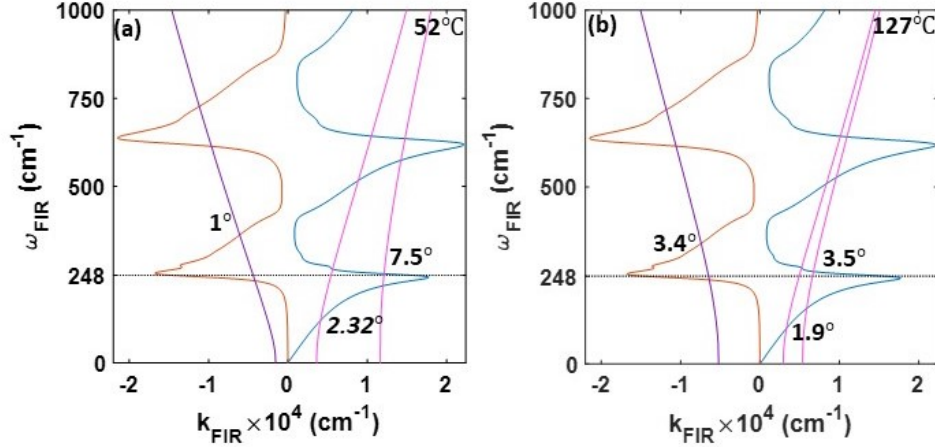


Figure 4.7: Represents the dispersion relation for TO phonon modes (solid blue curve) for MgO-doped $LiNbO_3$ crystal ((4.3)) and the variation of polariton frequency ω_{FIR} (solid purple curve) for different ϕ as a function of wavevector (k_{FIR}) (see (4.4)) for $\Lambda_{QPM} = 30 \mu m$. Variation in $Re(k_{FIR})$ represented by solid blue curve and solid brown curve represents $Im(k_{FIR})$. The solid purple curves represent the variation in k_{FIR} (as per (4.4)) for different ϕ ($\Lambda_{QPM} = 30 \mu m$) (a) $T_{ov} = 52^\circ C$ and (b) $T_{ov} = 127^\circ C$.

On the other hand for $\Lambda = 30 \mu m$, the signal spectrum exhibits multiple side peaks (at $T_{ov} = 52^\circ C$) and one of the peaks coincide with the Raman Stokes peak (see figure 4.5(a)). This stimulated Raman scattering (SRS) Stokes peak propagates at an angle $\phi \approx 7.5^\circ$ (see solid magenta curve in Fig. 4.7(a)) with respect to the signal beam and therefore, it undergoes significant cavity losses. Consequently, the SRS peak is small as compared to the SPS peak at $\lambda_{st} \approx 1534 \text{ nm}$ (for $k_{FIR} > 0$) which propagates at an angle $\phi = 2.3^\circ$ with respect to the SRO signal beam (see solid magenta curve in figure 4.7(a)). A similar observation could be made with regard to figure 4.5(b) which also contains three distinct peaks in the SRO signal spectrum. As explained above, the origin of first SPS Stokes mode and the SRS mode could be traced to the intersection of k_{FIR} curve (for $k_{FIR} > 0$) with the TO phonon dispersion curve for $LiNbO_3$ in Fig. 4.7(b) (solid magenta curves) when

$\phi = 1.9^\circ$ (SPS mode) and $\phi = 3.5^\circ$ (SRS mode).

In order to understand the origin of the third side-peak in the SRO signal spectrum (Figs. 4.7(a) and (b)), we note that k_{FIR} could be negative as per equation 4.3. When $k_{FIR} < 0$ graph (solid purple curve in Fig. 4.7(a) or (b)) intersects the TO phonon dispersion curve (solid brown curve), an SPS or SRS mode could be generated. The phase-matching condition for such a process would be $\vec{k}_s + \vec{k}_{st} + \vec{k}_{FIR} = 0$ which essentially implies that the SRO signal and Stokes beams are counter-propagating. The curve representing k_{FIR} (solid purple colour) for $\phi = 1^\circ$ (when $T_{ov} = 52^\circ C$) and $\phi = 3.4^\circ$ (when $T_{ov} = 127^\circ C$) is shown in Figs. 4.5(c) and (d) respectively. The intersection with the TO phonon dispersion curve (solid brown) yields the third side-peak at $\lambda_{st} \approx 1598 \text{ nm}$ ($\omega_{FIR} = 363 \text{ cm}^{-1}$) in Fig. 4.5(a) and $\lambda_{st} = 1621 \text{ nm}$ ($\omega_{FIR} = 349 \text{ cm}^{-1}$) in Fig. 4.5(b). In order to ascertain the gain associated with the Stokes beam and the FIR beam for a phase-matched interaction process, we note that [15],

$$\frac{\partial I_{st}(z, x')}{\partial z} = -\alpha_{st} I_{st}(z, x') + g_{st}^{(2)} [I_s(z, x') I_{st}(z, x') I_{FIR}(z, x')]^{1/2} + g_{st}^{(3)} I_s(z, x') I_{st}(z, x') \quad (4.5)$$

$$\frac{\partial I_{FIR}(z, x')}{\partial x'} = -\alpha_{FIR} I_{FIR}(z, x') + g_{FIR}^{(2)} [I_s(z, x') I_{st}(z, x') I_{FIR}(z, x')]^{1/2} \quad (4.6)$$

where the axis x' is defined in Fig. 4.3. We define

$$\alpha_{FIR} = \frac{\omega_{FIR}^2}{k_{FIR}^2} \text{Im}(\epsilon_{FIR}) \quad (4.7)$$

along with

$$g_m^{(2)} = \frac{\omega_m}{c} \left(\frac{2}{n_s n_{st} n_{FIR}} \right)^{1/2} \left(\frac{\mu_o}{\epsilon_o} \right)^{1/4} \left[d_E + \sum_j d_{Qj} \text{Re}(\chi_{Qj}) \right] \quad (4.8)$$

with ($m \equiv st, FIR$) and

$$g_m^{(3)} = \frac{\omega_m}{c} \left(\frac{\mu_o}{\epsilon_o} \right)^{1/2} \left[d_E + \sum_j d_{Qj}^2 \text{Im}(\chi_{Qj}) \right] \quad (m \equiv st) \quad (4.9)$$

4 Stimulated polariton scattering in $LiNbO_3$ based singly-resonant optical parametric oscillator

where $d_E' = 16\pi d_{33}$ and $d_{33} = \frac{1}{2}\chi^{(2)}$ is the nonlinear coefficient of $MgO : LiNbO_3$.

Here, $\chi_{Qj} = \epsilon_{FIR} - \epsilon_\infty$ and

$$d_{Qj} = \left[\frac{8\pi c^4 n_s (S_{33}/L\Delta\Omega)_j}{S_j \bar{h} \nu_{\circ j} \omega_{st}^4 n_{st} (\bar{n}_0 + 1)} \right]^{1/2} \quad (4.10)$$

where, n_s and n_{st} are the refractive indices of MgO:PPLN at SRO signal and SPS (or SRS) Stokes frequency respectively, \bar{h} is the Plank constant, \bar{n}_0 is the Bose distribution function, $(S_{33}/L\Delta\Omega)_j$ is the spontaneous Stokes scattering efficiency associated with the TO vibrational mode and j runs over all the natural phonon modes [15]. The factors $g_{st}^{(2)}$ and $g_{st}^{(3)}$ (in Eq. (4.5)) and $g_{FIR}^{(2)}$ (in Eq. (4.6)) represent the gain for the Stokes beam and the FIR beam. Amongst other factors, the parametric gain factors $g_{st}^{(2)}$ and $g_{FIR}^{(2)}$ are essentially dependent on the electronic polarization (d_E) as well as ionic polarization (d_{Qj}). From Eq. 4.9, it could be inferred that this interaction could be mediated by the third-order nonlinear polarization *i.e.* $d_{Qj}^2 Im(\chi_{Qj})$. In Figs. 4.5(a) and (b), the third side-peaks (weak intensity) are essentially due to such an interaction where the polariton mode derives energy from a decaying phonon mode through $Im(\chi_{Qj})$ and consequently, this Stokes mode is strongly attenuated within the cavity.

In Fig. 4.8, we present a variation in SPS Stokes wavelength as a function of MgO:PPLN crystal oven temperature (T_{ov}) for $\Lambda = 29.5 \mu m$ (purple square). For reference, we have also plotted the variation in SRO signal wavelength (red squares) and the expected 248 cm^{-1} Raman Stokes wavelength (green open circles) across the temperature range over which T_{ov} varies. The solid brown curve depict the expected variation of phase-matched SRO signal wavelength [39]. It is apparent that the difference between the SRO signal and the Stokes shift due to SPS (λ_{st}) varies non-uniformly across the entire tuning range. This is primarily due to the fact that the SRO cavity selects an angle ϕ for which the Stokes mode suffers least loss and therefore, exhibits most stable oscillations. The selection of angle ϕ is mainly dictated by the shape of wavefront for the polariton Stokes mode and the round-trip

scattering as well as reflection loss.

A similar variation could be observed in the variation of SPS Stokes and SRS Stokes modes for $\Lambda = 30 \mu m$ in Fig. 4.9. An SRS Stokes mode corresponding to $\omega_{FIR} \approx 248 \text{ cm}^{-1}$ remains unchanged across the entire temperature tuning range. It is worth noting that the third-order ($g_{st}^{(3)}$) mediated SPS Stokes mode ($> 248 \text{ cm}^{-1}$ shift) is unable to sustain the cavity losses at a certain T_{ov} owing to its low gain. Also, the SPS Stokes shifts tend to reduce at high crystal oven temperatures (T_{ov}) which could be attributed to dominant participation from low energy external lattice vibrations. An expected consequence

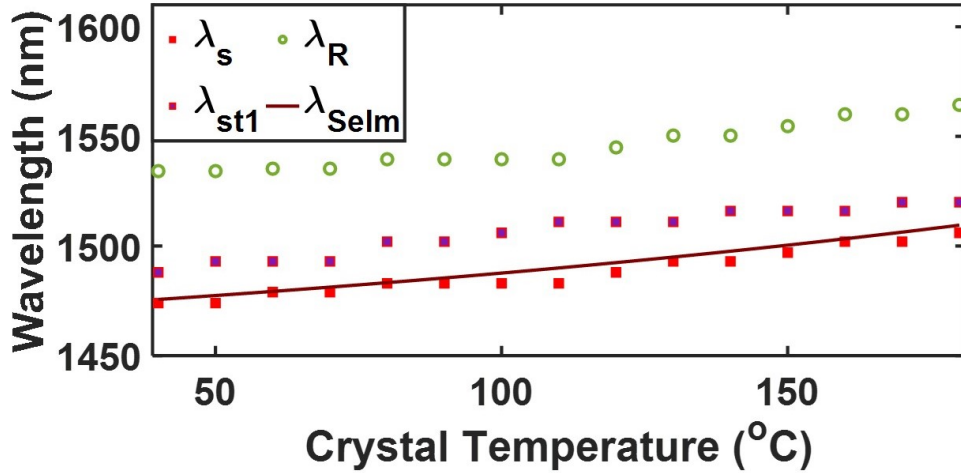


Figure 4.8: Variation in (a) measured SRO signal wavelength (λ_s) (red square dots), (b) measured SPS Stokes wavelength (λ_{st1}) (purple square dots) and (c) expected wavelength corresponding to 248 cm^{-1} SRS mode (λ_R) (green circles) as a function of crystal oven temperature (T_{ov}) for $\Lambda_{QPM} = 29.5 \mu m$. Solid maroon curve represents the expected SRO signal wavelength (λ_{Selm}) variation estimated from the phase-matching for SRO.

of the SPS (or SRS) process could be observed through the distortion in the SRO idler (or signal) spatial beam quality. This is primarily due to generation of SPS (or SRS) Stokes which propagate at a very small angle $\phi \leq 5^\circ$ with respect to SRO signal beam. In order to appreciate this point, we measured the spatial beam quality of the idler beam using a knife-edge based scanning beam profiler (NanoScan, Ophir, USA) in the far-field. A representative measurement at $P_p \approx 24 \text{ W}$ ($\Lambda_{QPM} = 29.5 \mu m$ and $T_{ov} = 100^\circ C$) yielded

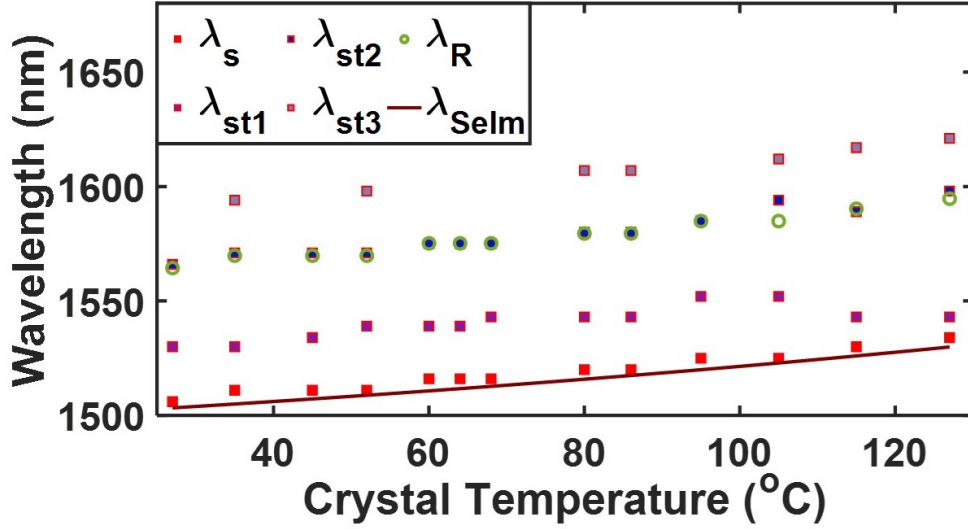


Figure 4.9:]

Variation in (a) measured SRO signal wavelength (λ_s) (red square dots), (b) measured 1st SPS Stokes wavelength (λ_{st1}) (purple square dots), (c) expected SRS wavelength (λ_R) (green circles), (d) measured SRS wavelength (λ_{st2}) (blue dots) and (e) measured 2nd SPS Stokes wavelength (λ_{st3}) (gray square dots) as a function of crystal oven temperature (T_{ov}) for $\Lambda_{QPM} = 30.0 \mu\text{m}$. Solid maroon curve represents the expected SRO signal wavelength variation estimated from the nonlinear phase-matching.

$M_x^2 \leq 1.3$ and $M_y^2 \leq 1.7$ which is significant deviation from that exhibited by the pump beam ($M^2 \leq 1.05$).

4.4 Conclusion

We have demonstrated a SRO using a 80 mm long MgO:PPLN crystal which delivers a maximum idler power of $\approx 2 \text{ W}$. The high intra-cavity SRO signal manifests in SPS and SRS processes which has been observed as Stokes frequencies in the SRO signal spectrum. The Stokes mode corresponding to the SRS exhibits a constant wavelength (or frequency) shift with respect to the SRO signal frequency when the SRO frequency tuning is carried out. On the other hand, the SPS Stokes mode exhibits a non-uniform spectral variation with respect to the SRO signal when the MgO:PPLN crystal temperature is varied. This is analyzed using the TO phonon dispersion properties of MgO:PPLN and the polariton-mediated

phase-matched nonlinear optical interaction. This process allows us efficiently generate coherent continuous-wave FIR (or THz) radiation through utilizing the high intra-cavity signal power in a SRO configuration. Further, through generation of multiple Stokes frequencies, the SRO could deliver optical pulses by adopting suitable phase-locking technique.

This Chapter constitutes the following journal publication:

R. R. Sahoo, M. K. Shukla, and R. Das, “Stimulated polariton scattering in Yb-laser pumped lithium niobate based continuous-wave singly-resonant optical parametric oscillator”, J. Opt. Soc. Am. B 39 (10) 2022.

References

- [1] L. E. Myers and W. R. Bosenberg, "Periodically poled lithium niobate and quasi-phase-matched optical parametric oscillators," *IEEE Journal of Quantum Electronics*, vol. 33, no. 10, pp. 1663–1672, 1997.
- [2] U. Schwarz and M. Maier, "Frequency dependence of phonon-polariton damping in lithium niobate," *Physical Review B*, vol. 53, no. 9, p. 5074, 1996.
- [3] H. Bakker, S. Hunsche, and H. Kurz, "Investigation of anharmonic lattice vibrations with coherent phonon polaritons," *Physical Review B*, vol. 50, no. 2, p. 914, 1994.
- [4] R. L. Byer, J. Young, and R. Feigelson, "Growth of high-quality LiNbO_3 crystals from the congruent melt," *Journal of Applied Physics*, vol. 41, no. 6, pp. 2320–2325, 1970.
- [5] P. Haycock and P. Townsend, "A method of poling LiNbO_3 and LiTaO_3 below T_c ," *Applied physics letters*, vol. 48, no. 11, pp. 698–700, 1986.
- [6] M. Yamada, N. Nada, M. Saitoh, and K. Watanabe, "First-order quasi-phase matched LiNbO_3 waveguide periodically poled by applying an external field for efficient blue second-harmonic generation," *Applied Physics Letters*, vol. 62, no. 5, pp. 435–436, 1993.
- [7] G. D. Miller, *Periodically poled lithium niobate: modeling, fabrication, and nonlinear optical performance*. Stanford university, 1998.
- [8] A. Barker Jr and R. Loudon, "Dielectric properties and optical phonons in LiNbO_3 ," *Physical Review*, vol. 158, no. 2, p. 433, 1967.
- [9] V. Gorelik and P. Sverbil', "Raman scattering by longitudinal and transverse optical

- vibrations in lithium niobate single crystals,” *Inorganic Materials*, vol. 51, no. 11, pp. 1104–1110, 2015.
- [10] N. Sidorov, A. Kruk, A. Yanichev, M. Palatnikov, and B. Mavrin, “Temperature investigations of raman spectra of stoichiometric and congruent lithium niobate crystals,” *Optics and Spectroscopy*, vol. 117, pp. 560–571, 2014.
- [11] Y. N. Polivanov, “Raman scattering of light by polaritons,” *Soviet Physics Uspekhi*, vol. 21, no. 10, p. 805, 1978.
- [12] V. Pasiskevicius, A. Fragemann, F. Laurell, R. Butkus, V. Smilgevicius, and A. Piskarskas, “Enhanced stimulated raman scattering in optical parametric oscillators from periodically poled $ktiopo_4$,” *Applied physics letters*, vol. 82, no. 3, pp. 325–327, 2003.
- [13] N. Bloembergen and Y. Shen, “Coupling between vibrations and light waves in raman laser media,” *Physical Review Letters*, vol. 12, no. 18, p. 504, 1964.
- [14] U. Schwarz and M. Maier, “Damping mechanisms of phonon polaritons, exploited by stimulated raman gain measurements,” *Physical Review B*, vol. 58, no. 2, p. 766, 1998.
- [15] P. Wang, X. Zhang, Z. Cong, Z. Liu, X. Chen, Z. Qin, F. Gao, J. Xu, Z. Wang, and N. Ming, “Modeling of intracavity-pumped q-switched terahertz parametric oscillators based on stimulated polariton scattering,” *Optics Express*, vol. 28, no. 5, pp. 6966–6980, 2020.
- [16] V. Pasiskevicius, C. Canalias, and F. Laurell, “Highly efficient stimulated raman scattering of picosecond pulses in $ktiopo_4$,” *Applied physics letters*, vol. 88, no. 4, p. 041110, 2006.

- [17] A. M. Warriar, R. Li, J. Lin, A. J. Lee, H. M. Pask, and D. J. Spence, “Tunable terahertz generation in the picosecond regime from the stimulated polariton scattering in a $linbo_3$ crystal,” *Optics Letters*, vol. 41, no. 18, pp. 4409–4412, 2016.
- [18] H. Jang, G. Strömquist, V. Pasiskevicius, and C. Canalias, “Control of forward stimulated polariton scattering in periodically-poled ktp crystals,” *Optics Express*, vol. 21, no. 22, pp. 27277–27283, 2013.
- [19] H. Jang, A.-L. Viotti, G. Strömquist, A. Zukauskas, C. Canalias, and V. Pasiskevicius, “Counter-propagating parametric interaction with phonon-polaritons in periodically poled $ktiopo_4$,” *Optics Express*, vol. 25, no. 3, pp. 2677–2686, 2017.
- [20] J. Zang, Z. Cong, X. Chen, X. Zhang, Z. Qin, Z. Liu, J. Lu, D. Wu, Q. Fu, S. Jiang, *et al.*, “Tunable kta stokes laser based on stimulated polariton scattering and its intracavity frequency doubling,” *Optics Express*, vol. 24, no. 7, pp. 7558–7565, 2016.
- [21] J. Kießling, K. Buse, K. L. Vodopyanov, and I. Breunig, “Continuous-wave optical parametric source for terahertz waves tunable from 1 to 4.5 thz frequency,” in *Non-linear Frequency Generation and Conversion: Materials, Devices, and Applications XIII*, vol. 8964, pp. 45–52, SPIE, 2014.
- [22] A. V. Okishev and J. D. Zuegel, “Intracavity-pumped raman laser action in a mid-IR, continuous-wave (cw) MgO: PPLN optical parametric oscillator,” *Optics Express*, vol. 14, no. 25, pp. 12169–12173, 2006.
- [23] J. Kiessling, R. Sowade, I. Breunig, K. Buse, and V. Dierolf, “Cascaded optical parametric oscillations generating tunable terahertz waves in periodically poled lithium niobate crystals,” *Optics Express*, vol. 17, no. 1, pp. 87–91, 2009.

- [24] J. E. Schaar, K. L. Vodopyanov, and M. M. Fejer, "Intracavity terahertz-wave generation in a synchronously pumped optical parametric oscillator using quasi-phase-matched gaas," *Optics letters*, vol. 32, no. 10, pp. 1284–1286, 2007.
- [25] L. Liu, X. Li, T. Liu, X. Xu, and Z. Jiang, "Cascaded continuous-wave singly resonant optical parametric oscillator pumped by a single-frequency fiber laser," *Optics & Laser Technology*, vol. 44, no. 5, pp. 1214–1218, 2012.
- [26] Y.-R. Shen, *Principles of nonlinear optics*. Wiley-Interscience, New York, NY, USA, 1984.
- [27] A. J. Lee and H. M. Pask, "Continuous wave, frequency-tunable terahertz laser radiation generated via stimulated polariton scattering," *Optics letters*, vol. 39, no. 3, pp. 442–445, 2014.
- [28] A. J. Lee and H. M. Pask, "Cascaded stimulated polariton scattering in a $Mg : LiNbO_3$ terahertz laser," *Optics Express*, vol. 23, no. 7, pp. 8687–8698, 2015.
- [29] A. Lee, Y. He, and H. Pask, "Frequency-tunable thz source based on stimulated polariton scattering in $Mg : LiNbO_3$," *IEEE Journal of Quantum Electronics*, vol. 49, no. 3, pp. 357–364, 2013.
- [30] A. M. Warriar, J. Lin, H. M. Pask, A. J. Lee, and D. J. Spence, "Multiwavelength ultrafast $linbo_3$ raman laser," *Optics Express*, vol. 23, no. 20, pp. 25582–25587, 2015.
- [31] D. A. Walsh, P. G. Browne, M. H. Dunn, and C. F. Rae, "Intracavity parametric generation of nanosecond terahertz radiation using quasi-phase-matching," *Optics express*, vol. 18, no. 13, pp. 13951–13963, 2010.
- [32] G. Boyd and D. Kleinman, "Parametric interaction of focused gaussian light beams," *Journal of Applied Physics*, vol. 39, no. 8, pp. 3597–3639, 1968.

-
- [33] R. L. Sutherland, *Handbook of nonlinear optics*. CRC press, 2003.
- [34] I.-H. Bae, H.-S. Moon, S.-K. Kim, S.-N. Park, and D.-H. Lee, “Self-guided operation of singly resonant continuous-wave optical parametric oscillator based on bulk MgO-doped PPLN,” *Applied Physics B*, vol. 106, no. 4, pp. 797–801, 2012.
- [35] M. Vainio, J. Peltola, S. Persijn, F. Harren, and L. Halonen, “Thermal effects in singly resonant continuous-wave optical parametric oscillators,” *Applied Physics B*, vol. 94, no. 3, pp. 411–427, 2009.
- [36] M. K. Shukla, P. S. Maji, and R. Das, “Yb-fiber laser pumped high-power, broadly tunable, single-frequency red source based on a singly resonant optical parametric oscillator,” *Optics Letters*, vol. 41, no. 13, pp. 3033–3036, 2016.
- [37] Y. Repelin, E. Husson, F. Bennani, and C. Proust, “Raman spectroscopy of lithium niobate and lithium tantalate. force field calculations,” *Journal of Physics and Chemistry of Solids*, vol. 60, no. 6, pp. 819–825, 1999.
- [38] S. S. Sussman, *Tunable light scattering from transverse optical modes in lithium niobate*. Stanford University, 1970.
- [39] O. Gayer, Z. Sacks, E. Galun, and A. Arie, “Temperature and wavelength dependent refractive index equations for MgO-doped congruent and stoichiometric $LiNbO_3$,” *Applied Physics B*, vol. 91, no. 2, pp. 343–348, 2008.

Chapter 5

Geometric phase measurement in singly resonant optical parametric pscillator

5.1 Motivation

The geometric phase (γ) of light is an invariant for dynamically evolving photonic system. The geometric phase estimation in condensed-matter systems provides plausible route to understand exotic effects such as quantum Hall effect and transport in topological insulators [1, 2]. The concept of geometric phase is derived from the evolution of states in parameter space (or phase space) [3, 4, 5]. Pancharatnam, in his seminal work, demonstrated that a change in polarization of light is accompanied by accumulation of a geometric phase. This phase has a geometrical interpretation in terms of the trajectory in the polarization space. Through a series of experimental effort, Pancharatnam proposed that, when the polarization returns to its original state, it forms a closed trajectory in the parameter space. The solid angle (Ω) subtended by the closed-trajectory at the origin of the parameter determines the geometric phase (γ). Mathematically, this could be represented as;

$$\gamma = -\frac{1}{2}\Omega \quad (5.1)$$

Sir Michael Berry proposed a similar formalism in a closed quantum mechanical system comprised of *spin-1/2* particles in magnetic field. The eigenstate of the *spin-1/2* particle in a magnetic field, evolves adiabatically and traces a closed trajectory in the parameter space, accumulating a geometric phase of $\gamma = -\frac{1}{2}\Omega$. Therefore, the geometric phase is also termed as Pancharatnam-Berry (PB) phase [4]. The Pancharatnam-Berry phase found

numerous applications such as light guiding and wavefront shaping [6, 7, 8, 9]. Recently, accumulation of geometric phase in a nonlinear optical process has drawn attention and adiabatic frequency conversion processes have been shown to occur in nonlinear optical crystals [10, 11, 12, 13, 14, 15, 16, 17]. It is worthwhile to point that the existence of geometric phase have played a crucial role in the development of nonlinear metasurfaces [18]. By optimally tailoring the geometric phase acquired in a nonlinear optical processes have resulted in the enhancement of efficiency, robustness, tunability and observation of non-reciprocity [19, 20, 21, 22, 23].

5.2 Geometric phase in three wave mixing process

The nonlinear optical frequency conversion processes, under the small pump depletion approximation, could be modeled in such manner that draw close resemblance with the evolution dynamics of a *spin-1/2* system in magnetic field. In order to explicitly show this, we consider interaction between three waves (ω_p , ω_s and ω_i) such that $\omega_p = \omega_s + \omega_i$. Under the slowly varying envelope approximation, we could express the field associated with each wave as,

$$E_n(r, t) = A_n(z)\tilde{E}(x, y)e^{i(k_n z - \omega_n t)} + c.c. \quad (5.2)$$

where $n \equiv p, s, i$, $A_n(z)$ is the slowly varying envelope and k_n is the propagation constant of each wave. By transforming co-ordinates of the amplitude as

$$a_s(z) = \frac{\sqrt{k_s}}{\omega_s A_p} A_s(z) \quad (5.3)$$

and

$$a_i(z) = \frac{\sqrt{k_i}}{\omega_i A_p} A_i(z) \quad (5.4)$$

By considering low pump depletion, the signal to idler conversion could be expressed as,

$$i \frac{d}{dz} a_s^*(z) = \kappa^* e^{i\Delta k z} a_i(z) \quad (5.5)$$

$$i \frac{d}{dz} a_i(z) = -\kappa e^{(-i\Delta kz)} a_s^*(z) \quad (5.6)$$

where the coupling coefficient is,

$$\kappa = \frac{2d_{eff}\omega_s\omega_i}{\sqrt{k_s k_i} c^2} A_p \quad (5.7)$$

with d_{eff} being the effective nonlinear constant and the phase-mismatch is given by

$$\Delta k = k_p - k_s - k_i \quad (5.8)$$

In the three wave mixing process, we consider the mode-coupling between signal state (mode) and the idler state (mode). These two orthogonal states could be assumed to span the Hilbert space. The orthogonality is governed by the virtue of the fact that there is no interference possible between these two modes. The signal and idler states could be represented by a state vector by considering the Manley-Rowe relation as,

$$|\psi\rangle = \frac{[a_s^*, a_i]^T}{\sqrt{|a_s^*|^2 + |a_i|^2}} \quad (5.9)$$

In such a scenario, the dynamical equation of motion 5.5 and 5.6 is;

$$i \frac{d}{dz} |\tilde{\psi}\rangle = \begin{bmatrix} \frac{\Delta k}{2} & \kappa^* \\ -\kappa & -\frac{\Delta k}{2} \end{bmatrix} |\tilde{\psi}\rangle \quad (5.10)$$

In order to write the above equation, we have used the transformation,

$$|\tilde{\psi}\rangle = \frac{[\tilde{a}_s^*, \tilde{a}_i]^T}{\sqrt{|a_s^*|^2 + |a_i|^2}} \quad (5.11)$$

where

$$a_s^* = \sqrt{k_i \omega_s} \tilde{a}_s e^{(i\Delta kz/2)} \quad (5.12)$$

and

$$a_i = \sqrt{k_s \omega_i} \tilde{a}_i e^{(-i\Delta kz/2)} \quad (5.13)$$

It is worth pointing out that the coupling coefficient (κ) takes the off-diagonal positions in the Hamiltonian. When the parameters Δk and κ varies adiabatically in the parameter space, the state vector evolves and in the evolution process, it acquires a geometric phase. The geometric phase originates from the geometry of the trajectory which the state vector takes on the Bloch sphere. In a general case, where the state vector traces a complete rotation, the geometric phase is given by the half of the solid angle subtended by the trajectory at the origin of the Bloch sphere. On the other hand, if the trajectory does not form a closed loop then such a surface area is erected by connecting the terminal points of the trajectory by the shortest geodesic arc. This situation is encountered in the frequency down-conversion case which is represented by a non-Hermitian Hamiltonian (see 5.10). Also, it is worth pointing out that the Hamiltonian represented by 5.10 exhibits \mathcal{PT} -symmetry and hence, exhibits a spectrum of real and imaginary eigenvalues. In order to draw resemblance with spin dynamics, the non-Hermitian operator could be expressed as;

$$i \frac{d}{dz} |\tilde{\psi}\rangle = \begin{bmatrix} \frac{\Delta k}{2} & \kappa^* \\ -\kappa & -\frac{\Delta k}{2} \end{bmatrix} |\tilde{\psi}\rangle = -(\sigma \cdot B) |\tilde{\psi}\rangle \quad (5.14)$$

where $\sigma = (\sigma_x, \sigma_y, \sigma_z)$ are the Pauli spin matrices and are represented as,

$$\sigma_x = \begin{pmatrix} 0 & 1 \\ 1 & 0 \end{pmatrix}, \quad \sigma_y = \begin{pmatrix} 0 & -i \\ i & 0 \end{pmatrix}, \quad \sigma_z = \begin{pmatrix} 1 & 0 \\ 0 & -1 \end{pmatrix} \quad (5.15)$$

In this case, the synthetic magnetic field \vec{B} in the parameter space is given by,

$$\vec{B}(r) = -i * Im(\kappa)\hat{x} + i * Re(\kappa)\hat{y} + \frac{\Delta k}{2}\hat{z} \quad (5.16)$$

This justifies our effort to represent a three-wave mixing process using the Bloch sphere representation. Since, the signal state ($|\omega_s\rangle$) and the idler state ($|\omega_i\rangle$) represent the pseudo-spin (basis) states, the south pole and the north pole are essentially represented by $|\omega_s\rangle$ and $|\omega_i\rangle$. Consequently, the equivalent Stokes parameters could be defined using pseudo-spin states as,

$$S_i = \langle \tilde{\psi} | \sigma_i | \tilde{\psi} \rangle \quad (5.17)$$

which simplifies to,

$$S_1 = \frac{1}{N} (\tilde{a}_s \tilde{a}_i + \tilde{a}_s^* \tilde{a}_i^*) \quad (5.18)$$

$$S_2 = \frac{1}{N} (\tilde{a}_s^* \tilde{a}_i^* - \tilde{a}_s \tilde{a}_i) \quad (5.19)$$

$$S_3 = \frac{1}{N} (|\tilde{a}_i|^2 - |\tilde{a}_s|^2) \quad (5.20)$$

Here, N is given by,

$$N = |a_s^*|^2 + |a_i|^2 \quad (5.21)$$

The Stokes vector, also known as the state-vector \vec{S} describes the evolution of the signal and idler beams (states) along the propagation direction. The z -component of the state vector *i.e.* (S_3) provides the information regarding frequency conversion efficiency. The south pole $\vec{S} = (0, 0, -1)$ corresponds to zero conversion (all power in signal state) whereas the north pole $\vec{S} = (0, 0, 1)$ represents the 100% conversion efficiency (all power in idler state). The equations 5.18, 5.19 and 5.20 also satisfy the relation,

$$S_1^2 + S_2^2 + S_3^2 = 1 \quad (5.22)$$

which makes the radius of the Bloch sphere to be unity. The conservation law expressed in (5.22) signify the conservation of total energy in the frequency conversion process. In an singly-resonant optical parametric oscillator (SRO), the experimental configuration constraints $\Delta k = 0$ *i.e.* the nonlinear interaction is always phase-matched. However, a change in pump power leads to substantial changes in the coupling constant κ that would result in acquiring of geometric phase by a signal and the idler beam. For sake of completeness, the evolution of states in this could be simplified and expressed as

$$\frac{\partial \vec{S}}{\partial z} = \vec{B} \times \vec{S} \quad (5.23)$$

which is a equivalent Bloch for nonlinear optical frequency conversion. Equation (5.23) essentially makes the point that the state vector (\vec{S}) precesses the synthetic magnetic field (\vec{B}).

5.3 Experimental set-up

In order to experimentally observe the manifestations, we have designed a MgO-doped PPLN based SRO which is pumped by a single-frequency fiber laser. In the experiment, we have carried out measurement on phase change in the undepleted pump beam when the SRO operates above the threshold. This measurement is realized through interfering the undepleted pump beam with the reference arm pump beam in Mach-Zehnder setting. The experimental configuration exhibits a close resemblance with the SRO configuration

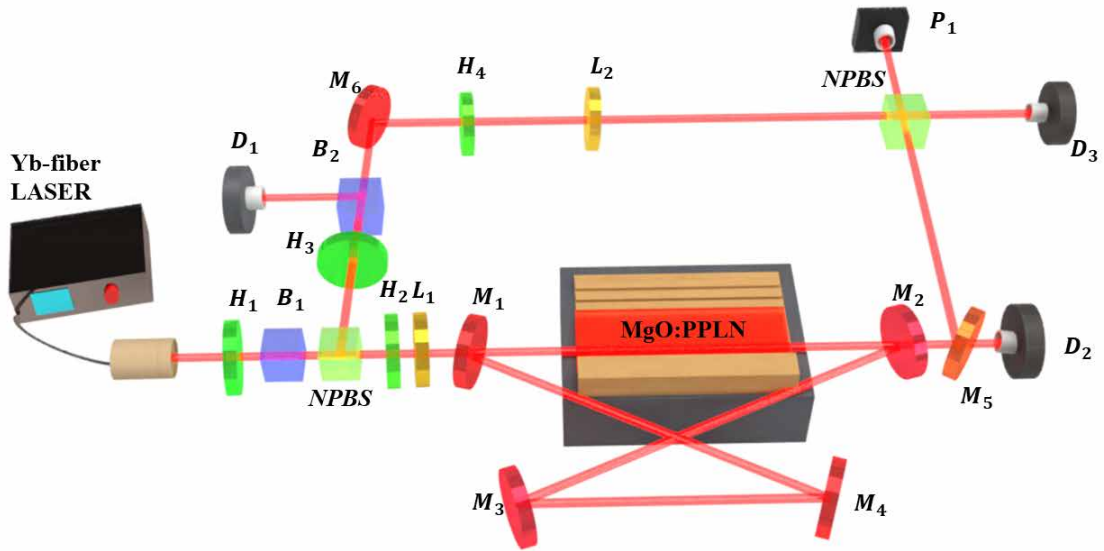


Figure 5.1: A schematic of the experimental set-up for the SRO; $H_{1,2,3,4}$: Half-wave plate, $B_{1,2}$: Polarizing beam-splitter, NPBS: Non-polarizing beam-splitter, $l_{1,2}$: Convex lens, $M_{1,2}$: Plano-concave mirrors, $M_{3,4}$: Plane mirrors, OV: Temperature controlled oven housing the nonlinear crystal $MgO : PPLN$, M_5 : Dichroic Mirror, $D_{1,2,3}$: Thermal detectors, P_1 : CCD camera.

which is explained in chapters 3 and 4. The schematic for the experimental set-up is shown in figure 5.1 which comprises a fiber laser pump delivering ≈ 40 W of linearly-polarized, single-frequency output at 1064 nm wavelength and $M^2 \leq 1.1$. A half wave plate (HWP) H_1 , in conjunction with a polarizing beam splitter (PBS) B_1 is used for controlling the in-

cident pump power (P_p). The forward propagating pump power is divided into two arms using a 50:50 non-polarizing beam splitter (NPBS). This splitting is used for the construction of the *Mach-Zehnder* interferometer (reference arm) where the SRO is positioned in one arm of the interferometer. A second HWP H_2 is used to obtain a suitable pump polarisation for carrying out phase-matching in MgO:PPLN crystal. A convex lens L_1 ($f=100$ mm) is employed for obtaining a beam-waist of $w_{0p} \approx 90 \mu\text{m}$ at the center of MgO:PPLN crystal which results in a Boyd-Kleinman (BK) focusing parameter of $\xi \approx 0.64$ [24]. This is essentially done to achieve a moderate to low frequency conversion efficiency [24]. The SRO is comprised of a four-mirror ring-cavity with two curved mirrors having radius of curvature (ROC=-200 mm) and two plane mirrors. The cavity design ensures a cavity length of ≈ 100 cm. The cavity mirrors are highly reflecting ($R \geq 99\%$) in the 1350-1650 nm wavelength range and highly transmitting ($T \geq 85\%$) for the pump (1064 nm) as well as idler (2500-4500 nm) wavelength range. The SRO nonlinear crystal is an 80 mm long and 1 mm thick multi-grating MgO:PPLN crystal with grating periods varying from $\Lambda = 27.5 \mu\text{m}$ to $\Lambda = 30 \mu\text{m}$ so as to facilitate *type-0* phase-matching. The entry as well as exit surface of MgO:PPLN crystal is anti-reflection (AR) coated for pump, signal and idler wavelengths. The crystal is housed in an oven whose temperature (T_{ov}) could be varied from room temperature to 200°C . In the other arm of *Mach-Zehnder* interferometer, a combination of HWP and PBS is employed for variably attenuating the beam and subsequently, it helps in achieving in equal pump power in both the interferometer arms. A HWP H_4 and convex lens L_2 is used to match the pump polarization and the pump beam diameter respectively with the residual pump in the other arm of the interferometer. The reference pump beam and the undepleted pump beam from the SRO, are allowed to interfere in the NPBS. The detector D_3 measures the power of the central lobe of interference pattern and CCD camera P_1 records the interference pattern.

5.4 Result and Discussion

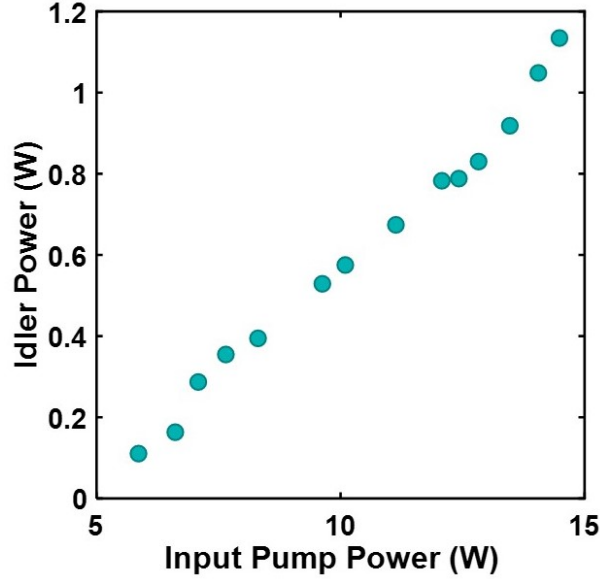


Figure 5.2: Variation of idler power as a function of pump power at crystal temperature $T = 100^\circ\text{C}$ and $w_0 \approx 90\mu\text{m}$

The SRO threshold pump power (P_{Th}) was measured to be $\approx 5\text{ W}$ at crystal oven temperature of $T_{ov} 100^\circ\text{C}$ and MgO:PPLN crystal grating of $\Lambda = 30\mu\text{m}$. When a temperature tuning is carried out, the SRO could exhibit wavelength tunability from $1509 - 1550\text{ nm}$ in signal band and from $3394 - 3609\text{ nm}$ in idler band as per the Sellmeier's relation for MgO-doped LiNbO_3 . This has been verified by measuring the wavelength at 60°C , 100°C , 140°C and 180°C which exhibits good agreement with the wavelengths predicted using the Sellmeier's relation. The variation in idler power as a function of pump power is shown in Fig. 5.2 where we could observe that the maximum idler power obtained from the SRO is $\approx 1.16\text{ W}$ at $T_{ov} = 100^\circ\text{C}$ when $P_p \approx 14\text{ W}$. This essentially means that the maximum conversion efficiency is $\approx 8\%$ which could be categorized as a low-to-moderate efficient configuration. Therefore, under the weak pump depletion approximation, the dynamical evolution of the signal and idler states could be understood from the Hamiltonian in Eq.

5.14. The evolution of state vector (\vec{S}) in the parameter space results in accumulation of geometric phase which could experimentally measured using a Mach-Zehnder interferometer shown in Fig. 5.1. In order to appreciate the phase measurement, we note that the interference of beams coming from two arms of the interferometer, with powers P_1 and P_2 with a phase difference of θ , results in a power distribution on the detector plane which could be expressed as [25, 13],

$$P = P_1 + P_2 + 2P_1P_2\cos\theta \quad (5.24)$$

In the SRO experiment, we have measured the intensity at both NBPS terminals (faces). When the pump power (P_p) increases, it is apparent that the coupling coefficient (κ) increases which could manifest through a geometric phase accumulated by the signal or idler beam (assuming $\Delta k = 0$). This is apparent from the Hamiltonian (Eq. 5.14) which depicts a different state vector (\vec{S}) trajectory on the Bloch sphere. Consequently, the acquired geometric phase (by signal or the idler) would be different at different pump power (P_p). It is also interesting to note that the frequency conversion in an SRO is constrained by the requirement $\theta_p = \theta_s + \theta_i - \frac{\pi}{2}$ where θ_p , θ_s and θ_i is the total phase acquired by the pump, signal and idler respectively [26]. The total phase has a dynamic (ϕ_D) as well as geometric (γ) component. This implies that a change in θ_s or θ_i (by virtue of change in ϕ_D and/or γ) would essentially lead to a change in θ_p . Since, the dynamic phase change for signal and idler is given by κL (when $\Delta k = 0$), the geometric phase acquired by the signal and idler beam would modify the pump phase (θ_p) through the relation $\theta_p = 2\kappa L + 2\gamma - \frac{\pi}{2}$. Since κ as well as γ is function of pump power, θ_p changes as we change the pump power (P_p). Therefore, the measurement of the change in the intensity of central lobe of the interference pattern would essentially yield the total phase change as per Eq. (5.24). Here, we assume $P_1 \approx P_2$ and the geometric phase could be ascertained through the measured θ_p assuming a suitable value of θ_p at the threshold pump power ($P_{p(th)}$). The recorded variation of inten-

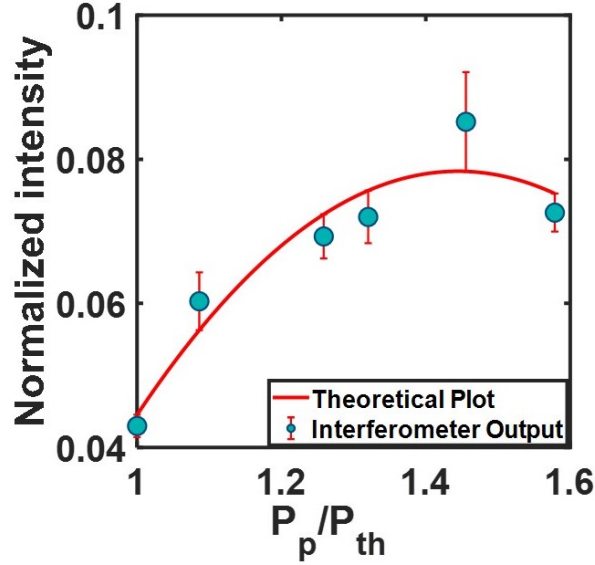


Figure 5.3: Variation of intensity at the center of the fringe pattern with P_p/P_{th} at crystal temperature $T = 100^\circ C$ and $w_0 \approx 90\mu m$

sity at the center ($\vec{r} = 0$) of the fringe pattern is shown in Fig. 5.3. The measured variation in the intensity is represented by the green dots and a solid red curve represents a $\sin^2\theta_p$ variation which indicates that θ_p is a function of pump power (or the coupling coefficient κ). In order to obtain γ , the quantity $\kappa L - \frac{\pi}{2}$ needs to be subtracted from θ_p .

5.5 Conclusion

We have demonstrated a SRO using a 80 mm long MgO:PPLN crystal which delivers a maximum idler power of $\approx 1.2 W$. A brief analytical formulation is presented to draw an equivalence between a *spin-1/2* system and $\chi^{(2)}$ -mediated nonlinear frequency conversion. We define a state vector (\vec{S}) comprising complex mode-field amplitudes of signal and idler beams and derive an expression for synthetic magnetic field (\vec{B}). The precession of state vector about the synthetic magnetic field results in accumulation of a geometric phase which could be measured experimentally using *Mach-Zehnder* interferometer.

References

- [1] F. D. M. Haldane, “Model for a quantum hall effect without landau levels: Condensed-matter realization of the” parity anomaly”,” *Physical review letters*, vol. 61, no. 18, p. 2015, 1988.
- [2] B. A. Bernevig, “Topological insulators and topological superconductors,” in *Topological Insulators and Topological Superconductors*, Princeton university press, 2013.
- [3] D. J. Griffiths and D. F. Schroeter, *Introduction to quantum mechanics*. Cambridge university press, 2018.
- [4] M. V. Berry, “The adiabatic phase and pancharatnam’s phase for polarized light,” *Journal of Modern Optics*, vol. 34, no. 11, pp. 1401–1407, 1987.
- [5] S. Pancharatnam, “Generalized theory of interference and its applications,” *Proceedings of the Indian Academy of Sciences-Section A*, vol. 44, no. 6, pp. 398–417, 1956.
- [6] S. Slussarenko, A. Alberucci, C. P. Jisha, B. Piccirillo, E. Santamato, G. Assanto, and L. Marrucci, “Guiding light via geometric phases,” *Nature Photonics*, vol. 10, no. 9, pp. 571–575, 2016.
- [7] Z. Bomzon, V. Kleiner, and E. Hasman, “Pancharatnam–berry phase in space-variant polarization-state manipulations with subwavelength gratings,” *Optics letters*, vol. 26, no. 18, pp. 1424–1426, 2001.
- [8] L. Marrucci, C. Manzo, and D. Paparo, “Pancharatnam-berry phase optical elements for wave front shaping in the visible domain: Switchable helical mode generation,” *Applied Physics Letters*, vol. 88, no. 22, p. 221102, 2006.

-
- [9] M. Khorasaninejad, W. T. Chen, R. C. Devlin, J. Oh, A. Y. Zhu, and F. Capasso, “Metalenses at visible wavelengths: Diffraction-limited focusing and subwavelength resolution imaging,” *Science*, vol. 352, no. 6290, pp. 1190–1194, 2016.
- [10] H. Suchowski, G. Porat, and A. Arie, “Adiabatic processes in frequency conversion,” *Laser & Photonics Reviews*, vol. 8, no. 3, pp. 333–367, 2014.
- [11] A. Karnieli, Y. Li, and A. Arie, “The geometric phase in nonlinear frequency conversion,” *Frontiers of Physics*, vol. 17, no. 1, p. 12301, 2022.
- [12] Y. Li, O. Yesharim, I. Hurvitz, A. Karnieli, S. Fu, G. Porat, and A. Arie, “Adiabatic geometric phase in fully nonlinear three-wave mixing,” *Physical Review A*, vol. 101, no. 3, p. 033807, 2020.
- [13] A. Karnieli and A. Arie, “Fully controllable adiabatic geometric phase in nonlinear optics,” *Optics Express*, vol. 26, no. 4, pp. 4920–4932, 2018.
- [14] A. Karnieli, S. Trajtenberg-Mills, G. Di Domenico, and A. Arie, “Experimental observation of the geometric phase in nonlinear frequency conversion,” *Optica*, vol. 6, no. 11, pp. 1401–1405, 2019.
- [15] A. Karnieli, S. Trajtenberg-Mills, G. Di Domenico, and A. Arie, “Observation of the nonreciprocal adiabatic geometric phase in nonlinear optics,” in *CLEO: Applications and Technology*, pp. JM3B–6, Optica Publishing Group, 2019.
- [16] A. Karnieli and A. Arie, “Nonlinear beam shaping via the geometric phase in sum frequency generation,” in *Advanced Solid State Lasers*, pp. ATu2A–24, Optica Publishing Group, 2018.
- [17] H. Suchowski, D. Oron, A. Arie, and Y. Silberberg, “Geometrical representation of

- sum frequency generation and adiabatic frequency conversion,” *Physical Review A*, vol. 78, no. 6, p. 063821, 2008.
- [18] G. Li, S. Zhang, and T. Zentgraf, “Nonlinear photonic metasurfaces,” *Nature Reviews Materials*, vol. 2, no. 5, pp. 1–14, 2017.
- [19] N. Westerberg, C. Maitland, D. Faccio, K. Wilson, P. Öhberg, and E. M. Wright, “Synthetic magnetism for photon fluids,” *Physical Review A*, vol. 94, no. 2, p. 023805, 2016.
- [20] P. Margules, J. Moses, H. Suchowski, and G. Porat, “Ultrafast adiabatic frequency conversion,” *Journal of Physics: Photonics*, vol. 3, no. 2, p. 022011, 2021.
- [21] H. Suchowski, B. Bruner, A. Ganany-Padowicz, I. Juwiler, A. Arie, and Y. Silberberg, “Adiabatic frequency conversion of ultrafast pulses,” *Applied Physics B*, vol. 105, pp. 697–702, 2011.
- [22] J. Moses, H. Suchowski, and F. X. Kärtner, “Fully efficient adiabatic frequency conversion of broadband titanium sapphire oscillator pulses,” *Optics letters*, vol. 37, no. 9, pp. 1589–1591, 2012.
- [23] G. Porat and A. Arie, “Efficient, broadband, and robust frequency conversion by fully nonlinear adiabatic three-wave mixing,” *JOSA B*, vol. 30, no. 5, pp. 1342–1351, 2013.
- [24] G. Boyd and D. Kleinman, “Parametric interaction of focused gaussian light beams,” *Journal of Applied Physics*, vol. 39, no. 8, pp. 3597–3639, 1968.
- [25] J. J. Sakurai and E. D. Commins, “Modern quantum mechanics, revised edition,” 1995.
- [26] M. Ebrahim-Zadeh, “Continuous-wave optical parametric oscillators,” *Handbook of Optics*, vol. 4, pp. 1–33, 2010.

Future Scope

In chapter three, we observed the generation of the thermal gradient in the MgO : cP P LT Crystal accomplishing variation in Δk along the crystal length. Thermal gradient along the crystal length could be managed with the help of external parameters such as crystal oven temperature, beam waist at the crystal centre. This could pave a way to achieve tunable ultrashort pulse frequency in long-length crystals.

In chapter four, we observed a spectral variation of Stokes mode with respect to the SRO signal when the MgO : PPLN crystal temperature is varied. The tunability of the signal wavelength could further be enhanced by changing the grating period of the crystal hence a wide tunable Stokes mode could obtain. The observation of SPS process in the SRO could facilitate the efficient generation of THz radiation. In addition the variation of Stokes mode will lead to a tunable THz source, hence silicon prisms can be employed to facilitate the outcoupling of THz radiation.

In chapter five, we have discussed an analytical framework to draw an equivalence between the TWM process in SRO with a spin-1/2 system in a magnetic field, by defining an equivalent magnetic field. We have observed a variation in the phase acquired by the pump intensity with the increase in input power, during the TWM process. From this observation, we are planning to calculate the geometric phase acquired by the signal/idler state through the TWM process. The incorporation of the nonlinear geometric phase could open up new avenue in the direction of shaping and manipulating down-converted signal and idler states.